Wallace Torres de Figueiredo

Elucidation of catalytic events at atomic level in Cu_xNi_{1-x}/CeO_2 ($0<x<1$) nanoparticles applied to the reverse water-gas shift (RWGS) reaction

UFRGS
UNIVERSIDADE FEDERAL
DO RIO GRANDE DO SUL

Porto Alegre, RS - Brazil
July, 2017

Wallace Torres de Figueiredo

Elucidação de eventos catalíticos a nível atômico em nanopartículas de Cu_xNi_{1-x}/CeO_2 ($0<x<1$) aplicadas à reação inversa de deslocamento gás-água (RWGS)

Dissertação realizada sob a orientação do Prof. Dr. Fabiano Bernardi e apresentada ao Instituto de Física da Universidade Federal do Rio Grande do Sul, em preenchimento parcial dos requisitos para a obtenção do título de Mestre em Física.

Universidade Federal do Rio Grande do Sul

Instituto de Física

Programa de Pós-Graduação

Orientador: Prof. Dr. Fabiano Bernardi

Porto Alegre, RS - Brasil
Julho, 2017

ACKNLOWLEDGMENT

I would first like to thank Prof. Fabiano Bernardi by its guidance, advisement, patience and friendship. The door to Prof. Bernardi was always open whenever I ran into a trouble spot or had a question about my research. He consistently steered me into the right path, whenever he thought I needed it.

I would like to thank Prof. Dr. Jairton Dupont, from Laboratory of Molecular Catalysis (IQ-UFRGS), by providing the samples used in this work.

I would also like to thank Drs. Virginia Pérez-Dieste and Carlos Escudero from CIRCE beamline, at ALBA - Spain, by the assistence during the NAP-XPS measurements and for valuable discussions towards the understanding of results analysis.

I must thank to ALBA, CMM, LNLS and LNNano for giving me access to state-of-the-art equipment and laboratories that ensured the quality of the measures presented in this work.

Specially, I would like to thank my mother for providing me with all the support that I needed throughout my years of study, even when far from home. Likewise, thanks my friends Fabiola, Willian, Alisson and Catiane for treating me like family and for all the fun we have had in the last two years.

My thanks and appreciation also go to my colleagues who have ennobled my knowledge through enriching discussions, and for all those people who has made my stay away from home more happier and enjoyable.

“[Quantum mechanics] describes nature as absurd from the point of view of common sense. And yet it fully agrees with experiment. So I hope you can accept nature as She is - absurd.” — Richard P. Feynman

ABSTRACT

The CO_2 molecule is the main responsible for the negative consequences of the greenhouse effect. The increasing numbers associated to the amount of CO_2 emission in the atmosphere have attracted the attention of scientists aiming the discovery of new catalysts to CO_2 dissociation reactions. At the same time, several atomic events may influence the catalytic properties of such systems, like the Strong Metal-Support Interaction (SMSI) effect and atomic rearrangement when the bimetallic nanoparticles (NPs) are exposed to a gaseous atmosphere.

This work presents the results of a study about the behavior of $Cu_xNi_{1\text{-}x}/CeO_2$ ($0<x<1$) NPs during the H_2 reduction treatment (step used in the activation of the catalysts) followed by the reverse water-gas shift (RWGS) reaction. The samples were initially characterized in terms of their compositions, chemical components, atomic arrangement and sizes, using the Energy Dispersive X-ray Spectroscopy (EDS), X-Ray Photoelectron Spectroscopy (XPS) and Transmission Electron Microscopy (TEM) techniques. Afterwards, these samples were heated to 500 °C in a H_2 atmosphere. At 500 °C the samples were exposed to H_2 and H_2+CO_2 atmospheres. During all these treatments, the samples were characterized *in situ* by Near Ambient Pressure XPS (NAP-XPS) with incident photon energies of 1250 eV and 2000 eV, X-ray Absorption Spectroscopy (XAS) and time-resolved XAS techniques in transmission mode at the Cu K (8979 eV), Ni K (8333 eV) and Ce L_3 (5723 eV) edges.

The *in situ* measurements performed showed a copper (nickel) migration to the nanoparticles surface during H_2 (H_2+CO_2) gaseous treatment. Moreover, the Cu surface atomic population is dependent on the Cu amount used in the synthesis process. The higher concentration of Cu during the synthesis implies in a smaller Cu surface atomic population during H_2 reduction and RWGS reaction. The occurrence of the geometrical factor of the SMSI effect, characterized by a cerium oxide capping layer surrounding the nanoparticles during reduction treatment, was observed for some of the NPs, revealing the existence of a threshold in the Cu concentration to occur the SMSI effect. Only nanoparticles with high amounts of Cu present the SMSI effect during the H_2 reduction treatment. The surface of the nanoparticles presenting the SMSI effect is recovered to the initial state (free of the capping layer) after inserting the CO_2 atmosphere. Moreover, the nature of the SMSI effect was elucidated for the first time: the capping layer interacts with the Cu and Ni atoms *via* $Ce3d^{10}O2p^6Ce4f^0$ and $Ce3d^{10}O2p^6Ce4f^1$ initial states, depending on the case studied. As a consequence of the SMSI effect, the Cu atoms of the nanoparticles reduce earlier (lower temperature) than similar nanoparticles that do not present the SMSI effect.

The reactivity results towards the CO formation in the RWGS reaction, associated to the catalytic events at atomic level observed (SMSI effect, surface atomic population, change on the oxidation state of the catalysts) led to the design of an optimized catalyst applied to this reaction. The capping layer of the SMSI effect has a negative influence on the reactivity results. The migration of Ni atoms to the surface led to a decrease of the catalyst reactivity in the RWGS reaction. Based on these results, it is proposed a synthesis of nanoparticles with a high amount of Ni in order to avoid the SMSI effect and to allow a high Cu surface atomic population during the RWGS reaction, both playing a key role in the reactivity results towards the RWGS reaction.

RESUMO

A molécula de CO_2 é a principal responsável pelas consequências negativas do efeito estufa. Os números cada vez maiores associados à emissão de CO_2 na atmosfera têm atraído a atenção de cientistas na busca de novos catalisadores para reações de dissociação de CO_2. Simultaneamente, vários eventos atômicos podem influenciar as propriedades catalíticas de tal sistema, como o efeito de forte interação metal-suporte (SMSI - *Strong Metal-Support Interaction*) e o rearranjo atômico nas nanopartículas bimetálicas expostas a atmosferas gasosas.

Este trabalho apresenta os resultados de um estudo sobre o comportamento de nanopartículas (NPs) de Cu_xNi_{1-x}/CeO_2 ($0<x<1$) durante o tratamento de redução em H_2 (etapa usada na ativação de catalisadores) seguido da reação inversa de deslocamento gás-água (RWGS - *Reverse Water-Gas Shift*). As amostras foram inicialmente caracterizadas em termos de suas composições, componentes químicas, arranjo atômico e tamanhos usando as técnicas de espectroscopia de raios X por dispersão em energia (EDS - *Energy Dispersive X-ray Spectroscopy*), espectroscopia de fotoelétrons excitados por raios X (XPS - *X-ray Photoelectron Spectroscopy*) e microscopia eletrônica de transmissão (TEM - *Transmission Electron Microscopy*). Após, as amostras foram aquecidas até 500 °C em uma atmosfera de H_2. Em 500 °C as amostras foram expostas às atmosferas de H_2 e H_2+CO_2. Durante todos esses tratamentos, as amostras foram caracterizadas *in situ* pelas técnicas de XPS em pressões próximas à ambiente (NAP-XPS - *Near Ambient Pressure X-ray Photoelectron Spectroscopy*) com energias de fótons incidentes de 1250 eV e 2000 eV, espectroscopia de absorção de raios X (XAS - *X-ray Absorption Spectroscopy*) e XAS resolvido no tempo medido no modo transmissão nas bordas K do Cu (8979 eV), K do Ni (8333 eV) e L_3 do Ce (5723 eV).

As medidas *in situ* realizadas mostraram uma migração de átomos de Cu (Ni) para a superfície das nanopartículas durante o tratamento em atmosfera de H_2 (H_2+CO_2). Além disso, a população atômica de Cu na superfície é dependente da quantidade de Cu usada no processo de síntese. Uma maior concentração de Cu durante a síntese implica em uma menor população de Cu na superfície durante as reações de redução em H_2 e de RWGS. A ocorrência do fator geométrico do efeito SMSI, caracterizado por uma camada de óxido de cério em torno das nanopartículas durante o tratamento de redução, foi observado para algumas nanopartículas, revelando a existência de um limite na concentração de Cu para a ocorrência do efeito. Somente as nanopartículas com grande quantidade de Cu apresentaram o efeito SMSI durante o tratamento de redução em H_2. A superfície das nanopartículas apresentando o efeito SMSI retorna ao estado inicial (sem a camada de óxido de cério) após a inserção da

atmosfera de CO_2. Além disso, a natureza do efeito SMSI foi elucidada pela primeira vez: a camada de óxido de cério interage com os átomos de Cu e Ni através dos estados iniciais $Ce3d^{10}O2p^{6}Ce4f^{0}$ e $Ce3d^{10}O2p^{6}Ce4f^{1}$, dependendo do caso estudado. Como consequência do efeito SMSI, os átomos de Cu das nanopartículas reduzem antes (temperaturas mais baixas) do que nanopartículas semelhantes que não apresentam o efeito SMSI.

Os resultados de reatividade para a formação de CO através da reação RWGS, associados aos eventos catalíticos a nível atômico observados (efeito SMSI, população atômica de superfície, mudança no estado de oxidação dos catalisadores) levaram à projeção de um catalisador otimizado aplicado à reação RWGS. A camada de óxido de cério do efeito SMSI tem consequência negativa nos resultados de reatividade. A migração de átomos de Ni para a superfície levou a uma diminuição da reatividade catalítica na reação RWGS. Baseado nesses resultados, é proposta a síntese de nanopartículas com uma grande quantidade de Ni visando evitar a ocorrência do efeito SMSI e permitir uma grande população atômica de Cu na superfície durante a reação RWGS, ambos desempenhando um papel fundamental nos resultados de reatividade para a reação RWGS.

CONTENTS

LIST OF ABBREVIATIONS AND ACRONYMS

a.u.	Arbitrary Units
AC	Analysis Chamber
CAE	Constant Analyzer Energy
CCD	Charge-Coupled Device
CCU	Carbon Capture and Utilization
CFCs	Chlorofluorocarbons
CMM	Centro de Microscopia e Microanálise
CNPEM	Centro Nacional de Pesquisa em Energia e Materiais
CRR	Constant Retard Ratio
DRIFTS	Diffuse Reflectance Infrared Fourier Transform Spectroscopy
DXAS	Dispersive X-ray Absorption Spectroscopy
EDS	Energy Dispersive X-ray Spectroscopy
ESM	Earth System Model
EXAFS	Extended X-ray Absorption Fine Structure
FOLU	Forestry and Other Land Uses
FT	Fourier Transform
FWHM	Full Width at Half Maximum
GHG	Greenhouse gases
HRTEM	High-Resolution Transmission Electron Microscopy
HSA	Hemispherical Sector Analyzer
LAMOCA	Laboratory of Molecular Catalysis
LCA	Linear Combination Analysis

LEIS	Low-Energy Ion Scattering
LNLS	Laboratório Nacional de Luz Síncrotron
LS	Long Scan
LWR	Longwave radiation
MS	Mass Spectrometer
NAP-XPS	Near Ambient Pressure X-ray Photoelectron Spectroscopy
NPs	Nanoparticles
PCA	Principal Component Analysis
RWGS	Reverse Water-Gas Shift
SMSI	Strong Metal-Support Interaction
SWR	Shortwave radiation
TEM	Transmission Electron Microscopy
WGS	Water-Gas Shift
XAS	X-ray Absorption Spectroscopy
XANES	X-ray Absorption Near Edge Structure
XPS	X-ray Photoelectron Spectroscopy

LIST OF SYMBOLS

Å	Angstrom
$\hat{A}$	Vector potential operator
A_s	Scattering amplitude
α	Angle between the electron's polarization vector and detection direction
β	Angular asymmetry factor
c	Light speed
$\chi(k)$	EXAFS oscillations
χ^2	*Chi* squared factor, indicating the quality of a XPS fit
D	Particles mean diameter
$D(T)$	Detector efficiency for electrons of kinetic energy T
ΔH_{298K}	Enthalpy of formation at the temperature 298 K
e	Electron charge
E	Energy
E_b	Binding energy
$\hat{\epsilon}$	Polarization vector
ϕ	Quantum state
G	Green's function
Γ	Electron lifetime
$\hat{H}$	Hamiltonian operator
$h\nu$	Photon energy
I	Intensity
$Im(f)$	Imaginary part of the f function
j	Total angular momentum number

J	Photon flux
k	Wave number
l	Orbital angular momentum number
λ_{IMFP}	Inelastic mean free path
m_e	Electron mass
M_{ij}	ij-th element of the M matrix
μ	Absorption coefficient
N_e	Number of electrons
N_s	Number of scattering atoms
$\hat{p}$	Momentum operator
R_{as}	Absorber-scatterer distance
$\mathcal{R}$	R-factor, indicating the quality of a XAS fit
$\rho(z)$	Atomic concentration at the z depth
s	Spin angular momentum number
S_0^2	Amplitude correction factor
σ_{nl}	Photoionization cross section of a electron from the atomic level defined by the n and l quantum numbers
σ_{as}^2	Debye-Waller factor
$\Sigma(E)$	Energy dependent operator
T	Kinetic energy
τ	Complete scattering operator
Θ	Angular direction
ϕ_{spec}	Spectrometer work function
ϕ_{samp}	Sample work function
ϕ_{as}	Phase-shift caused by scattering processes
V	Electrostatic potential

1 INTRODUCTION

Catalysts are chemical compounds capable to conduct and accelerate thermodynamic viable reactions. The application of heterogeneous catalysts, which exist in a distinct phase from the reacting medium, to industrial processes were specially important to the evolution of the modern industrial society. For example, by 1962, about 20% of the manufactured products in the United States of America had already being produced using heterogeneous catalysts. Ever since the chemical industry have been using catalysts in almost every process involved in the ammonia manufacture, methanol synthesis, and crude oil refinement.

The governments and the scientific community are paying attention to the society future on Earth thanks to the evidences of anthropogenic-induced global warming occurring due to the magnification of the greenhouse effect. Recent measurements relates these evidences to the increasing CO_2 emission rate, indicating that the unprecedented carbon dioxide atmospheric concentration is the primary responsible to the warming effect. In response to this problem, a new industrial niche has emerged intending to design mechanisms to recycle this discarded material.

Pursuing the development of an industrial reasonable process to reduce the CO_2 emissions into the atmosphere, the Reverse Water-Gas Shift (RWGS) reaction has been broadly studied and currently considered one of the best alternative technologies to dissociate the carbon dioxide molecules. CO, the main product of the CO_2 dissociation reaction *via* RWGS, is a very flexible chemical intermediate used in many industrial processes, such as hydrocarbons production.

Studies involving copper-based catalysts supported over several oxides such as ZnO, ZnO/Al_2O_3, Al_2O_3, SiO_2, ZrO_2, and CeO_2, demonstrated its prominent efficiency and high activity towards CO_2 dissociation *via* RWGS reaction. Apart from noble metals catalysts (Pt, Pd, Au), nickel-based catalysts are the second most promising catalyst (copper is the first) being able to perform the RWGS reaction at temperatures as low as 150 °C [1]. Supported over cerium and zirconium oxides, nickel catalysts proved to have high selectivity favouring the formation of CO and presenting high CO_2-CO conversion ratios.

Intending to combine the activity and selectivity properties in one single system, Cu-Ni nanoparticles (NPs) supported on ceria were synthesized with different Cu and Ni concentrations. The utilization of ceria as the support is due to its unique properties such as lattice oxygen ion mobility, readily switching between Ce(III) and Ce(IV) states.

The main goal of this work is to examine the RWGS reaction, investigating the kinetic processes and atomic phenomena presented by the Cu-Ni/CeO_2 catalysts. In order to achieve this goal, the electronic and structural properties of the synthesized systems were probed using the X-ray Photoelectron Spectroscopy (XPS), Energy Dispersive X-ray Spectroscopy (EDS) and Transmission Electron Microscopy (TEM) techniques. Concerning the investigations of the reactivity towards the RWGS, CO_2 dissociation into carbon monoxide and water was probed *via* Mass Spectrometry, while the catalysts surface and bulk properties were investigated using synchrotron radiation-based techniques. The *in situ* techniques used in this work were the Near-Ambient Pressure X-ray Photoelectron Spectroscopy (NAP-XPS), X-ray Absorption Spectroscopy (XAS) and time-resolved XAS.

The second chapter of this thesis is dedicated to cover the motivation phenomena that led to this work, where the scientific impulse joins the industrial economic interest on catalysis research. Preceding studies related to relevant atomic phenomena, established models and probed properties are also presented. Third chapter contemplates the physical principles and processes regarding the analysis techniques used to characterize and to explore the catalyst systems. At the fourth chapter, all the measurements before and during the RWGS reaction and the corresponding discussion of results is presented. The fifth chapter shows the conclusions of the work, describing the complete atomic phenomena concerning the kinetics of the RWGS reaction.

2 THE CONTEMPORANEOUS GLOBAL WARMING ISSUE AND THE CARBON DIOXIDE DILEMMA

2.1 Carbon dioxide issue

Earth's climate system is powered by solar radiation. About 70% of the solar shortwave radiation (SWR) is absorbed by the Earth's surface and atmosphere, while the other 30% is reflected by gases and aerosols, clouds and Earth's *albedo* (superficial reflectivity, primarily due to ice covering) (see Figure 2.1.1). Due to the Earth's surface temperature, the majority of the emitted radiation is in the infrared part of the light spectrum. This emitted infrared longwave radiation (LWR) is largely absorbed by certain atmospheric constituents, as the water vapour, carbon dioxide (CO_2), methane (CH_4), nitrous oxide (N_2O), and clouds, which re-emit these LWR into all directions. A fraction of this radiation is emitted downwards and gets trapped below the outer atmosphere, creating a *greenhouse effect* responsible to heat the lower layers of the atmosphere and the Earth's surface.

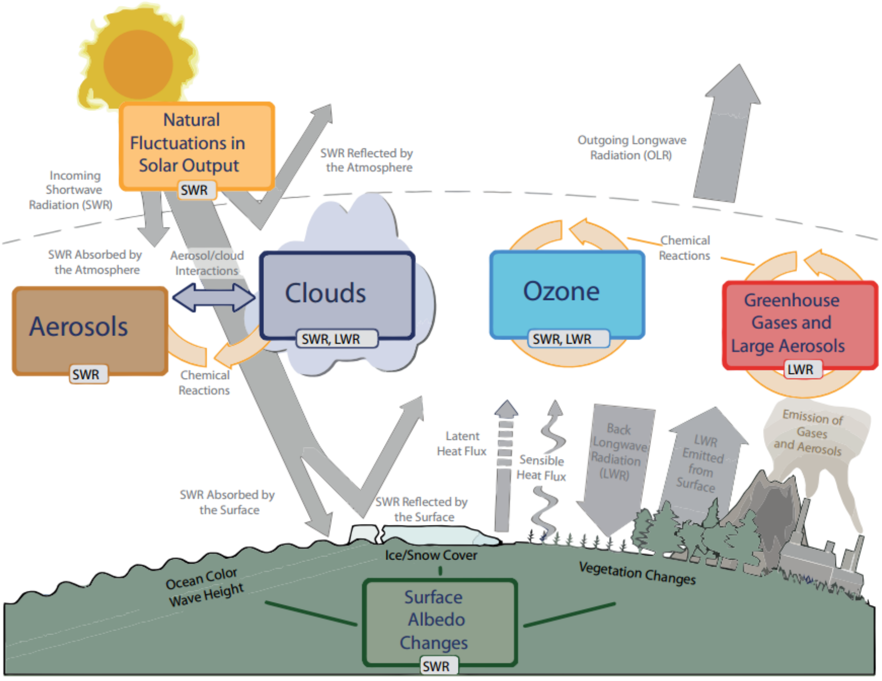

Figure 2.1.1 – Main drivers of climate change. The radiative balance between incoming solar shortwave radiation (SWR) and outgoing longwave radiation (LWR) is influenced by global climate 'drivers' [2].

Natural fluctuations in solar cycles can cause changes in the energy balance (through fluctuations in the amount of incoming SWR due to the 11-year sunspot cycles). Human activity also affects the Earth's *energy budget* by emitting aerosols which may change the atmospheric reflectivity (clouds albedo), and greenhouse gases (GHGs) such as CO_2, CH_4, N_2O, O_3 and chlorofluorocarbons (CFCs). In addition to the changes in the atmospheric concentrations of gases and aerosols, anthropogenic activities affect the energy and water budgets by changing the planet's land surface. Land uses, such as forestry and farming, adds carbon dioxide to the atmosphere and changes the reflectivity of the land (surface albedo), rates of evapotranspiration and longwave emission.

All this natural and anthropogenic changes in the planet's surface can cause a perturbation at the Earth's energy budget, producing a *radiative forcing* that affects the climate system. Internal feedback mechanisms may amplify or diminish the effects of a change in the climate system caused by the radiative forcing. Some of these feedback mechanisms operates within hour responses (*e.g.* the variation on the amount of water vapour on the atmosphere), though some others may develop over decades to centuries (*e.g.* the melting of ice sheets). In order to understand the full impact of a feedback mechanism, the timescales needs to be considered.

Since the components of climate systems respond on a large range of timescales, even if anthropogenic emissions were immediately ceased or if radiative forcing was fixed at the current value, the climate system would continue to change until it came into equilibrium with those forcings. Trying to foresee the radiative feedbacks, Earth System Models (ESMs) capable to explicitly simulate the biosphere, carbon cycle and atmospheric chemistry are used to project quantitatively the climate response to forcings. In order to achieve more realistic models, changes in the radiative forcing are applied over time, *e.g.* using historical reconstructions of CO_2. These transient simulations are typically based on increasing rates of $1\%\ yr^{-1}$ on the CO_2 concentrations of a coupled ocean-atmosphere model.

The processes affecting the climate system can exhibit natural variability on a vast range of spatial and temporal scales even in the absence of external forcing. In some cases, the relation between this variability, forcings and responses is complex and characterized by the dependence of past states (hysteresis). For these situations, the changes in the climate may be irreversible over some timescale and forcing range. Currently, the most comprehensive models shows no evidence of global-scale impasse during the 21th century, though, thresholds on the multi-centennial-to-millennial timescales are being reached in climate aspects such as ocean circulation and ice sheets.

Records of atmosphere, land, ocean and cryosphere systems supplies the database for the ESMs. Multiple climate indicators evidences a warming world from the atmosphere to the depths of oceans, as shown in Figure 2.1.2. The warming trend observed for the temperatures over land follows closely the trend presented for the oceans. Furthermore, recent measurements shows that the temperature of the lowest layers of the troposphere is increasing. The oceans keep storing the energy excess absorbed by the climate system, observed by the records of the oceanic heat content. The rise in sea levels, melting of glaciers and ice sheets are observed as an indirect result of the oceanic warming.

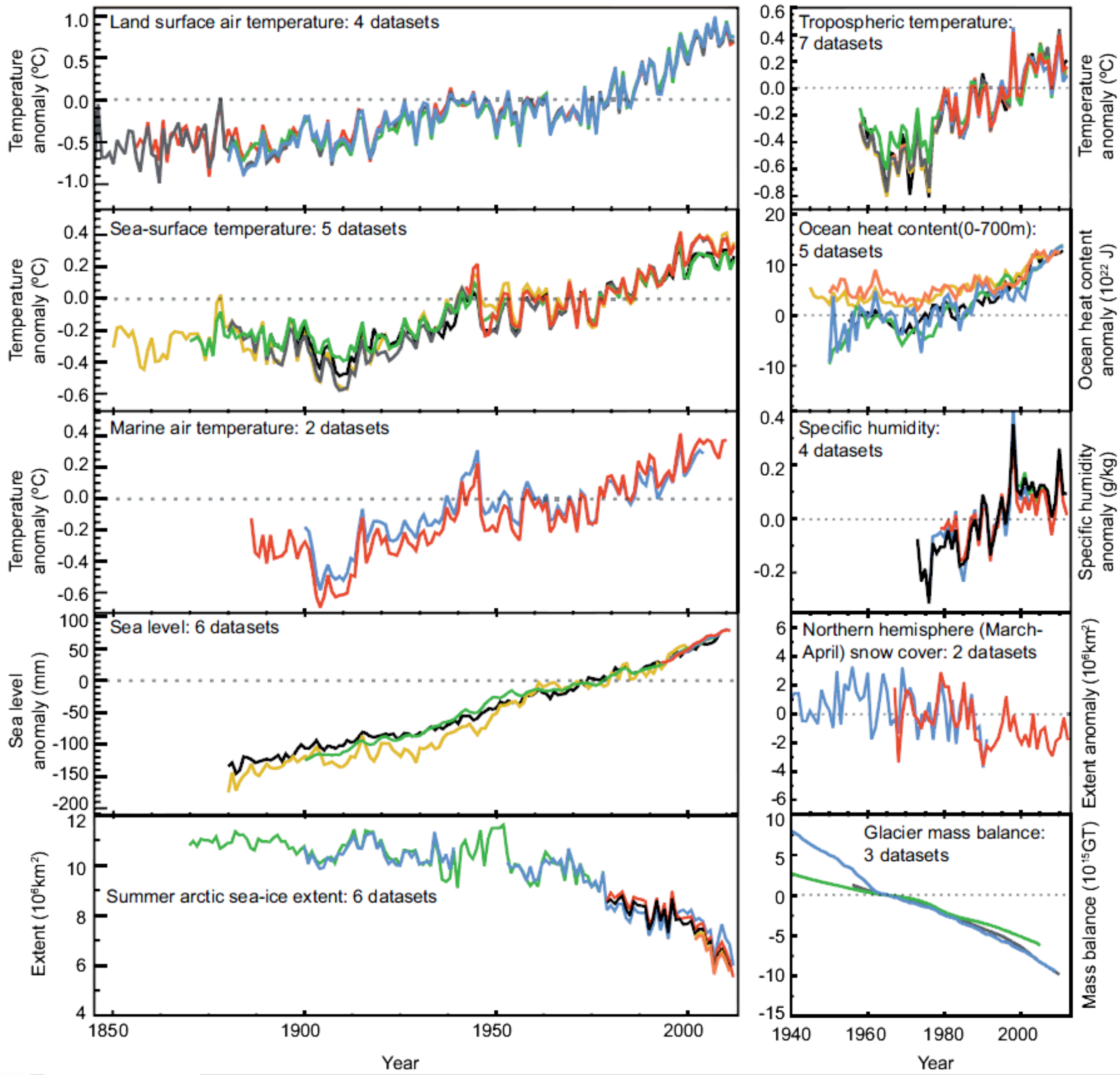

Figure 2.1.2 – Multiple independent indicators of a changing global climate. Each colored line represents an independently derived estimate of change in the climate element. In each panel all data sets have been normalized to a common period of record [3].

The trend presented in Figure 2.1.2 by the different indicators from independent data sets, leads independent research groups around the world to reach one same conclusion: the world has warmed since the late 19th century.

The economic and population growth has increased the anthropogenic GHGs emissions since the beginning of the industrial era. Despite the growing number of climate change mitigation policies promulgated worldwide, the increasing rate of GHGs emissions in the last decades (see Figure 2.1.3) is considered the major factor of the observed increase on the global average surface temperature. The oceans alone has absorbed about 30% of the emitted anthropogenic CO_2 in the 1750-2011 period, presenting an acidification process that decreased it's pH by 0.1 (corresponding to a 26% increase in acidity). This acidification process is altering the nutrients concentration on the seas, therefore leading to a shrinking process on the biological variety of the oceans [4]. About 40% of the GHGs emissions in this same period have remained in the atmosphere resulting on unprecedented atmospheric carbon dioxide concentrations over the last 800,000 years.

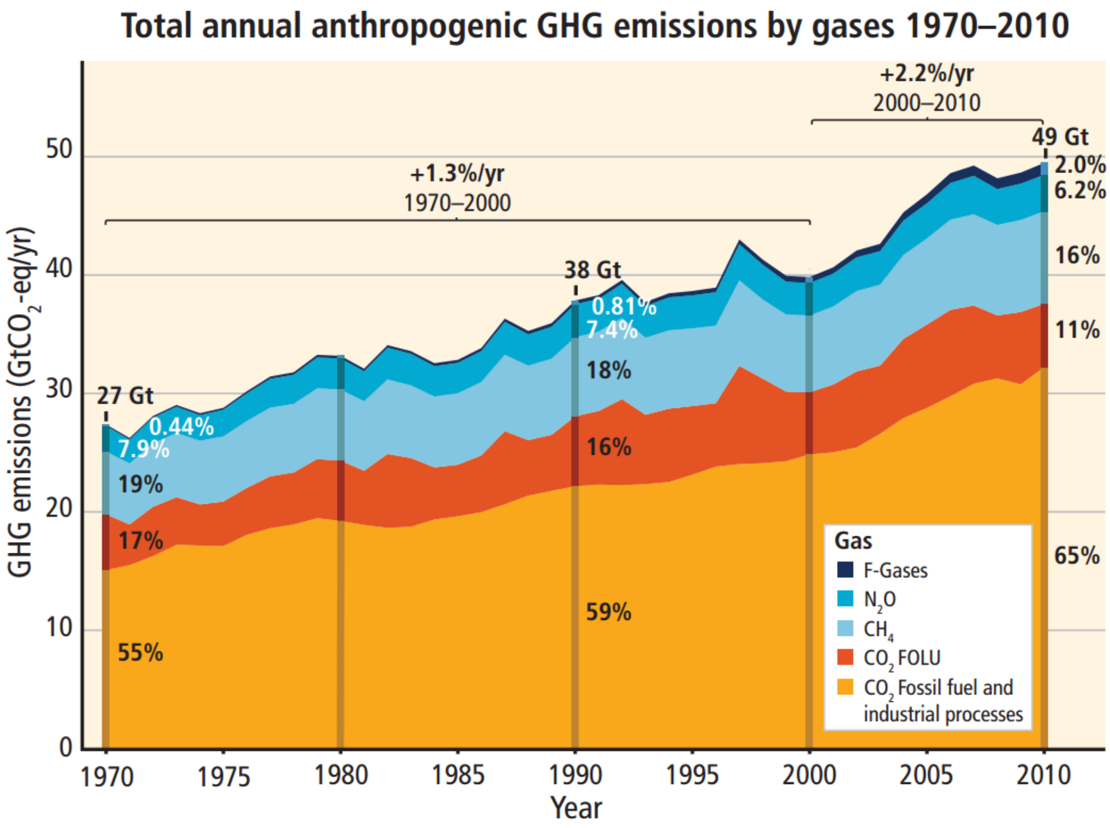

Figure 2.1.3 – Total annual anthropogenic GHGs emissions (gigatonne of CO_2-equivalent per year, $GtCO_2$-eq/yr) between 1970 and 2010 for: fluorinated gases covered under the Kyoto Protocol (F-gases); nitrous oxide (N_2O); methane (CH_4); carbon dioxide from Forestry and Other Land Use (CO_2 FOLU); and carbon dioxide from fossil fuel combustion and industrial processes [5].

2.2 Unraveling the CO_2 obstacle

Whereas high atmospheric carbon dioxide concentration is seen by part of the scientific community as a contemporaneous "villain", some researchers realize it as an alternative energy source since it is abundant, low-cost and a raw material [6]. In the last few years, new technologies have been developed focusing the conversion of *wasted* CO_2

into useful chemicals and fuels. This practice, known as Carbon Capture and Utilization (CCU), is still very expensive since it requires high energy substances such as H_2 to convert carbon dioxide into the most desired and useful chemicals, due to the high thermodynamic stability of the carbon dioxide molecule. Despite the high cost, more than 250 CCU projects are currently under development creating a niche industry capable to compete against petrochemical processes.

The CO_2 dissociation processes have been exhaustively explored due to its fundamental and practical significance in surface science, nanoscience and environmental science. Among the developing technologies, the leading processes in CO_2 dissociation are the RWGS reaction and the direct hydrogenation of CO_2. The direct hydrogenation of CO_2 was considered one of the most promising alternatives for industrialized methanol production [7], however, it yields smaller amounts of CH_3OH than that found in the RWGS process (which is thermodynamically less favored). Few CO_2 dissociation processes for low temperatures (< 500 °C) were reported, typically using noble metal-based catalysts [8]. The RWGS reaction is an endothermic process that occurs in many industrial reactions containing H_2 and CO_2, and has been exhaustively studied since it produces an important chemical feedstock (CO) under mild conditions.

In a recent study, Mallapragada *et al.* showed that the RWGS reaction already present the higher efficiency to convert atmospheric CO_2 into liquid fuels using sunlight, if compared to direct photosynthesis, biomass and algae self-contained or conversion processes [9]. The interest in the RWGS reaction is also related to space exploration research, by the association of high CO_2 concentrations found on Mars atmosphere to the H_2 formation as a byproduct on oxygen production processes.

2.3 The promising technology

The RWGS reaction (Eq. 2.1), first observed by Bosch *et al.* [10], is currently a key step in the methanation processes of CO_2. In addition to that, the RWGS reaction has the advantage of forming CO, which can be used as feedstock to produce a variety of chemicals, such as those used in *Fischer–Tropsch* processes. Additionally to the RWGS reaction, methanation (Eq. 2.2) and Sabatier (Eq. 2.3) reactions may occur in the H_2+CO_2 atmosphere.

$$CO_2 + H_2 \rightleftharpoons CO + H_2O, \qquad \Delta H_{298K} = 41.2\,kJmol^{-1} \tag{2.1}$$

$$CO + 3H_2 \rightleftharpoons CH_4 + H_2O, \qquad \Delta H_{298K} = -206.5\,kJmol^{-1} \tag{2.2}$$

$$CO_2 + 4H_2 \rightleftharpoons CH_4 + 2H_2O, \qquad \Delta H_{298K} = -165.0\,kJmol^{-1} \tag{2.3}$$

Due to the kinetic stability of the CO_2 molecule, CO_2 dissociation processes require efficient catalysts. As a result of its reversibility, the RWGS reaction often utilizes catalysts active in the Water-Gas Shift (WGS) reaction [11]. Historically, CO_2 dissociation processes utilizes noble metal-based catalysts (such as Ru, Rh, Pd, and Pt). However, Oshima *et al.* [1] studied the RWGS reaction on transition metal-based catalysts (Cu, Ni) supported on La-ZrO_2 and found good results towards CO selectivity at low temperature (150 °C). This study presented a smaller selectivity to CO for the nickel surface when compared to the copper one. Liu *et al.* [12], using DFT, showed that the Cu interaction with CO_2 is thermodynamically unfavorable.

Copper-based catalysts has the advantage of producing essentially no methane as a side product in the RWGS reaction. Due to its weak interactions with CO_2 molecules, CO_2 dissociation is highly unfavorable in the absence of hydrogen making needed the association of supports and/or promoters into the catalytic system. Chen *et al.* studied the association of Cu NPs to several metal oxide supports such as SiO_2 [13] and Al_2O_3 [14]. In the study involving a silica support, the high Cu dispersion enhances the CO_2 conversion to CO. Moreover, the Temperature Programmed Reduction and Desorption techniques (TPR and TPD, respectively) showed that the potassium association to the system's support creates new active sites which promotes CO_2 adsorption and CO production [15] enhancing the catalytic activity in the RWGS reaction. On the alumina supported case, the study proposed that the formation of CO is entirely related to the adsorption of formates species. Using the TPR technique, they observed a partial surface oxidation during the reaction and attributed this effect to the CO_2 dissociation, leaving O atoms bonded to the Cu surface. They also related the presence of hydrogen atoms at the Cu surface to an enhancement on the CO production. The enhanced activity promoted by hydrogen interactions with Cu surfaces was corroborated by an *in situ* XPS study by Fox *et al.* [16]. The analysis explored the promoter and support interactions in CuPd/CeO_2 catalysts, showing that Pd promoted the reduction of CuO clusters and CeO_2 by facilitating the hydrogen spillover.

Luhui *et al.* studied the effects of different Ni contents on Ni-CeO_2 catalysts for the RWGS reaction [17]. Using X-Ray Diffraction (XRD) and TPR techniques, they observed that low NiO loadings and high Ni dispersion are key components for a high catalytic activity in the RWGS reaction. Nickel-based catalysts have the advantage of being more stable at higher temperatures (such as 600 °C [17]) if compared to copper. A time-resolved XRD study made by Barrio *et al.* indicates that a strong interaction between Ce-O-Ni delays the reduction of nickel cations by hydrogen up to temperatures above 400 °C [18].

The usage of bimetallic catalytic systems attempts to achieve better performance, associating features of activity and selectivity coming from different materials. A natural association is copper and nickel, intending to combine the thermal stability from nickel to the high selectivity and activity of copper in a very reasonable system.

Liu *et al.* investigated the effect of variable (3:1, 1:1, 1:3, and 1:5) Cu/Ni ratio contents on Cu-Ni/γ-Al_2O_3 catalysts in the RWGS reaction [19]. The XRD analysis presented in this study relates the decrease in the Cu/Ni ratio to a stronger Cu-Ni interaction through oxygen transfer from the Cu oxides to the Ni oxide compounds. Moreover, the study relates the content of Cu to the CO production, while the content of Ni is related to the CH_4 production due to higher amounts of H_2 adsorbed at the Ni-rich surfaces. Derosa *et al.* performed a DFT study [20] which indicated that Cu-Ni bimetallic clusters yields stronger H bindings than Cu or Ni monometallic systems. However, among the bimetallic cases, copper clusters containing small concentrations of nickel are best adsorbers of hydrogen. This enhancement on the H_2 adsorption can improve the CO_2 conversion to CO, as shown by [15].

Several metal oxide supports were associated to metallic catalysts for the RWGS reaction. The support role on the RWGS mechanism is to stabilize the catalyst, avoiding phenomena such as agglomeration. Reducible oxide materials such as ceria (CeO_2) and titania (TiO_2) may interact with the NPs through oxygen exchange, which creates vacancies able to dissociate CO_2, enhancing the systems activity. Kim *et al.* compared the RWGS catalytic activity of Pt NPs supported on a reducible (TiO_2) and a non-reducible (Al_2O_3) support [21]. The system supported on a reducible oxide presented better results for the CO_2 conversion and CO selectivity due to the increase of the number of catalytic active sites with the appearing of oxygen vacancies. Pettigrew *et al.* showed that the oxygen vacancies play a key role towards the RWGS reaction when ceria is associated to Pd/Al_2O_3 systems, since it can re-oxidize with CO_2 exposition [22].

Kinetics studies involving cheap catalyst applied to the industry, such as copper [14, 15, 23, 24, 25, 26, 27] and nickel [27, 28], are among the trending topics on catalysis research nowadays. However, due to the high number of complex atomic events occurring during a catalytic reaction, the elucidation of catalytic events at the atomic level is still subject of intense research aiming the projection of new catalysts, more selective and sustainable.

2.4 Atomic level phenomena

The interaction between NPs surface, support, and reaction constituents during the catalyst exposition to the reactants are directly related to the catalytic activity. Phenomena such as diffusion of reactants through the catalyst surface, adsorption of reacting substances over catalysts surface, interactions between catalyst surface and reacting substances or support may influence the catalysts performance, improving or decreasing it [29]. A clean metallic surface is commonly desired for the NPs, since it presents catalytic sites typically more active. The adsorption of some reactants induce effects such as poisoning, sintering, and coke formation, causing catalysts deactivation. In the literature is showed that carbon deposition over catalysts plays a major role in the deactivation of Cu/CeO_2 and Ni/CeO_2 catalysts in the RWGS reaction conditions [30, 31]. This deactivation process occurs through a C covering of the supports active sites. This effect was also reported for Au [32, 33], and Pt NPs [34].

Form, size, texture (pore volume and density), surface area, and dispersion are some of the important intrinsic features of catalysts that are determined by the synthesis process. After synthesis, catalysts require activation before playing its role in the catalytic reactions. Most of the metal-based catalysts are activated by reduction processes, which leaves the particles clean and metallic, exposing the majority of the catalytic active sites. The reaction is favored in this active sites due to different chemical properties that enhances locally the chemisorption, such as a local lower activation energy promoted by the different electronic state in the catalytic site. Furthermore, these sites are typically related to the geometry of the surface and degree of crystallinity of the NPs since defects on the crystal structure, such as vacancies or dislocations, may alter the chemisorption properties of the NPs surface.

During the activation process and catalytic reaction, the exposition to some thermal or electrochemical condition may change some structural or electronic properties of the catalysts. In bimetallic systems, thermal annealing, electrochemical reactions, adsorption and desorption of reactants, or metal-support interactions may induce atomic migration to the catalyst's surface [35, 36, 37, 38, 39], giving rise to several possible atomic arrangements. The alloying extent in bimetallic NPs may generate totally separated phases, giving rise to monometallic clusters, or mixed phases in which several arrangements can occur. Mixed configurations include cases where the atoms of both species are present at random positions, at homogeneous distributions, or forming organized inner complexes such as core-shell, or layered (onion-like) atomic structures [40]. These arrangements are displayed schematically in Figure 2.4.1.

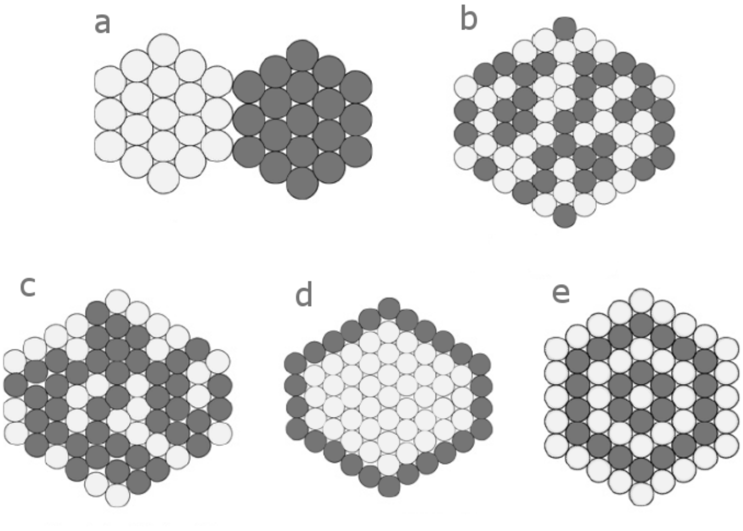

Figure 2.4.1 – Schematic representation of atomic arrangements in bimetallic NPs at various degrees of alloying. Different metallic species are presented as light and dark gray balls in (a) separated clusters, (b) random distribution (alloy), (c) small inner clusters, (d) core-shell, and (e) onion-like atomic structure (image adapted from [40]).

The surface segregation ability of a given specie is related to the particle's size, which influences on the surface-to-bulk ratio changing its alloying mechanism and differentiates the properties related to the particles surface and bulk [39]. The most common method to change the surface atomic population in bimetallic NPs is exposing the sample to a gaseous atmosphere under high temperatures [41, 42, 43, 44, 45, 46, 47, 48, 49, 50]. Ahmadi *et al.* studied atomic segregation in $Pt_{0.5}Ni_{0.5}$ NPs supported on highly oriented pyrolytic graphite (HOPG) under different gaseous environments (1 bar H_2, 1 bar O_2, and vacuum) using *in situ* XPS technique [51]. The results of this study can be summarized in the schematic representation presented in Figure 2.4.2. Initial *ex situ* Atomic Force Microscopy (AFM) measurements showed Ni-rich NPs surface due to the higher Ni affinity to the oxygen from the preparation environment. Following the shape change, the thermal treatment (≈ 500 °C) in oxygen led to a drastic Ni surface segregation which probably induced the formation of a thick and stable NiO shell and a small PtNi alloy core. The Pt segregation to NPs surface was observed under vacuum and hydrogen treatment above 270 °C and is related to the reduction of surface oxide species, creating a smaller surface free energy for Pt atoms if compared to Ni atoms.

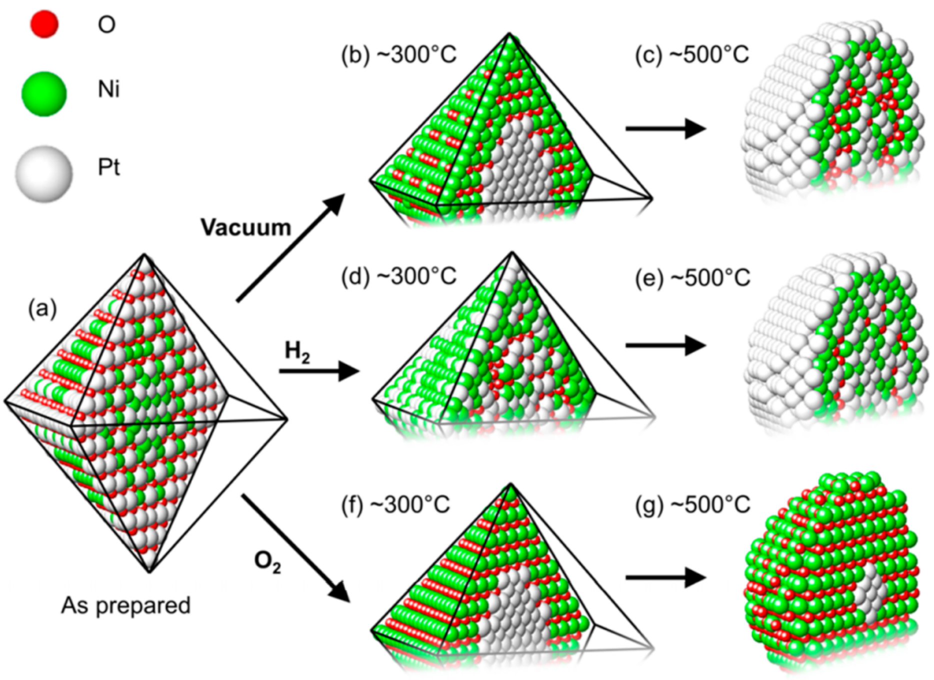

Figure 2.4.2 – Schematic representation of models describing the segregation phenomena of Pt and Ni atoms in octahedral $Pt_{0.5}Ni_{0.5}$ NPs (a) as-prepared and after annealing from 25 to 500 °C in the following environments: (b, c) vacuum (10^{-10} mbar), (d, e) H_2 (1 bar), and (f, g) O_2 (1 bar) [51].

For catalysis purposes, the bimetallic core-shell arrangement is the most desired one since it improves the physical and chemical properties of a material by combining multiple functionalities and providing new active interfaces, as well as synergic effects among components. Material engineering has made extensive efforts in order to design and to prepare controlled core-shell atomic structures. The techniques applied to obtain these atomic structures are most commonly based on precipitation, decomposition, surface enrichment, leaching or deposition. However, the segregation into separated core and shell phases relies on differences of physical and chemical properties such as reduction potential, affinity to adsorbates, etc. In particular, Cu-Ni bimetallic NPs have been synthesized by several different techniques [52, 53, 54, 55]. Cu has a lower surface free energy than Ni and is generally observed occupying the surface sites [56]. However, Wu *et al.* was able to prepare an alloy atomic structure with a Ni-rich surface by using a solvated metal atom impregnation technique [57].

Furthermore, the surface state of catalysts may also be influenced by interactions between NPs surface and the support. Different groups of supports (such as reducible oxides or refractory) revealed quite different catalytic activity and selectivity towards chemical reactions. In the reducible oxides case, the supported metals may interact strongly with the reducible support (Strong Metal-Support Interaction effect, SMSI), giving an almost complete inhibition of the capacity of CO and H_2 adsorption by the

NPs.

The SMSI effect is classically divided in the electronic and geometric factor, each one occurring in a given range of temperature [58]. The electronic factor occurs via charge transfer from the support to the metallic NPs supported. The geometric factor occurs with the migration of oxide moieties coming from the support to the surface of the NPs, then making a capping layer surrounding the NPs. Both effects occur during the activation of the catalyst under the reducing treatment.

Since its first observation by Tauster *et al.* [59], the mechanisms of metal encapsulation by the support are not yet fully understood for some supports, like CeO_2. Recently, several works have been developed aiming the elucidation of the nature of the SMSI effect [42, 46, 60, 61, 62]. One of them, proposed by Fu *et al.* in a study of the Pd/TiO_2 system using the XPS and Rutherford Backscattering Spectrometry (RBS) techniques [63], describes the encapsulation effect as a multi-step process: (i) electrons transferring from the oxide support surface to the metal NPs; (ii) mass transport of support's cations out of the crystal, into the near-surface region, driven by electrochemical potential difference between the support's bulk and the oxygen vacancies across the metal-support interface; (iii) mass transport of non-stoichiometric support portions (such as oxide moieties) onto the surface of the metal clusters by a thermodynamic process to minimize the surface energy. According to this model, the metal clusters deposited over the support must have larger work function than the oxide support, so that a charge transfer occurs at the materials contact, forming negatively charged metal particles. Labich *et al.*, studying Rh/TiO_2 model catalysts, correlated the occurrence of the SMSI effect to a surface energy minimization process [64]. Using Low-Energy Ion Scattering (LEIS) and XPS techniques, the authors described the minimization process to metal clustering and diffusion into the supports bulk.

The geometric factor of the SMSI effect (formation of the capping layer) is observed only for NPs exposed to a reduction treatment, when supported in reducible supports. Oi *et al.* described diagrammatically the reaction mechanism towards the covering process observed for the titania support [65]. As represented in Figure 2.4.3, a hydrogen-rich atmosphere can reduce the TiO_2 support's surface by removing some oxygen atoms to formate water. In response to that, the electron transferring phenomena charges negatively the metal clusters inducing the functional groups migration to particles surface. This capping layer drastically changes the chemisorption properties of metals and may form (or destruct) active sites, enhancing (worsen) the catalyst efficiency for the catalytic reaction.

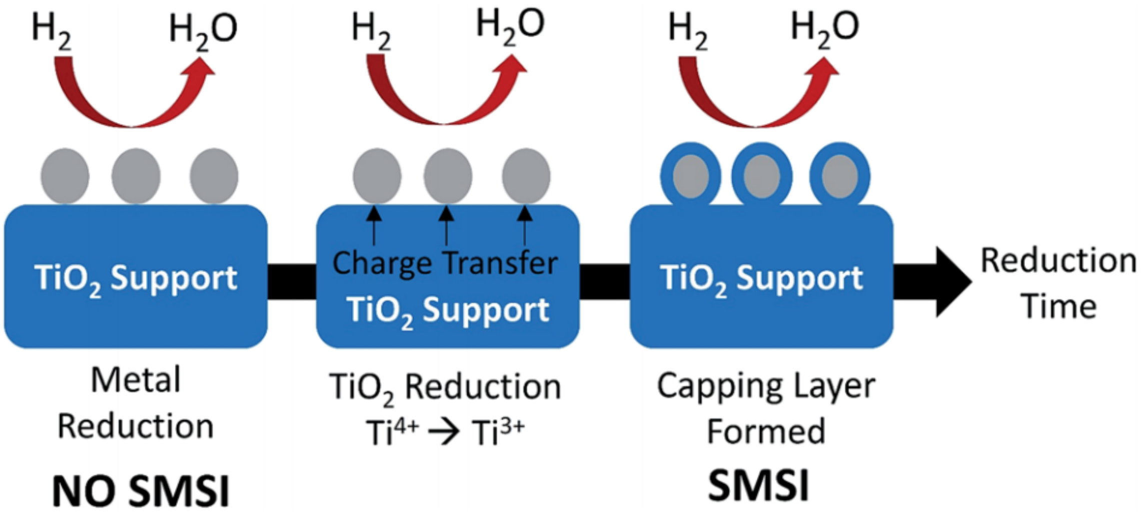

Figure 2.4.3 – Diagrammatic representation of the covering process due to the SMSI effect in a TiO_2 supported metallic NPs. During the H_2 treatment, water molecules are formed leaving oxygen vacancies as result of the support reduction. The reduced support transfers charge to the metallic clusters, which are covered by functional groups of support in order to diminish its surface energy [65].

Whereas the SMSI effect is widely explored and well understood for the TiO_2 case, little is known about the nature and reaction mechanisms for the CeO_2 supported systems. Zhuang *et al.* observed *via* TGA and TPR techniques, a decrease in the hydrogen chemisorption ability on the Ni/CeO_2 system after a high-temperature reduction treatment [66]. After oxidation and a low-temperature reduction treatment, the hydrogen chemisorption ability was restored. This behavior is typical of a SMSI [67]. In a previous work of our group, Matte *et al.* verified, using *ex situ* XPS measurements, the existence of the SMSI effect for the Ni/CeO_2 system after exposition to a 500 °C H_2 reduction treatment [60]. Figure 2.4.4 shows a High Resolution Transmission Electron Microscopy (HRTEM) image of the Ni/CeO_2 NPs after H_2 reduction treatment at 500 °C. It is possible to observe the caracteristic capping layer composed of cerium oxide surrounding the Ni NPs. Using the *in situ* time-resolved XAS measurements at the Ni K edge to compare the Ni oxidation state of supported and non-supported NPs, the authors observed a decrease of the Ni reduction temperature for the supported case and suggested an association of this effect to the electronic factor of the SMSI effect, with the charge transfer from the CeO_2 support to the Ni NPs. The electronic factor of the SMSI effect in this case helps the Ni NPs reduction with the charge transfer process. It was corroborated by *in situ* time-resolved XAS measurements at the Ce L_3 edge. Matte *et al.* also studied the influence of the CeO_2 support on the reduction properties of Cu NPs [60]. Differently from the Ni/CeO_2 system, Cu/CeO_2 NPs did not showed evidences of the existence of the SMSI effect. Consequently, no differences in the reduction temperature of supported and non-supported Cu NPs is found for this case. However, Liu *et al.* [68] and Dow *et al.* [69] reported strong interactions between Cu and CeO_2 supports using TPR measurements.

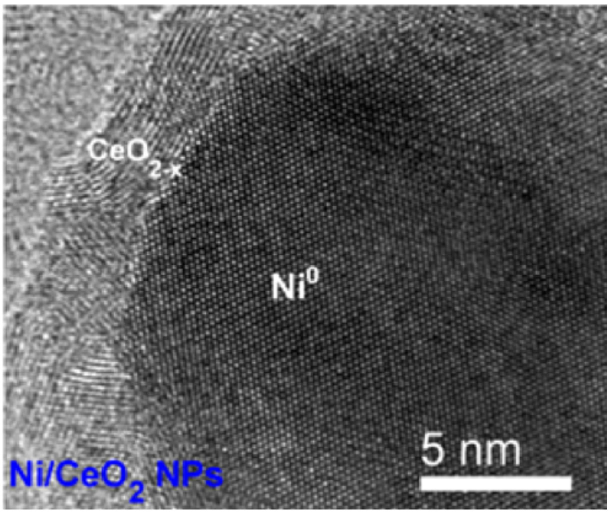

Figure 2.4.4 – HRTEM image showing the capping layer of cerium oxide surrounding the Ni(0) NP [60].

Moreover, the SMSI effect on ceria presented the ability to stabilize core-shell NPs by changing its segregation properties, as presented by Liu *et al.* in a study of Au-Pt bimetallic system using TPR and XPS techniques [70]. When exposed to a N_2 thermal treatment, the $Au_{0.5}Pt_{0.5}/C$ system presented Au segregation to NPs surface. The addition of CeO_2 modified the NPs surface energy and the Au segregation was inhibited even at high temperatures. It occurred because ceria anchored the Pt atoms (specimen presenting higher oxygen affinity) at NPs surface *via* Ce-O-Pt bonds (Pt for metal).

In another previous work of our group, Bernardi *et al.* studied $Rh_{0.5}Pd_{0.5}$ NPs supported on CeO_2 using Ambient Pressure X-ray Photoelectron Spectroscopy technique (AP-XPS) [42]. The authors presented high control of surface atomic population by the utilization of reducing and oxidizing atmospheric treatments in different temperatures. Using the AP-XPS technique, they showed that during reduction treatment (H_2) at 300 °C, Pd atoms migrate towards the NPs surface, but the exposition to an O_2 atmosphere causes a migration of Rh atoms towards the NPs surface. It occurs because Pd atoms have smaller surface energy than Rh atoms and Rh oxide is more stable than the Pd oxide compound. However, after a high temperature H_2 treatment at 480 °C, the change on the Pd or Rh surface enrichment is not observed anymore and the Pd atoms were freeze at the NPs surface. That is, even for exposition to an oxidizing treatment at 300 °C the Pd atoms remains at the surface of the bimetallic NPs. The reason for this behavior was attributed to the occurrence of the geometrical factor of the SMSI effect that changes the energy configuration at the surface of the NPs, keeping the Pd atoms at the surface during the oxidation treatment.

Despite all the complex phenomena related to atomic interactions in catalysts, studies aiming to model the kinetic processes of chemical reactions have been developed. Goguet *et al.* modelled the reaction paths in which CO_2 molecule may be dissociated *via* RWGS in the Pt/CeO_2 system [34]. Figure 2.4.5 presents the possible paths towards CO formation. Measurements of Mass Spectrometry and Diffuse Reflectance Infrared Fourier Transform Spectroscopy (DRIFTS) revealed that RWGS reaction occurs in the main route (indicated in Figure 2.4.5 as the "Carbonates" tab), in which carbonates interact with oxygen vacancies in the CeO_2 support, possibly leaving Pt-bounded carbonyls. While the process of CO_2 dissociation (through carbonates formation) is evidenced through the measurements, the oxidation of H_2 is not yet clear. A possible pathway involves the H_2 adsorption on Pt sites (CO free) followed by the migration of oxygen from the supported to the Pt-CeO_2 interface, allowing the reaction.

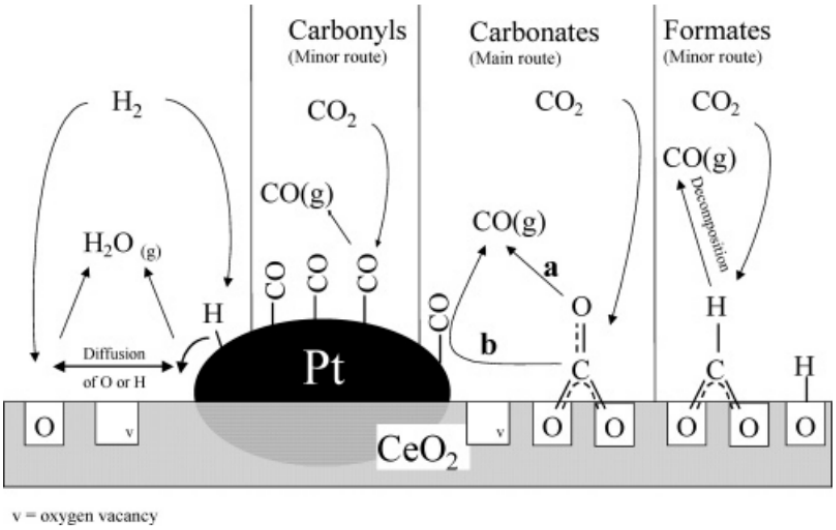

Figure 2.4.5 – Model for the reaction mechanism of the RWGS reaction over the Pt/CeO_2 catalyst [34].

Fujita *et al.* presented a model for the redox mechanism on Cu-based catalysts [24] under RWGS reaction. Based on XPS results, this model associates an oxidation process of metallic copper atoms promoted by CO_2 molecules, formating a Cu(I) oxidation state at the NPs surface, and a reduction process of the oxidized copper atoms promoted by H_2 molecules. Studies describing the reaction kinetics on Ni or bimetallic supported systems are still rare due to the number of simultaneous phenomena and the technical difficulties to probe the systems properties during the catalytic reactions.

2.5 Limitations of common characterization processes

Theoretical [71] and experimental [14, 15, 24, 72] models were proposed to represent the reaction kinetics, however *in situ* measurements were rarely used to explain these phenomena. Therefore, scientists struggle to confirm the reaction mechanisms forecasted in models and to understand the observed phenomena due to limitations of conventional methods, though, the arising of new technologies in research centers is enabling deeper and faster analysis of catalysts properties. For example, the development of devices that use synchrotron radiation allowed accurate analysis of some complex catalytic reactions. Due to its peculiar properties, this tool allows time-evolution studies for some analysis techniques.

Recently developed methods allows measurements for catalysts exposed to conditions close to the real ones, that is, high temperatures and high pressures of the reactant gases. A catalytic reaction is a sequence of several complex steps starting with the molecule adsorbing at a specific site on the surface of the catalyst and ending with the formation and the desorption of the final product. The detailed understanding of the events at the atomic level occurring during a catalytic reaction plays a fundamental role on the optimization and generation of advanced catalysts that can be applied in industry. However, the atomic structure and surface chemistry of catalysts under reaction conditions are usually very different from those studied under high vacuum or at low temperatures [73]. Thus, in order to understand the catalytic reaction mechanisms at the molecular or atomic level, *in situ* techniques have been applied successfully over the last few years [60, 73]. One of the best techniques employed to study the surface of catalysts is XPS. However, for a conventional XPS instrument, the samples must be maintained in an environment with a pressure lower than 10^{-7} mbar (high vacuum). In contrast, the NAP-XPS technique allows surface characterization of NPs when exposed to conditions closer to the actual reaction environment (high temperature ($\leq$1000 °C) and pressure ($\leq$ 25 mbar)) [74]. In this way, important scientific issues such as the surface atomic population and electronic properties of the surface have been addressed *in situ* [42, 61, 75]. Moreover, the *in situ* XAS technique is widely employed to probe the oxidation state and the short-range order around a specific atom of the NP when submitted to a catalytic reaction [60, 76]. Combining both techniques is a powerful approach that scientists can use to elucidate the catalytic properties of NPs. These level of analysis are take as the *state-of-the-art* in catalysis research.

3 PHYSICAL BACKGROUND ON THE ANALYSIS TECHNIQUES

This chapter is reserved to discuss the physical processes associated to the experimental procedures executed in this work. The properties of the as prepared NPs were investigated by EDS, XPS and TEM. When submitted to the catalytic reaction, Mass Spectrometry was applied to study the products formation while advanced *in situ* X-ray based techniques were used to understand the particle's properties.

3.1 Transmission Electron Microscopy (TEM)

The TEM technique [77, 78] is a broadly used technique in materials science providing informations as size and morphology [79] of nanosystems. The microscope operates by the same basic principles as light microscopes, but using electrons ($\lambda < 1$ nm) instead of light (400 nm $< \lambda <$ 700 nm) to achieve better resolution (light microscopes as a typical resolution of 150 nm, while in electron microscopes the resolution can be as smaller as 0.01 nm). An illumination source (or electron gun) at the top of the microscope emits electrons that travel through vacuum and are collimated by electromagnetic converging lenses into a small and coherent beam. This beam strikes the target sample and a portion is transmitted, refocused by objective lenses and projected onto a phosphorescent screen (or a CCD camera) at the bottom of the microscope, giving rise to a "shadow image" of the sample. The dark regions of the image displays high electronic density regions on the sample, where the electron is backscattered and do not pass through, while the white regions shows lower electronic density regions. All the other regions, displayed in shades of gray, are intermediate electronic density regions existing in the sample. Figure 3.1.1 presents a typical image of supported nanoparticles, specifically Cu-Ni bimetallic NPs supported on CeO_2.

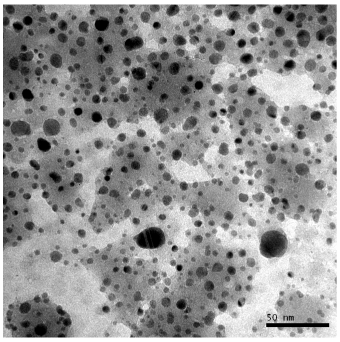

Figure 3.1.1 – TEM image of Cu-Ni NPs.

The EDS is an auxiliary technique, used in electron spectroscopy, which allows the determination of the sample's elemental composition.

When a high energy electron beam reaches a sample, some electrons undergoes inelastic scattering processes transferring energy to the sample by interacting with *phonons*, *plasmons*, or exciting other electrons. The electron excitation may cause *interband transitions* (migration from a occupied valence band state to an unoccupied conduction band state) or ionize the atom by ejecting an electron. Once an electron is emitted, its parent atom quickly decays from the excited state. The atomic relaxation occurs by "non-radiative" (Auger transitions) or "radiative" (fluorescence emission) processes, emitting an Auger electron or an X-ray, respectively.

In the radiative process, the energy conservation is fulfilled by the emission of X-rays. These X-rays, characteristic for each element, may pass through the sample and be absorbed by the detector (typically made of semiconductors as Si or Ge) where electron-hole pairs are created and generate a small current, proportional to the X-ray energy. Electronic processing of the pulses translates the current into a signal, in a specific channel, in a computer-controlled storage system. The final count in these energy channels constitutes the EDS spectrum, inferring a quantitative compositional profile of the sample.

3.2 Mass Spectrometry

Mass Spectrometry [80] is an analytical method used to identify compounds as well as to study ionization processes and dissociation of molecules.

The mass spectrometer (MS) can be divided in three fundamental parts, namely the ionization chamber, the analyzer, and the detector. Figure 3.2.1 displays a layout of the spectrometer.

In the ionization chamber, sample is kept in a high vacuum container (10^{-7} torr) where it can be ionized by diverse methods. A common procedure, called electron impact (EI), consists in the application of a high energy electron beam, which knocks electrons off the molecules creating positive ions. Repelled by the very positive voltage on the ionization chamber, ions enter into the analyzer passing through slits, a voltage gradient, being accelerated and collimated into a finely focused beam. This beam is driven through a magnetic field, and as result, the ions deflects in different angles depending on their masses and charges (lighter and more charged ions are more deflected). After deflection, ions reach a multichannel detector where metal plates neutralize them through electron transfers. The metal plates are connected by wire to amplifiers, and the electronic flows are detected as electric current signals, then amplified and recorded. The spectrum relates mass and its relative current intensity. Figure 3.2.2 shows the mass spectra from CO_2

and H_2O, where is also present the signals due to these compounds dissociation in the measurements (in the CO_2 spectrum: carbon, oxygen, carbon monoxide molecule, and carbon dioxide molecule; in the H_2O spectrum: oxygen, hydroxyl molecule, and water isotopes)

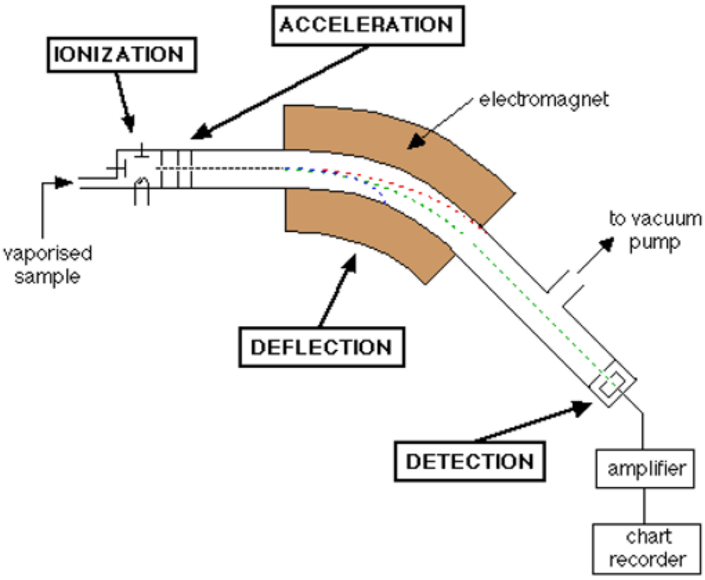

Figure 3.2.1 – Simplified schematic description of a MS [81].

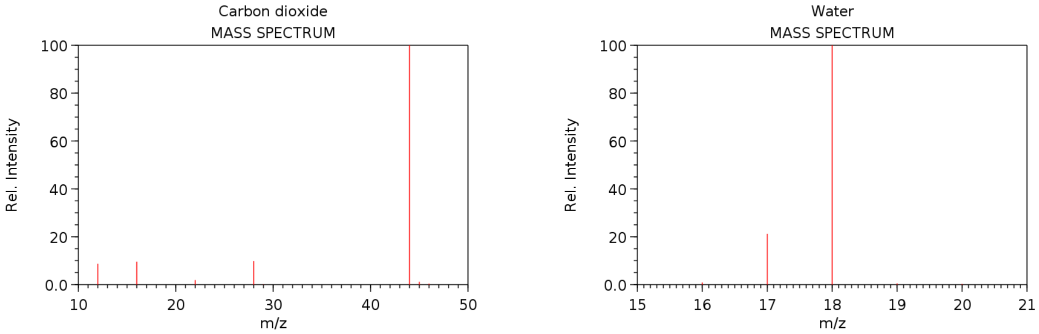

Figure 3.2.2 – Mass spectrum of CO_2 and H_2O showing relative intensities for the signals in the detection [82, 83].

In order to identify precisely a compound, is necessary to detect and analyze its isotopes signals, whereas different composites may present the same mass-to-charge ratio. The isotopes relative ratios can be found in databases, as that from the National Institute of Standards and Technology [84]. Features of a specific reaction kinetics can be investigated in a time-dependent measurement, since the time-resolved spectra indicate the evolution of each constituent during the reaction.

3.3 Synchrotron Radiation

The usage of synchrotron radiation [85, 86] has grown since its first observation, in 1947, and become a primary spectroscopy tool for the study of matter. This form of radiation occurs when a charged particle, moving at relativistic speeds, follows a curved trajectory due to the effect of a magnetic field which is perpendicular to its direction of motion. To produce synchrotron radiation, charged particles are initially accelerated up to millions of electron-volts (MeV) by a linear accelerator (Linac), then boosted up to billions of electron-volts (GeV) by a booster ring, and kept in ultra-high vacuum (10^{-9} torr) in storage rings. This ring consists of an array of insertion devices (wiggler and undulator), focusing devices (quadrupoles/sextupole magnets), and bending devices (dipole magnets), connected by straight linear sections (Figure 3.3.1). The curved path that the charges are forced in by the magnetic fields generates the electromagnetic radiative process causing energy loss in each turn at the ring. In order to restore the particles energy, radio frequencies cavities are installed, where the beam is splitted into small particle bunches by electric fields from the insertion devices. These bunches are transversely accelerated and radiate a pulsated light tangentially, in a concentrated narrow cone (due to relativistic effects).

Inside the ring, a charge may interact with other charges from the beam and some remaining gas molecules being scattered off. This gradual charge loss makes necessary a new charge insertion after typically 24 hours. To provide a more stable current, some synchrotron facilities utilize an injection mode, called top-up, where electrons are injected in the ring continuously.

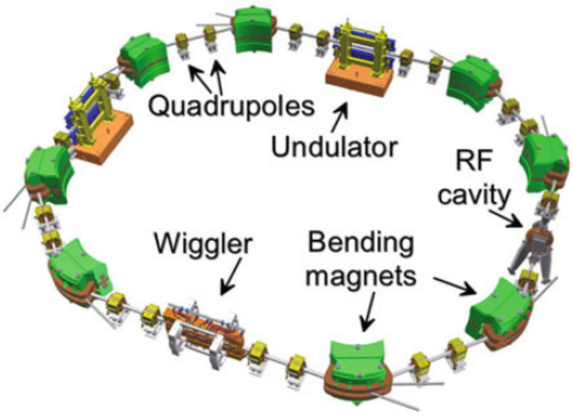

Figure 3.3.1 – Oversimplified scheme of a synchrotron storage ring, containing focusing magnets, insertion devices, and a radio frequency cavity [86].

The light emitted at the ring presents a wide range frequency spectrum (*i.e.* a large bandwidth) which is reduced to a smaller region when captured by the beamlines, located tangentially to the storage ring. In a typical hard X-ray beamline, the raw X-ray beam pass by mirrors to be focused, and by a monochromator to select the experimental energy according to Bragg's law. The experimental station is a custom-designed sample holder, where experimental conditions (*e.g.* atmosphere, pressure, reactants, temperature, etc.) are controlled, and data are recorded by detectors. Figure 3.3.2 shows a layout sketch of the DXAS beamline [87], dedicated to dispersive X-ray absorption spectroscopy techniques, in the hard X-rays energy range, at the Brazilian Synchrotron Light Laboratory (LNLS).

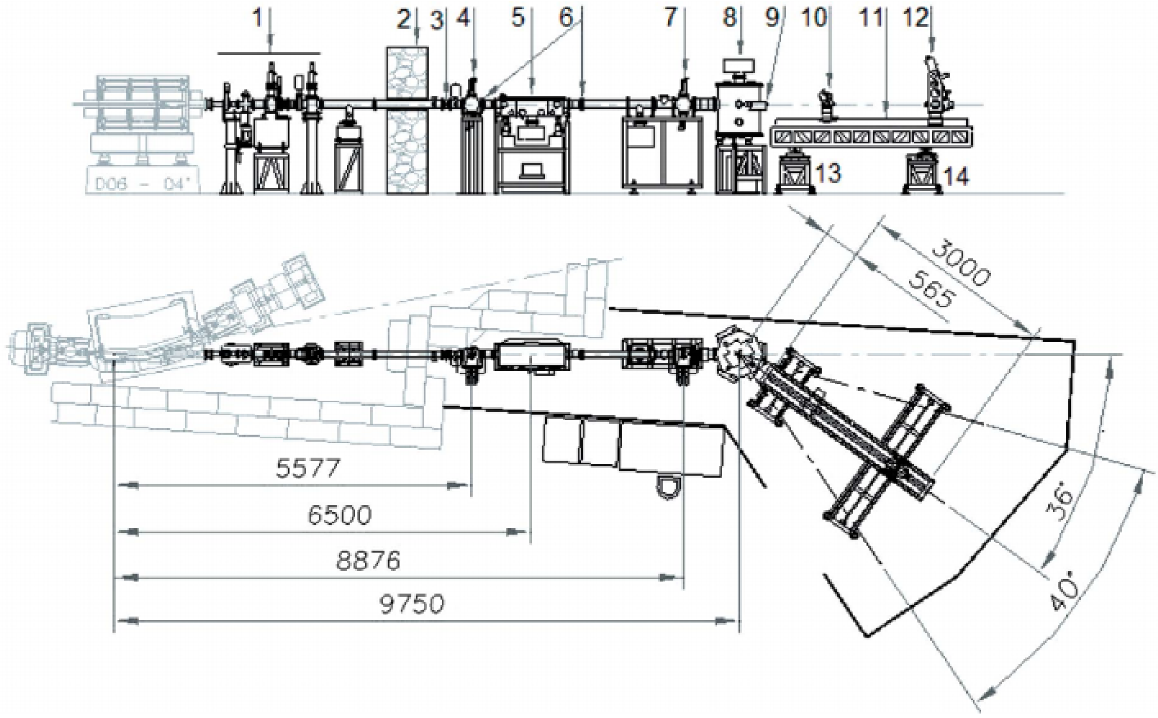

Figure 3.3.2 – Layout of the DXAS beamline at LNLS, installed in a bending-magnet port. The sequence indicates: (1) front-end, (2) wall shield, (3) cooled Be window, (4) cooled slits, (5) Rh-coated mirror, (6) two Be windows, (7) cooled slits, (8) monochromator, (9) beam shutter and large Be window, (10) sample holder, (11) optical bench, (12) modified CCD detector, (13) short linear stage and (14) long linear stage. Distances are in millimeters [87].

Overall, synchrotron radiation presents intrinsic advantages, such as

- High brightness: the photon flux per unit solid angle is hundreds of thousands times bigger than that produced by conventional X-ray tubes, for a given wavelength band.
- Wide spectral range: very broad and continuous, from infrared to hard X-ray region.
- Polarization: light is polarized by construction, being tunable in linear or circular polarization.
- Short pulsed time structure: pulses may be shorter than 10^{-12} s, providing possibility for time resolved studies.

These advantages make synchrotron-based techniques frequently in the state-of-art for several fields of the knowledge.

3.4 X-ray Photoelectron Spectroscopy (XPS)

The XPS [88, 89] is a widely used technique that provides chemical composition and electronic states of the elements at the sample's surface. This technique, based on the photoelectric effect, consists in irradiating a material with an X-ray beam while measuring the kinetic energy of the photoelectrons emitted from the core levels of the atoms in sample's surface.

In the photoemission process, schematically shown in Figure 3.4.1, the kinetic energy T of a detected photoelectron is

$$T = h\nu - E_b - \phi_{samp} \tag{3.1}$$

where $h\nu$ is the incident X-ray photons energy, ϕ_{samp} is the sample work function, and E_b is the electron's binding energy to the atom with respect to the Fermi level. In order to measure the kinetic energy of the ejected photoelectrons, it is used an energy analyzer which has itself a work function ϕ_{spec}. Once the sample is prepared for the measurements, both sample and electron analyzer are grounded an their Fermi levels are aligned. This connection set a potential difference equals to $\phi_{samp} - \phi_{spec}$, that accelerates the photoelectrons yielding an effective kinetic energy of

$$T = h\nu - E_b - \phi_{samp} + (\phi_{samp} - \phi_{spec}) = h\nu - E_b - \phi_{spec} \tag{3.2}$$

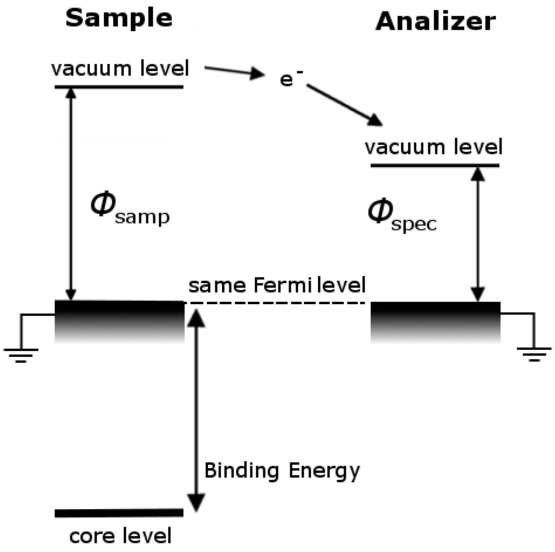

Figure 3.4.1 – Energetic level representation of the photoemission process, where ϕ_{samp} is the sample work function and ϕ_{spec} is the spectrometer's electron analyzer work function.

XPS spectra are commonly presented in electrons count (or intensity) as a function of binding energy [90, 91] (see Figure 3.4.2). Those excited electrons which escape without energy loss contribute to its characteristic atomic level peak, and those which suffer inelastic scattering contribute to the spectrum background. Peaks derived from orbitals whose angular momentum quantum number l is greater than 0, *i.e.* orbitals p,d and f, are usually split in two due to the interaction between electron's spin and orbital angular momentum. According to the total angular momentum number ($j = l \pm s$), orbital doublets (peak pairs) are denominated.

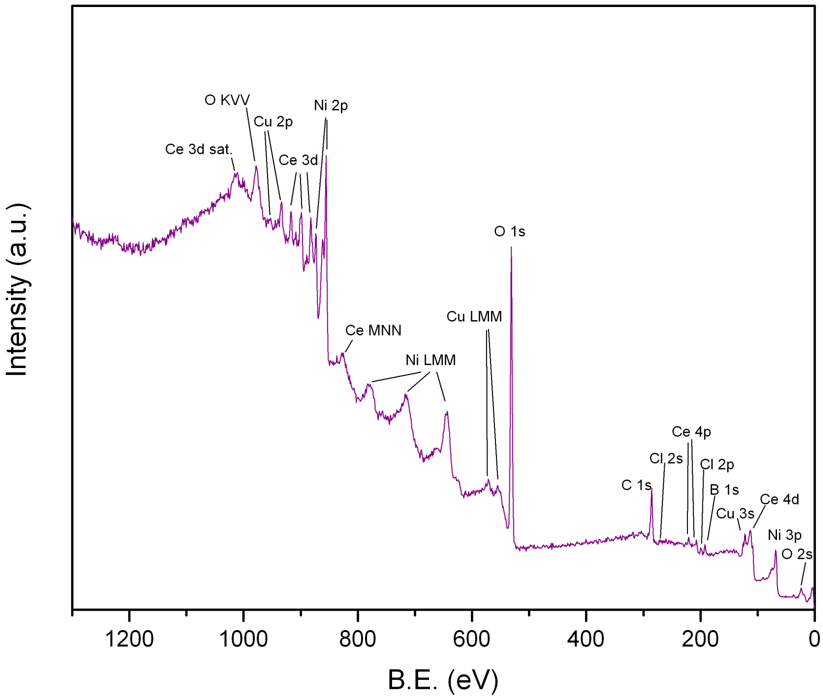

Figure 3.4.2 – XPS long scan spectrum of a Cu/CeO_2 NPs. Auger and photoemission peaks are identified.

The depth probed in XPS measurements varies with the kinetic energy of the electrons under consideration. It is determined by a quantity known as the electron's inelastic mean free path (λ_{IMFP}), that is defined as the mean distance traveled by the photoelectron before suffering an inelastic scattering in the sample. This behavior is well known for most of the solids and is shown in the universal curve (see Figure 3.4.3), which describes a model based on scattering theory [92, 93]. In the curve, is possible to observe that the depth typically probed in photoemission experiments is around tens of angstroms ($\lambda = 10$ Åat 500 eV kinetic energy).

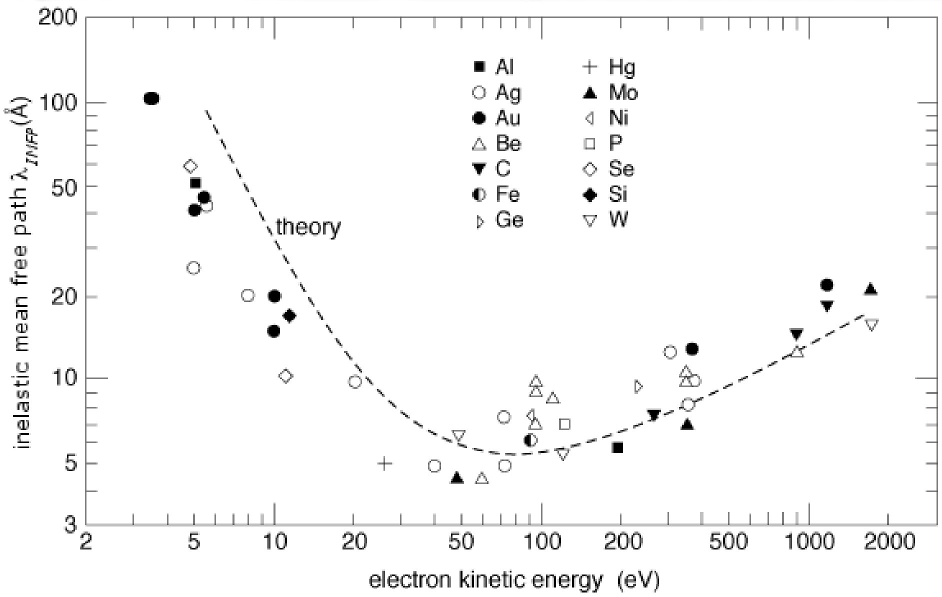

Figure 3.4.3 – A compilation of inelastic mean-free path values as a function of the electrons kinetic energy. The points, representing measurements of distinct elements, follows the "trend" set by the theoretical model (image adapted from [94]).

After the photoemission process, the core holes are refilled by outer shell electrons, and a secondary electron may be ejected to fulfill the energy balance in this relaxation process. This secondary electron, called Auger electron, is typically indexed over the atomic shells involved in the emission process, *i.e.*, an KLL Auger electron was bound to a L shell before being ejected after another L shell electron fill the K shell hole left by the photoelectron emitted. The Auger emission process is favoured for atoms with low atomic number. Moreover, since the Auger transitions are result of the atomic relaxation process, the Auger electron kinetic energy doesn't depends on the incident photon energy. Therefore, when a sample is measured in two different photon energies is possible to observe an energy shift in the Auger electron peaks that is not observable for the peaks associated to the photoemission process at the counts versus binding energy spectra (see 3.4.4). It occurs due to the transformation from kinetic energy to binding energy by using Eq. 3.2.

Conventional XPS systems uses radiation from Mg Kα (1253.7 eV), Al Kα (1486.7 eV), Ag Lα (2984.3 eV) or Cr Kα (5414.7 eV) X-ray sources. In some systems there are more than one X-ray source, providing a modest depth profiling capability (which can be improved by using a synchrotron radiation source by scanning more distinct depths) and ability to differentiate between Auger and photoelectric transition.

The emitted photoelectrons are usually collected by a hemispherical analyzer (HSA, see Figure 3.4.4). It consists of a pair of concentric hemispherical electrodes between which there is a gap for the electrons to pass. A voltage is applied across the two hemispheres, with the outer hemisphere being more negative than the inner one, forcing the electrons to travel in a circular path. The user-selected acceleration to the electrons defines the particles energy as they pass through the electron analyzer (called *pass energy*). The selected pass energy affects both transmission and resolution of the electron analyzer. A smaller pass energy results in a higher resolution while a bigger pass energy provides a higher electron transmission.

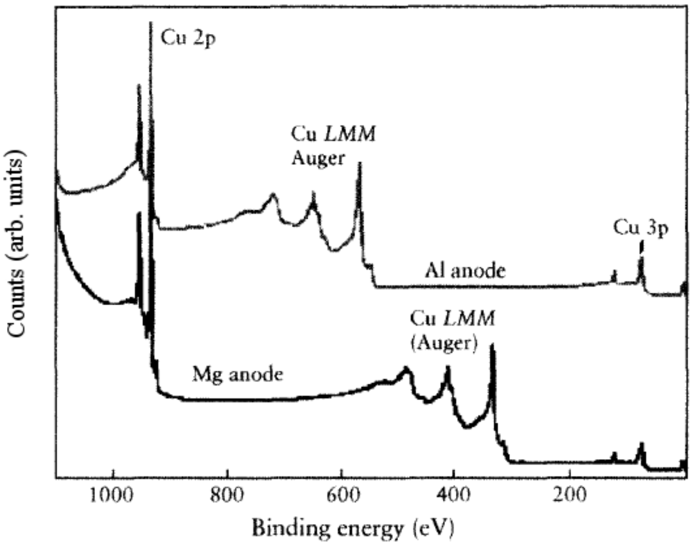

Figure 3.4.4 – Comparison of a copper foil XPS spectra recorded using both Al Kα and Mg Kα X-ray sources. Note that photoemission peaks remain at constant values and Auger peaks shifts about 230 eV by switching the radiation source [89].

Conventional XPS systems require measurements being carried out in ultra-high vacuum to avoid the electron scattering by gas molecules in sample-detector path, to avoid surface contamination during the measurements, and to keep the electron spectrometer running. However, the study of catalysts in ultra high vacuum may provide erroneous informations of the electronic and structural properties of systems that operates under high pressures and temperatures. Recently, electron spectrometers operating in high pressures and temperatures were produced. Measurements in such systems are named NAP-XPS and represent the state-of-art in the characterization of catalysts.

The use of NAP-XPS measurements for catalysts has a huge grown in the past last years around the world. This technique is not available currently in Brazilian laboratories. Considering synchrotron facilities, the X-ray beam may enters to the analysis chamber (AC) through a thin membrane (typically of Si_3N_4) or through a differentially pumped system, used to protect the vacuum in the beamline, causing a pressure difference of about

9 orders of magnitude between the analysis chamber and the storage ring. Inside the AC, the sample is placed and it's surface is brought close to a differentially-pumped aperture that connects the electron analyzer to the chamber. Across this aperture, pressure drops by several orders of magnitude by differential pumping, allowing the sample to remain in an ambient at a few tens of millibar pressure [95, 96].

The HSA operates in the constant analyzer energy (CAE) mode or constant retard ratio (CRR). In the CAE mode, every electron is accelerated (or retarded) to the same pass energy, presenting constant transmission and resolution throughout the entire spectrum width. For measurements in CRR mode, electrons are retarded to a ratio of its original kinetic energy, so the pass energy is proportional to its kinetic energy thus resolution decreases for higher binding energies. This resolution decrease is compensated by the increase in electron transmission.

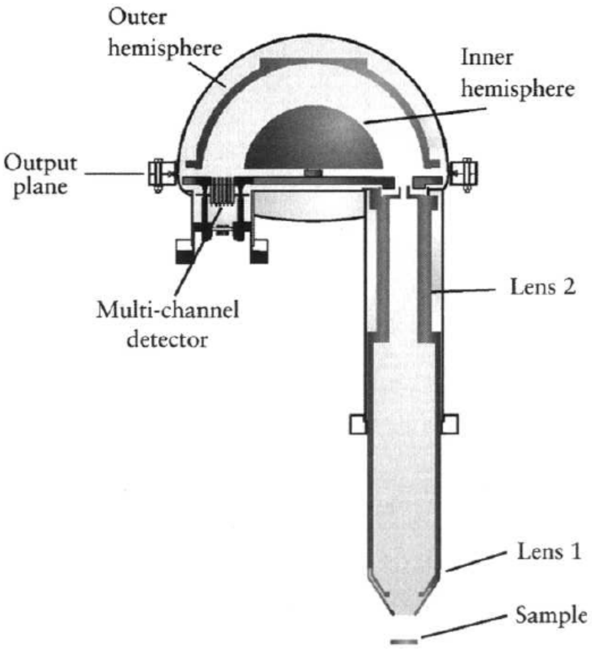

Figure 3.4.5 – A hemispherical sector analyzer layout [89].

In the detector, a multichannel collector coupled to a photomultiplier emits several secondary electrons in a cascade effect increasing the signals in about 10^8 times, thus creating a current recorded as the electrons counting. The spectrometer associates the electrons count and the correspondent binding energy of the detected particles.

The intensity I of a peak, related to the electron emitted from an atomic level nl

is given by

$$I_{nl} = J \cdot \frac{d\sigma_{nl}}{d\Omega}(h\nu) \cdot D(T_{nl}) \cdot \int_0^{\infty} \rho(z) \cdot \exp\left\{\frac{-z}{\lambda_{IMFP}(T_{nl}) \cdot cos\theta}\right\} dz \tag{3.3}$$

where J is the photon flux, $\frac{d\sigma_{nl}}{d\Omega}(h\nu)$ is the photoionization differential cross section, $D(T_{nl})$ is the efficiency of the detector at T_{nl} energy, z is the depth below surface, $\rho(z)$ is the concentration (atoms per volume unity) of the atom at z depth in the sample, $\lambda_{IMFP}(T_{nl})$ is the inelastic mean free path of the electron at T_{nl} energy, and θ is the electron emission angle in relation to sample's surface normal.

The photoionization cross section defines the probability of an electron to be ejected from the atom due to its excitation. This probability depends on the element, the orbital from which the electron is ejected, and the energy of the exciting radiation. Electrons in an initial state ψ_i have a probability to absorb an X-ray photon and transit to a final state ψ_f given by the Fermi's Golden Rule. This rule dictates the dipole selection rules (Δ l=$\pm$ 1; Δ m=0, $\pm$ 1; Δ s= 0, where l, m, and s are the quantum numbers associated respectively to the azimuthal, total, and spin angular momenta), and the transition probability is calculated as the matrix element $M_{if} = \langle\psi_i|\hat{H}'|\psi_f\rangle$. The electromagnetic radiation interaction with electrons can be described in the dipole approximation by the semi-classical Hamiltonian

$$\hat{H}' = \frac{-e}{2 \cdot m_e \cdot c}(\hat{p} \cdot \hat{A} + \hat{A} \cdot \hat{p}) \tag{3.4}$$

where e is the electron charge, m_e is the electron mass, c is the light speed, $\hat{p}$ is the momentum operator, and $\hat{A}$ is the vector potential operator. The matrix element is then calculated by

$$|M_{if}|^2 \propto |\langle\psi_i| \sum_{j=1}^{N_e} \hat{A} \cdot \hat{p}^j |\psi_f\rangle|^2 \tag{3.5}$$

where the sum is made over the number of transitioning electrons, N_e. The differential cross section $\frac{d\sigma_{nl}}{d\Omega}(h\nu)$ is the probability to detect the photoelectron in a specific angle on the detector. The detection for all possible angles ($\Omega = 4\pi$) gives the total cross section $\sigma_{nl}(h\nu)$ calculated as

$$\sigma_{nl}(h\nu) = \int_0^{4\pi} \frac{d\sigma_{nl}}{d\Omega}(h\nu) d\Omega \tag{3.6}$$

The differential cross section for linearly polarized light is

$$\frac{d\sigma_{nl}}{d\Omega}(h\nu) = \frac{\sigma_{nl}}{4\pi} \cdot \left[1 + \frac{\beta_{nl}}{2}(h\nu) \cdot (3cos^2\alpha - 1)\right] \tag{3.7}$$

where α is the angle between the polarization vector and the electron detection direction, and β is the angular asymmetry factor related to the anisotropy in the photoemission due to interaction with neighbour atoms.

3.5 X-ray Absorption Spectroscopy (XAS)

The XAS technique [97] is an analytical technique used to investigate the local atomic structure and electronic states in crystalline or amorphous materials, through measurements in solid or liquid samples.

The XAS technique consists in the measurement of the X-ray absorption coefficient as a function of the incident photon energy. Focusing an X-ray beam of intensity I_0 on a sample, the intensity of the transmitted radiation will depend on thickness and absorbance of the sample. This relation, known as Beer's Law, is

$$I_T(z) = I_0 e^{-\mu(E) \cdot z} \tag{3.8}$$

where I_T is the transmitted intensity, $\mu(E)$ is the energy-dependent absorption coefficient, and z is the thickness of the sample.

Figure 3.5.1 shows a typical XAS spectrum measured for a Cu sample at the Cu K edge, which corresponds to a electron transition from the 1s level to the 4p level. When the incident photon energy is lower than a given electronic binding energy, the absorption process for this electronic level does not occurs. When increasing the incident photon energy to a value higher than the electronic binding energy, there is an abrupt increase on the absorption coefficient. The region of this abrupt increase on the absorption coefficient is named absorption edge. Absorption edges are named in accordance to the principal quantum number of the electron associated to promoting shell: K for n=1, L for n=2, M for n=3, etc.

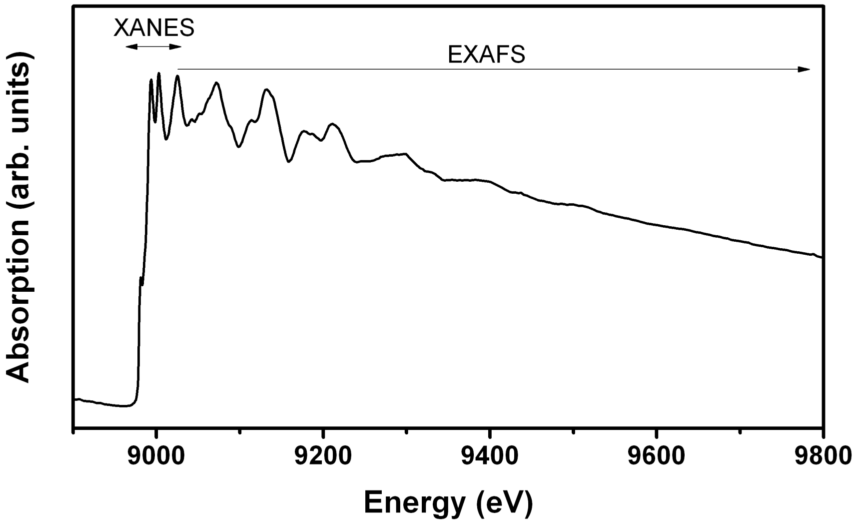

Figure 3.5.1 – XAS spectrum at the Cu K edge, evidencing XANES and EXAFS regions.

The oscillatory behavior observed after the absorption edge are result of interactions between the photoelectron with the neighborhood of the absorbing atom.

For a single isolated atom, the absorption coefficient would be a monotonic decreasing function of energy. However, the emitted photoelectron is understood as a spherical wave and backscatters in the atoms at its neighborhood (see Figure 3.5.2). The interference caused between the incident and the backscattered photoelectron waves changes the behavior of the absorption coefficient, creating an oscillatory pattern depending on the atomic number, position, disorder, and number of neighbors, as well as the wavelength associated to this photoelectron.

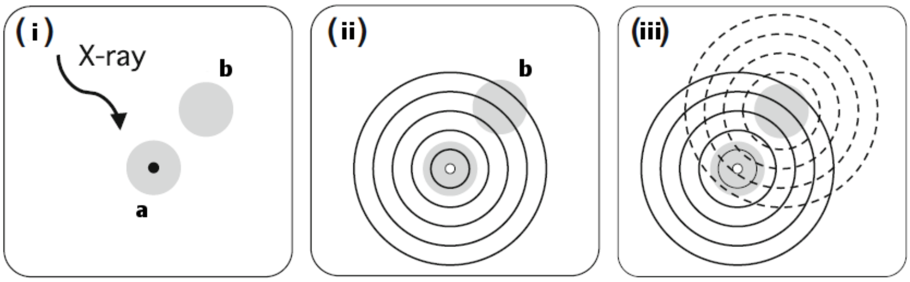

Figure 3.5.2 – Schematic representation of the backscattering phenomenon: **(i)** the X-ray photon arrives in the atom a (the black circle represents the orbital of the core electron), **(ii)** the photoelectron is seen as a spherical wave by the neighbour atom b(the open circle represents the core hole of the atom a), **(iii)** the atom b scatters the photoelectron's wave (dashed lines) [86].

The kinetic energy of the photoelectron is

$$\frac{p^2}{2m_e} = T = h\nu - E_b \tag{3.9}$$

where $h\nu$ is the energy of the incident X-ray, and E_b is the binding energy of the electron in the atom. The wave associated to the photoelectron has a wave vector k of

$$k = \frac{2\pi p}{h} = \frac{\sqrt{2m_e(h\nu - E_b)}}{\hbar} \tag{3.10}$$

The XAS spectrum is divided in two regions: the XANES (X-Ray Absorption Near Edge Structure) and the EXAFS (Extended X-Ray Absorption Fine Structure) region. The XANES region comprises the region from the absorption edge up to around 50 eV after the absorption edge. The EXAFS region is defined between the end of the XANES region up to the end of the XAS spectrum, typically 1000 eV after the absorption edge. XAS experiments can also be performed in time-resolved mode and for *in situ* conditions, *i.e.*, recording data with the sample exposed to real conditions (high pressure and temperature). The combined use of NAP-XPS and *in situ* XAS measurements is the *state-of-the-art* for catalysis research. In order to make an *in situ* time-resolved study, the X-ray absorption spectroscopy technique is performed in dispersive mode, known as

DXAS. Typically, a curved crystal focuses a synchrotron X-ray beam onto the sample. In this geometry, the continuous variation of the incident angle in the crystal selects an energy band, creating a polychromatic beam, capable to perform simultaneously the measurement of the complete XAS spectrum. The transmitted X-rays are dispersed onto a position-sensitive detector, typically a *CCD*, allowing a fast measurement of the spectra.

3.5.1 Extended X-ray Absorption Fine Structure (EXAFS)

In the EXAFS region, photoelectrons have their de Broglie wavelength comparable to interatomic distances. The EXAFS oscillations, $\chi(k)$, contains information about the coordination number, interatomic distances, and thermal and structural disorder in the neighbourhood of a particular atomic specie. $\chi(k)$ is usually defined as the fractional modulation in the X-ray absorption coefficient

$$\chi(k) = \frac{\mu - \mu_0}{\mu_0} \tag{3.11}$$

where μ is the observed absorption coefficient, and μ_0 is the absorption coefficient expected for a single isolated atom. This single atom contribution cannot be measured, so it is approximated by the fit of a smooth spline function through the data.

Extracting the single atom contribution, $\chi(k)$ can be described as

$$\chi(k) = \sum_s \frac{N_s \cdot A_s(k,\Theta) \cdot S_0^2 \cdot exp(-2k^2\sigma_{as}^2) \cdot exp\Big(\frac{-2R_{as}}{\lambda(k)}\Big)}{k \cdot R_{as}^2} \cdot sin\Big(2kR_{as} + \phi_{as}(k)\Big) \tag{3.12}$$

where the summation is taken over all the atomic shells s around the absorber a. The parameters used in the equation 3.12 are the absorber-scatterer distance for a s shell, R_{as}, the coordination number for a shell s, N_s, the photoelectron scattering amplitude in the angle Θ, $A_s(k,\Theta)$, an amplitude correction term to consider the inelastic loss processes, S_0^2, and the phase-shift caused by the scattering processes, $\phi_{as}(k)$.

The EXAFS sinusoidal amplitude decreases as R^{-2}, as a result of the spherical wave propagation. It's signal oscillates in a frequency $2kR_{as}$ proportional to the interatomic distances with phase shift $\phi_{as}(k)$. The first exponential term reflects the fact that different absorber-scatterer distances contributes in different frequencies, causing a partial destructive interference that damps the amplitude of the oscillations. The second exponential term is a damping component related to the mean distance covered by the photoelectron in the solid, $\lambda(k)$, depending on the inelastic mean free path and the finite life time of a hole state, limiting the distance around the absorbing atom that can be probed by EXAFS measurements. The root-mean-square deviation in absorber-scatterer distance is called Debye-Waller factor, σ_{as}^2.

During the analysis of the EXAFS oscillations, a Fourier analysis method [98, 99] is applied describing quantitatively the absorbing atom's local structure. The Fourier

Transforms (FT) deconvolutes the $\chi(k)$ signal in the collaborative different frequencies, defining a pseudo-radial distribution function. The peaks presented in $\chi(k)$'s FT represents the atomic shells around the absorbing atom (positioned in R=0 Å).

The approach used to describe the multiple-scattering effects presented in EXAFS data is based on *ab initio* calculations that are used to determine the phase shift and the scattering amplitudes. The effective potential used in these calculations consists in the addition of an energy functional (analogous to the exchange-correlation potential used for ground state calculations [100]) to the Coulombian potential, presenting the *muffin-tin* geometry (see Figure 3.5.3) in which the atoms are the center of spherical scattering potentials connected to the neighbours by a constant potential interstitial region.

The actual potential of a solid (or cluster of atoms) is more complex but the atomic-like spherical approximation in the *muffin-tin* potential is appropriated close to the nucleus. In the outer regions of the atom, the bonding (ionic, covalent or metallic) generates anisotropies in the actual potential but the high kinetic energy of the photoelectrons decreases their sensitivity to features of the atomics potential edges. As the electrons are mainly scattered in the inner regions of the atomic potential moving approximately free in the interstitial regions, the *muffin-tin* geometry provides a good approximation for the EXAFS region.

The potential near the atomic nucleus depends on the local charge density. In the *muffin-tin* geometry, most of the charge density is due to the atom in the center of the potential, with small contributions in the outer parts due to neighbouring atomic charge distributions. In order to describe the effective potential, the most often used idea approximates this potential to the ground-state by placing a neutral-atom in each atomic center and overlapping their charges densities to obtain the total charge density around a given atom, though an average spherical symmetry is kept by the *muffin-tin* approximation in the inner region.

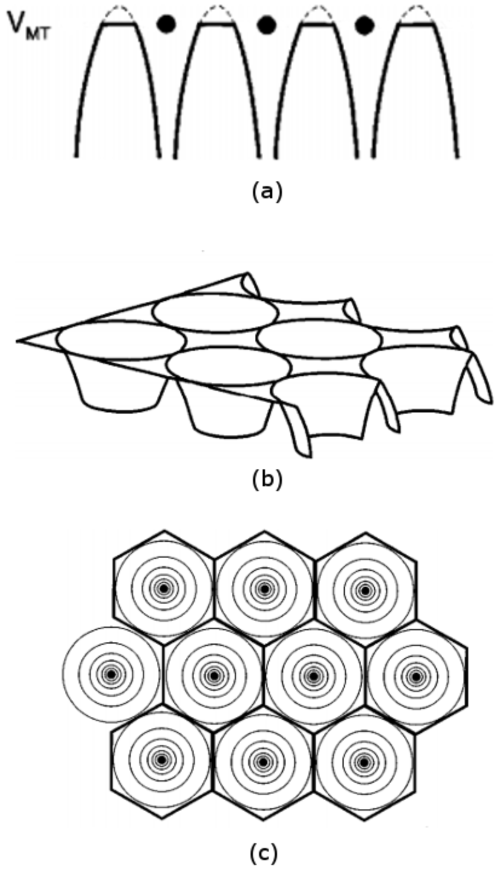

Figure 3.5.3 – (a) One-dimensional representation of the *muffin-tin* potential profile, where the solid lines between the atoms (black balls) shows how the flat interstitial potential truncates the true shape of the potential (dashed lines). (b) Two-dimensional drawing representing the motive of this potential is named *muffin-tin.* (c) Two-dimensional schematic representation of the spherical approximation inside a Wigner-Seitz cell centered around each atom. It illustrates how the effect of spherical *muffin-tin*-like approximations of real crystals (the figures were redrawn, based on [101]).

Inelastic losses in the multiple-scattering effects may involve *intrinsic* or *extrinsic* processes. *Extrinsic* losses are referred to the photoelectron propagation and are described in terms of a complex valued and energy dependent operator ($\Sigma(E)$) that arise from exchange interactions between the photoelectron and the system. The real part of $\Sigma(E)$ accounts for the shifts of the EXAFS oscillations compared to the ground-state positions, while the imaginary part gives rise to the inelastic mean free path. *Intrinsic* losses refer to excitations arising due to the creation of a core hole in the photoabsorption process. *Intrinsic* processes generally involves more than one excited electron (*e.g.* shakeup and shakeoff excitations) and to relax the $N-1$ excited electrons, secondary emissions occurs. Since these two processes share the same final state, their amplitude may interfere damping the EXAFS oscillations.

In the Green's-function formulation of multiple-scattering theory, inelastic losses are naturally accounted in the *quasiparticle* behavior of the photoelectron as it moves though the potential. This formalism also has the advantage of avoiding the necessity to calculate the wave-functions. The description of the X-ray absorption coefficient is made in terms of a one-particle Green's-function

$$G(E) = \frac{1}{E - H + i\Gamma} \tag{3.13}$$

where Γ describes the net life time of the photoelectron, including both extrinsic and intrinsic losses, and the one-particle Hamiltonian H includes the core hole screening effect. Using a spectral representation of the Green's-function in the positional space

$$G(\mathbf{r}, \mathbf{r}_f; E) = \sum_f |\psi(\mathbf{r}_f)\rangle \frac{1}{E - H_f + i\Gamma} \langle\psi(\mathbf{r}_f)| \tag{3.14}$$

the absorption coefficient from a given core level $|\psi(r_c)\rangle$ can be described as

$$\mu_c(E) = -\frac{1}{\pi} Im\langle\psi_c|\hat{\epsilon}\cdot\mathbf{r}G(\mathbf{r}, \mathbf{r}_f; E)\hat{\epsilon}\cdot\mathbf{r}_f|\psi_c\rangle\theta_\Gamma(E - E_F) \tag{3.15}$$

where θ_Γ is a broadened step function at the Fermi energy E_F. The resemblance of the equation 3.15 with the Fermi's Golden Rule is due to the proportion relation between the absorption coefficient and the absorption cross section: $\mu_c = n_c\sigma_c$, where n_c is the density of atoms within the concerning core level c.

In the *muffin-tin* approximation, the photoelectron Hamiltonian H_f is given by

$$H_f = T + V_a + \sum_{n\neq a} V_n \tag{3.16}$$

where V_a is the ionized atom potential in its relaxed state, and the V_n are the neighbouring atoms potentials. This description allows a reinterpretation of the Green's-function propagator G describing separately the collaborations from the single atom emission from the single and multiple scatterings of the photoelectron in the neighbourhood of atom A. Thus, the absorption coefficient is given by

$$\mu_c(E) = -\frac{1}{\pi} Im\langle\psi_c|\hat{\epsilon}\cdot\mathbf{r}[G_a + G_a\tau G_a]\hat{\epsilon}\cdot\mathbf{r}_f|\psi_c\rangle\theta_\Gamma(E - E_F) \tag{3.17}$$

where G_a is the Green's-function propagator related to the photoemission

$$G_a = \frac{1}{E - T - V_a + i\Gamma} \tag{3.18}$$

and τ is the complete scattering operator.

$$\tau = \sum_{\substack{n\neq a\\ n\neq b}} V_n + \left(\sum_{n\neq a} V_n\right) G \left(\sum_{m\neq b} V_m\right) \tag{3.19}$$

Separating the contribution from each given atom n in the scattering operator

$$t_n = V_n + V_n G_n V_n \tag{3.20}$$

is possible to rewrite 3.19 in terms of the free-space Green's-function $G_0 = 1/(E - T + i\Gamma)$ through perturbation theory by applying the identity $V_n G_n = t_n G_0$, so

$$\begin{aligned} \tau = \sum_{n \neq a} t_n + \sum_{n \neq a} t_n G_0 \sum_{\substack{m \neq n \\ m \neq a}} t_m + \sum_{n \neq a} t_n G_0 \sum_{m \neq n} t_m G_0 \sum_{\substack{k \neq m \\ k \neq a}} t_k \\ + \sum_{n \neq a} t_n G_0 \sum_{m \neq n} t_m G_0 \sum_{k \neq m} t_k G_0 \sum_{\substack{j \neq k \\ j \neq a}} t_j + \ldots \end{aligned} \tag{3.21}$$

Eq. 3.21 can be replaced in eq. 3.17, describing the propagation from the photoelectron from the atom a to the atom j, then scattering there (t_j) and propagating in free-space to the atom k, m, n, and back to atom a. The figure 3.5.4 shows a representation of different paths that the photoelectron may propagates through the material.

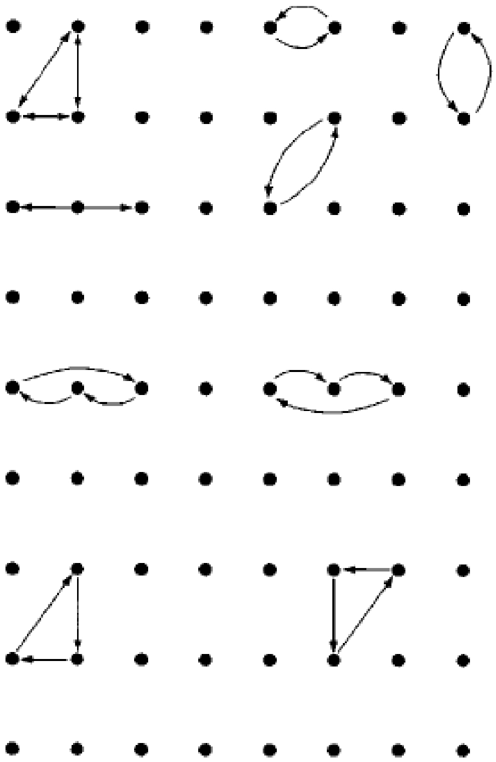

Figure 3.5.4 – Different possible paths followed by a photoelectron wave: collinear, non-collinear, single and multiple paths [101].

Using Dyson's equation $G_n = G_0 + G_0 V_n G_n$, is possible to rewrite the propagator

G in terms of G_0 as

$$\begin{aligned} G = G_0 + G_0 \sum_{n\neq a} t_n G_0 + G_0 \sum_{n\neq a} t_n G_0 \sum_{\substack{m\neq n\\ m\neq a}} t_m G_0 + G_0 \sum_{n\neq a} t_n G_0 \sum_{m\neq n} t_m G_0 \sum_{\substack{k\neq m\\ k\neq a}} t_k G_0 ... \\ = \left(1 - G_0 \sum_{b\neq a} t_b\right)^{-1} G_0 \end{aligned} \tag{3.22}$$

since in 3.22 is identified a geometrical series. Applying 3.22 in 3.17 leads to

$$\mu = \mu_0(1 + \chi_l) \tag{3.23}$$

where μ_0 is the background absorption correspondent to the isolated atom, l is the final state angular momentum, and χ is the trace of Γ matrix.

Through scattering paths determined by the *ab initio* calculations, the FTs of EXAFS oscillations are fitted in terms of variable parameters to be determined, as N_s, R_{as}, S_0^2 and σ_{as}^2. The quality of these fits can be determined by the *R-factor*, $\mathcal{R}$, which is a statistical measurement of the misfit relative to the data. $\mathcal{R}$ is calculated as

$$\mathcal{R} = \frac{\sum_{i=min}^{max}[Re(\chi_{mea}(r_i) - (\chi_{fit}(r_i))^2 + Im(\chi_{mea}(r_i) - (\chi_{fit}(r_i))^2]}{\sum_{i=min}^{max}[Re(\chi_{mea}(r_i))^2 + Im(\chi_{mea}(r_i))^2]} \tag{3.24}$$

where the summation is made over i measured points in the interval selected in the fit (min, max). The indexes *mea* and *fit* are for, respectively, measured and fitted data.

3.5.2 X-ray Absorption Near Edge Structure (XANES)

The energy position of an absorption edge is defined as the inflection point at that region. This position provides information about the oxidation state of the absorber (atoms with higher oxidation state have their nucleus less-shielded, therefore carry a higher effective charge, so core electrons have higher binding energies). Also the shape of the edge characterizes the chemical environment and ligand geometry, then it can be used as a fingerprint of a particular chemical species.

Several structures are found near the absorption edge describing electron transitions. The transition in the absorption edge is explained by the electric dipole transition rules, Δl = +-1, Δm = 0,±1, Δs = 0, and differ by the nature of their initial and final states. In some cases, it is possible to find a pre-edge region which cannot be explained by the dipole selection rules and are described by the quadrupole selection rules. In the edge region, electrons in initial bound states may transit into unfilled bound states, while in the *post-edge* region the transitions are to continuum states of large kinetic energy. A quadrupole transition probability is much smaller than a dipole one, but these transitions are observed for example in the *pre-edge* region of some transition metal complexes.

The *pre-edge* structures are useful for the determination of the absorber local geometry since the crystalline field features (as molecular bond lengths) affects strongly the orbital symmetry, creating hybrid states. Group theory offers a systematic study of geometric symmetries, and can be used to identify the hybrid final states. The crystalline structure is represented by a point group, describing the system's symmetries and properties. The basis sets described by a given irredutible representation of a point group are related to the orbital symmetries according to the Hamiltonian's symmetries. So, a irredutible representation of a point group that presents basis set functions of two different orbitals indicates the hybridization of these orbitals.

The most common methods to analyze the XANES region are the Linear Combination Analysis (LCA) and the Principal Component Analysis (PCA). The LCA method exploits the fact that the XANES shape is characteristic for a given absorber environment, and uses a theoretical linear combination of normalized reference spectra μ_{th} to fit the experimental spectrum μ_{exp}

$$\mu_{exp} = \sum_j \alpha_j \mu_{th} \tag{3.25}$$

with the correspondent α_j fractions of absorbers in the jth chemical state. A least-squares algorithm is also used to refine the sum of the reference spectra to the experimental spectrum. Given the simplicity of the method, the quality of the fit is dependent on the measurement quality of the spectra used in the fit. The PCA method is a more sophisticated technique, in which a set of contributions (principal components) are estimated and automatically selected from a series of reference spectra to reproduce the experimental data. Each selected contribution is associated to a vector and the measured spectrum is decomposed in a linear combination of these vectors using purely statistical considerations. Since these methods, *a priori*, uses none assumptions (as number or type of components) the choice of a plausible set ensemble of reference components is crucial to a meaningful analysis.

The spectral features around the absorption edge can be interpreted in terms of transitions to localized states or to the continuum. In this interpretation, the transitions to localized states can also be described by lorentzian peaks, while the summation of the transitions to the continuum describes a background in the absorption coefficient that can be modelled by an arctangent function. The lorentzian profile corresponds to a FT of a state that is exponentially decaying over its lifetime. The arctangent is a smooth representation of the step-function-like behavior from the density of states, related to the transitions as the lorentzian's integral.

4 ELUCIDATING CATALYTIC EVENTS BY ASSOCIATION TO CATALYST'S STRUCTURAL AND ELECTRONIC PROPERTIES

This chapter is dedicated to describe in details the experimental setups, procedures related to the samples preparation and analysis performed for the characterization of $Cu_xNi_{1\text{-}x}/CeO_2$ ($0<x<1$) NPs. In order to determine the synthesized NPs atomic arrangement, the samples were characterized as prepared by EDS, TEM and conventional XPS techniques. Afterwards, the samples were exposed to a reduction treatment followed by the RWGS reaction, while characterized *in situ* by NAP-XPS, XAS and time-resolved XAS techniques.

4.1 Samples synthesis

$Cu_xNi_{1\text{-}x}$ NPs were synthesized in collaboration with Prof. Jairton Dupont, at the Laboratory of Molecular Catalysis (LAMOCA) of Institute of Chemistry at UFRGS. In accordance to the procedure described in [60], solutions of $CuCl_2{\cdot}2H_2O$ and $NiCl_2{\cdot}6H_2O$ were dissolved in the ionic liquid $BMI{\cdot}BF_4$ to synthesize four different samples containing selected concentrations (x) of $Cu_xNi_{1\text{-}x}$ bimetallic NPs. In order to obtain supported samples, the synthesized NPs were supported on commercial CeO_2.

EDS measurements were performed intending to identify possible species remaining from the synthesis process, to determine the metal/support weight concentration for the supported NPs, and to determine the Cu and Ni concentrations in the bimetallic samples.

4.2 *Ex situ* characterization of the as prepared samples

4.2.1 EDS measurements

The EDS measurements were carried out on the scanning electron microscope *Zeiss EVO MA10* at the UFRGS's Microscopy and Microanalysis Center (CMM). To perform the measurements, a layer of the sample's powder was spread out over a carbon tape supported on a metallic stub. Thereafter, the samples were exposed to a carbon deposition through an evaporating method to eliminate charging effects during the measurements. The microscope, operating at 15 kV, scanned several different regions of each sample to obtain mean values of Cu and Ni concentrations in non-supported bimetallic NPs. The Cu/CeO_2 sample was also measured to determine the atomic fraction of metal in the CeO_2 of the samples. Typical results are presented in table 4.1.

Table 4.1 – EDS spectra of non-supported $Cu_xNi_{1\text{-}x}$ and Cu/CeO_2 NPs with the associated atomic concentrations obtained by the spectra analysis.

EDS Spectrum	Atomic concentration[%]
a) 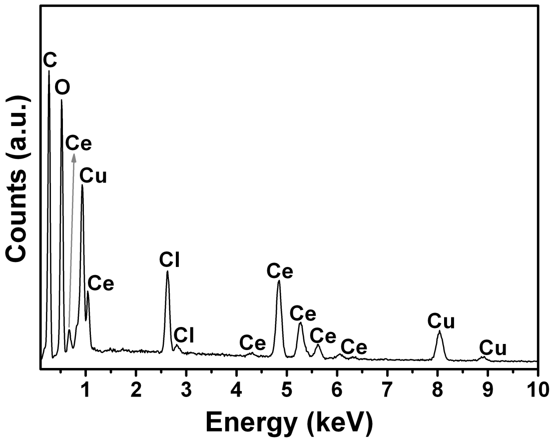	$Cu = 45 \pm 1$ $Ce = 55 \pm 1$

b) 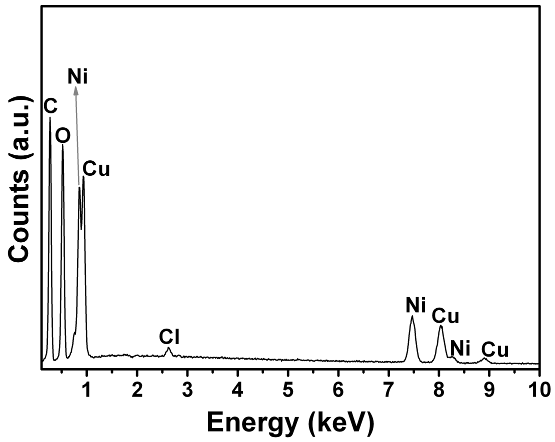	Cu = 60 ± 3 Ni = 40 ± 3
c) 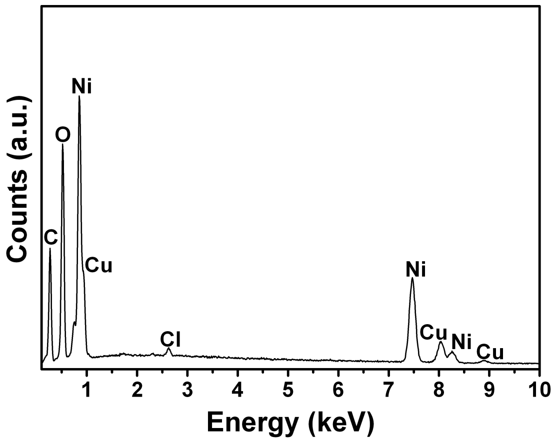	Cu = 35 ± 3 Ni = 65 ± 3
d) 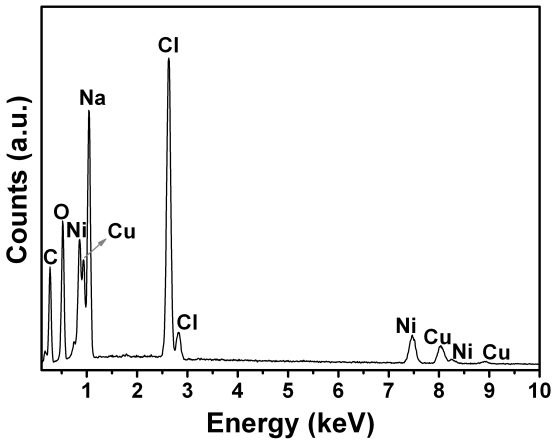	Cu = 25 ± 4 Ni = 75 ± 2

In table 4.1, the carbon detection observed by the peak next to 0.25 keV in the spectra is due to the carbon tape and carbon deposition used in the samples preparation. In the $Cu_{0.25}Ni_{0.75}$ NPs spectrum, a Na contamination is accused by the peak around 1 keV, showing the presence of remaining from the solutions used in the synthesis process of the samples. Cl peaks were observed, being also expected due to unreacted starting material remaining during the synthesis procedure ($CuCl_2 \cdot 2H_2O$ and $NiCl_2 \cdot 6H_2O$). The O atoms may come from several sources like synthesis procedure, air exposition and sample holder. Analyzing the Cu/CeO_2 NPs spectrum, the Cu/Ce atomic ratio converted to mass concentration shows that approximately 20% of the sample's mass corresponds to Cu, as expected from previous procedures [60].

Since each sample presents a different concentration of Cu, samples were labeled as $Cu_xNi_{1\text{-}x}$ NPs, for non-supported cases, and $Cu_xNi_{1\text{-}x}/CeO_2$ NPs, for the supported ones, where the subscribed x index may assume the values 0.25, 0.35, 0.60, or 1, indicating the respective Cu concentration of a given sample.

The next step in the characterization of these NPs is the size and shape determination. TEM measurements were performed for this purpose.

4.2.2 TEM measurements

The TEM images were obtained using the *JEOL JEM 1200 EXll* microscope, also at the CMM (UFRGS). To perform the measurements, $Cu_xNi_{1\text{-}x}/CeO_2$ (x = 0.25, 0.35, 0.60, 1) NPs were dispersed in deionized water using ultrasound, and a drop of each solution was placed over a copper grid coated by a carbon film. Using a 80 kV operational voltage, the microscope imaged several regions of the Cu grid in order to provide a good statistics on the determination of the NPs mean diameter.

The *ImageJ* software was used to obtain the histogram of size distribution in the images collected by the microscope. The first step in this process was the enhancement of images contrast in order to achieve a better definition in the NPs borders. A threshold filter was then applied, eliminating the background structures and highlighting the NPs. Each evidenced mark, representing a NP, had its area calculated (in the unit set in the image's scale) and the diameter is obtained considering a circle approximation for this area.

The mean diameter value was obtained averaging the values obtained in the *ImageJ*'s analysis over about 2500 NPs for each sample. Typical TEM images of the samples are shown in Figure 4.2.1 aside of the respective size distributions obtained. It was possible to observe shape differences comparing monometallic and bimetallic samples: pure Cu NPs presents irregular shapes, while bimetallic NPs tend to appear in more spherical shapes.

a) Cu/CeO_2 NPs

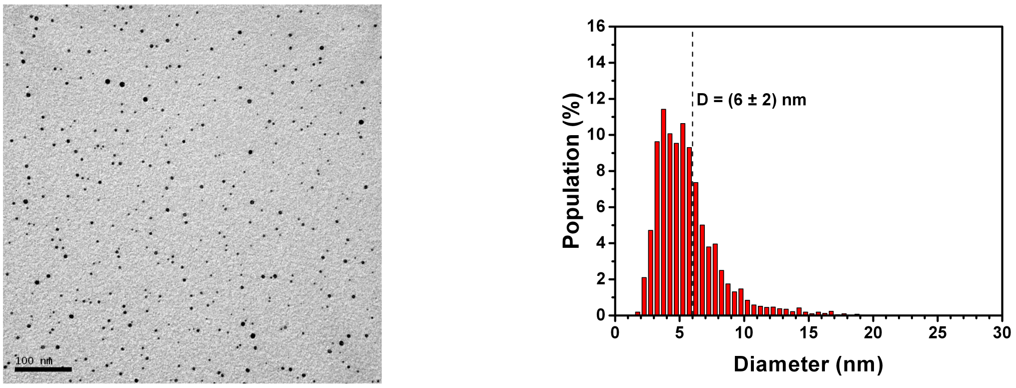

b) $Cu_{0.60}Ni_{0.40}/CeO_2$ NPs

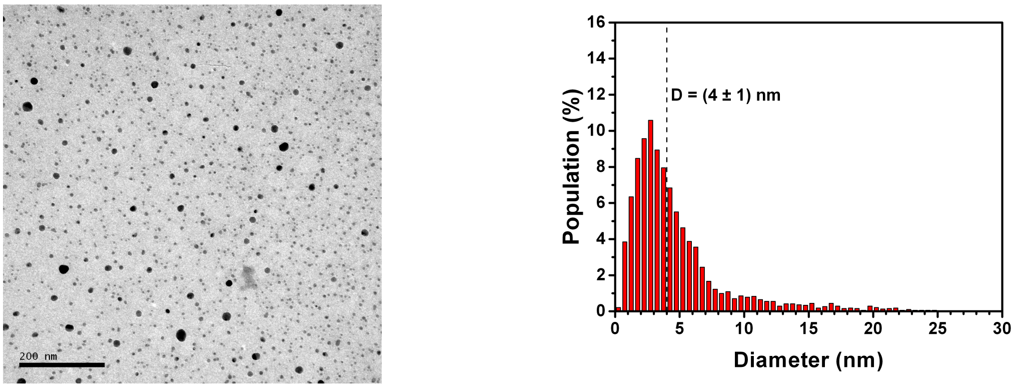

c) $Cu_{0.35}Ni_{0.65}/CeO_2$ NPs

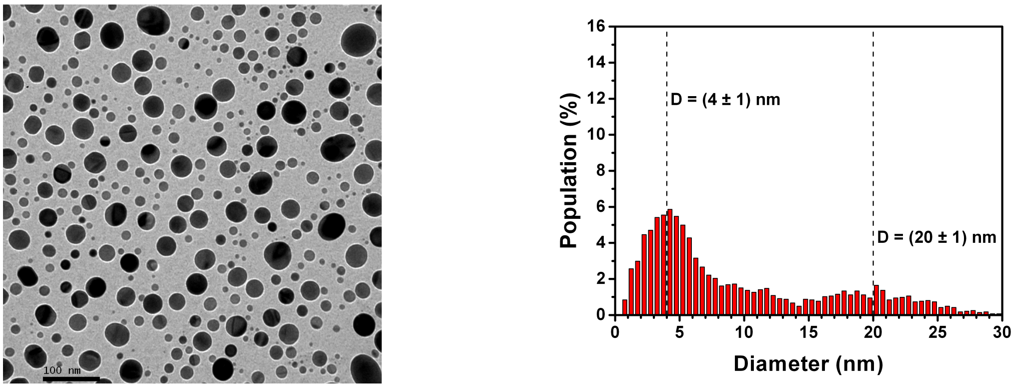

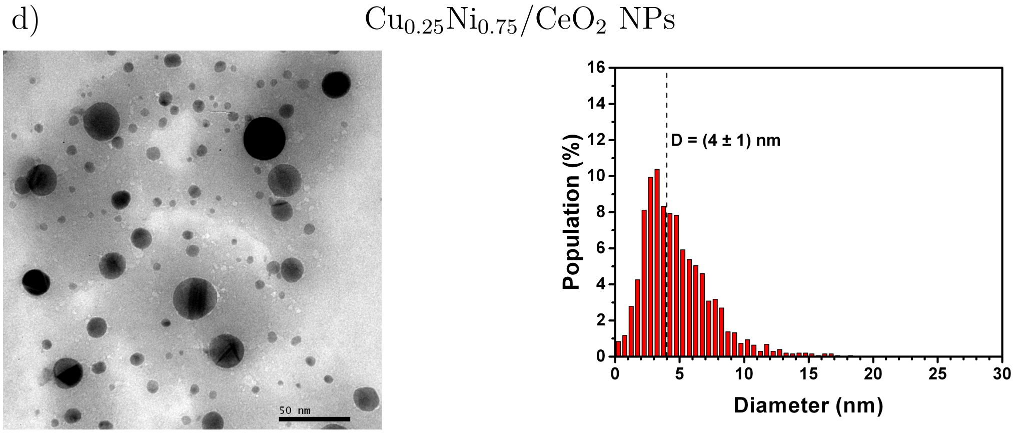

Figure 4.2.1 – TEM images of a) Cu/CeO_2, b) $Cu_{0.60}Ni_{0.40}/CeO_2$, c) $Cu_{0.35}Ni_{0.65}/CeO_2$, and d) $Cu_{0.25}Ni_{0.75}/CeO_2$ NPs, with the respective histogram of size distribution. The mean diameter value of major populations are indicated by the dashed lines.

During the TEM measurements it was possible to identify regions in the grid where Cu-Ni NPs were non-supported and regions where they were well supported on CeO_2. This desorption phenomenon may be related to the dispersion procedure promoted by the ultrasound treatment in the sample preparation. Desorption enhanced processes involving ultrasound treatments are described in the literature [102, 103].

The histogram of size distribution presents a lognormal-type distribution. In the $Cu_{0.35}Ni_{0.65}/CeO_2$ NPs case, the samples presented 2 distinct NPs population with different mean diameters. The NPs diameters of the population related to smaller sizes proved to be independent of the Cu/Ni ratio since a common mean value around 4 nm was observed to all the cases.

In order to study the electronic properties, and to finish the structural characterization of the as prepared NPs, the samples were studied using the XPS technique.

4.2.3 Conventional XPS measurements

The conventional XPS measurements were carried out on the *Thermo Scientific K-Alpha* X-ray photoelectron spectrometer at the LNNano-CNPEM. Using an Al Kα ($h\nu$=1486.7 eV) X-ray source operating at 12 kV, the non-supported $Cu_xNi_{1\text{-}x}$ (x=0.25, 0.35, 0.60, 1.00) NPs were analyzed during the measurements. The NPs were measured non-supported in order to avoid charging effects during the XPS measurements, which would make the analysis of the spectra more complicated. The measurements were performed in the survey, Cu 2p, Cu 3p, Ni 2p, Ni 3p, O 1s and C 1s regions. For these measurements, a thin layer of each sample's powder was dispersed on a carbon tape, placed in the sample holder, and exposed to ultra high vacuum. The ejected photoelectrons were collected in the exit angle of 45° by a double focusing hemispherical analyzer operating in the CAE mode. To perform low and high resolution measurements, the pass energies used were 200 eV and 50 eV, while the energy steps were 1 eV and 0.1 eV, respectively, and the dwell time was 0.1 s.

To analyze the measured spectra, the software *XPSPEAK41* was used. The analysis process began with the background contribution removal by fitting a *Shirley-type* function [104]. The Au 4f region was measured (from a Au standard sample) and analyzed in order to determine the *Voigt profile* used to fit the XPS peaks. This profile combines a Lorentzian function, which accounts for the intrinsic life time broadening of the core-level hole state and the X-ray line shape from the X-ray source, with a Gaussian function, which describes the response function of the analyzer. Therefore, a symmetric Gaussian-Lorentzian combination was used to fit the Au 4f peaks, resulting in a 55% Lorentzian - 45% Gaussian profile. Then, the energy calibration of the samples was accomplished considering the adventitious carbon in the C 1s region at 285.0 eV, according to [91]. In order to perform a consistent fit that allows the results comparison between the samples, a ΔE_b range value was fixed for each measured region. To interpret the data in this selected range, binding energy position constrains were set between the different chemical components. The FWHM (full width at half maximum) of a given component was constrained to the same value for all the samples.

A quantitative analysis was performed to characterize the atomic structure of the as prepared samples. In order to probe different depths of the NPs, photoelectrons coming from the Cu and Ni atoms with different kinetic energies were studied. The kinetic energy associated to the photoelectrons ejected from the Cu (and Ni) 2p and 3p electronic levels were calculated using the photoelectric effect relation (Eq. 3.2). Then, these kinetic energy values were used in the *IMFP-TPP2M* code [105] to calculate the electron inelastic mean free path. The values determined for the photoelectrons coming from the Cu and Ni electronic levels were averaged, resulting in a mean depth probed by the photoelectrons from the 2p (3p) electronic levels of $\lambda \approx 11$ Å ($\lambda \approx 20$ Å). In order to compare the Cu/Ni atomic ratio in these depths, the intensity of the Cu and Ni $2p_{3/2}$ and 3p regions were normalized by the photoionization differential cross section values, obtained by an interpolation of data from theoretical [106] and experimental [107] databases. The photon flux and analyzer efficiency of detection were considered the same for all the cases and, then, are not considered in the calculus. Using the Cu/Ni normalized atomic fraction determined for different probed depths, the NPs atomic structures were determined.

4.2.3.1 Survey region

In order to identify possible contaminations, a survey scan was performed in each sample. The spectra are very similar among samples, presenting Cl peaks coming from the synthesis process. Furthermore, Na peaks were detected in $Cu_{0.25}Ni_{0.75}$ NPs spectra, also due to remnants from the synthesis process. Both results are in accordance to the EDS results found. Figure 4.2.2 presents the survey spectrum in the $Cu_{0.60}Ni_{0.40}/CeO_2$ NPs, where the components are identified.

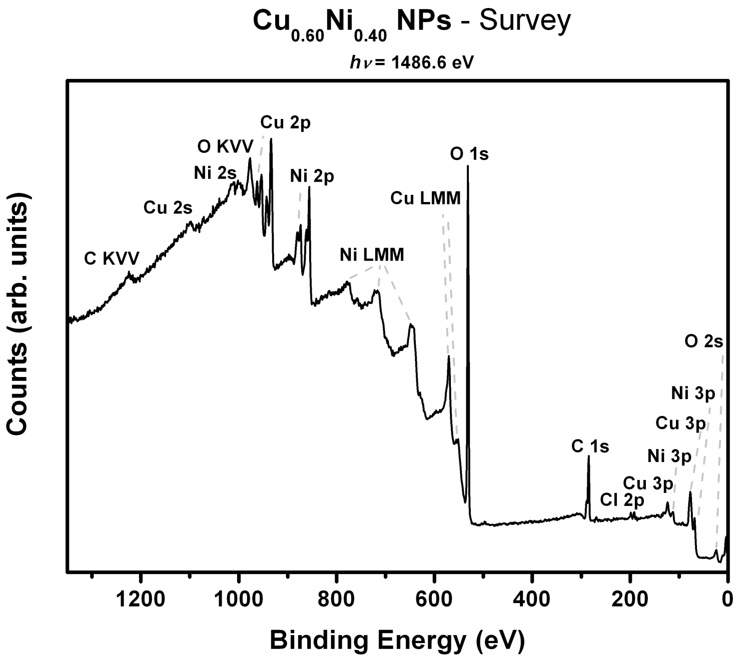

Figure 4.2.2 – XPS survey spectrum of the as prepared $Cu_{0.60}Ni_{0.40}$ NPs measured using an Al Kα X-ray source. Copper, nickel, oxygen and carbon Auger transitions are observed.

4.2.3.2 Cu and Ni 2p regions analysis

Figure 4.2.3 shows the XPS spectra at the Cu $2p_{3/2}$ and Ni $2p_{3/2}$ regions for the Cu_xNi_{1-x} (x = 0.25, 0.35, 0.60, 1.00) NPs. It is possible to observe an increase on the Cu $2p_{3/2}$ intensity with the increase of the Cu concentration in the NPs. Analogous trend is observed for the Ni $2p_{3/2}$ region. Moreover, it is clear the presence of more than one chemical component, which can be determined by the analysis of the region.

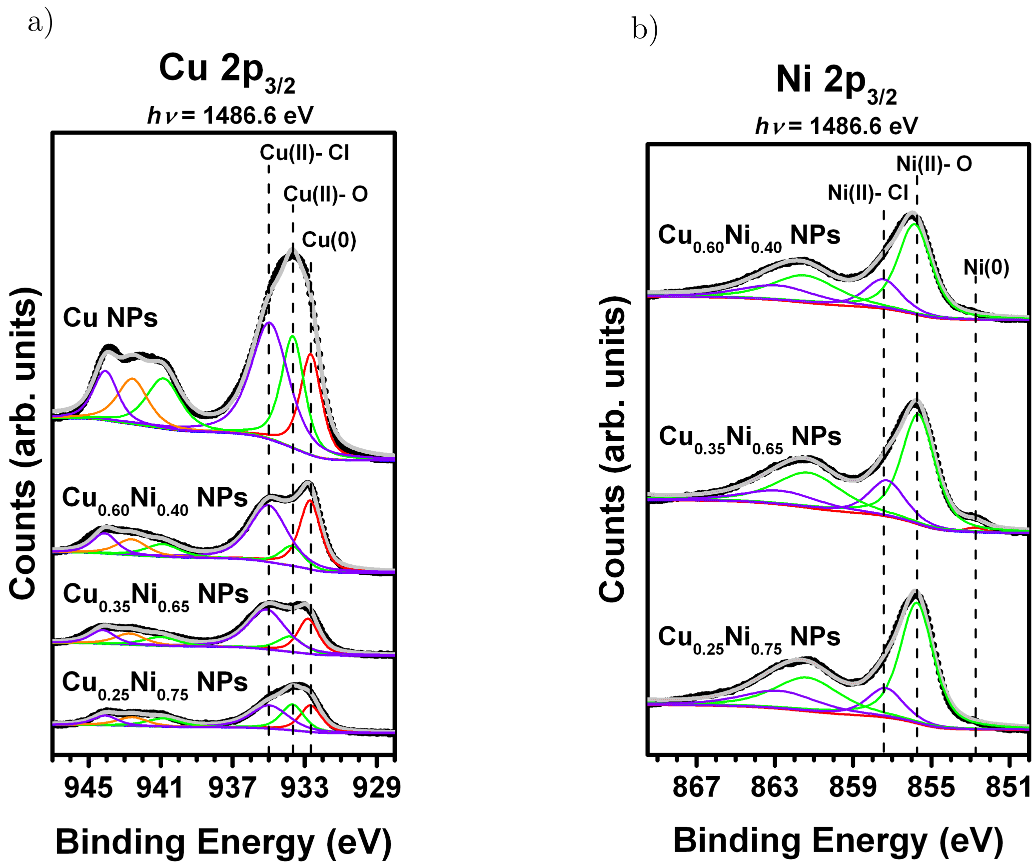

Figure 4.2.3 – a) Cu 2p$_{3/2}$ and b) Ni 2p$_{3/2}$ XPS spectra of the as prepared Cu$_x$Ni$_{1\text{-}x}$ (x=0.25, 0.35, 0.60, 1.00) NPs measured using an Al Kα X-ray source. The black points represent the experimental data, the dash blue line the Shirley background used, and the gray line the best fit result. The components used to fit the Cu region are presented as red, green, and purple dashed lines indicating Cu(0), Cu(II)-O, and Cu(II)-Cl components, respectively. The orange peak in the Cu 2p$_{3/2}$ region corresponds to a superposition of satellites from Cu(II)-O and Cu(II)-Cl. To fit the Ni region, red, green, and violet dashed lines are used to indicate the Ni(0), Ni(II)-O, and Ni(II)-Cl components, respectively.

The XPS peaks at the Cu 2p$_{3/2}$ region were fitted using a combination of main peaks and the respective shake-up satellites. In order to fit this region, the FWHM and the binding energy position of main peaks and the respective satellites were constrained to the values presented on tables 4.2 and 4.3. The binding energy position values present good accordance to the reported values in the literature [108, 109, 110, 111, 112, 113]. The analysis shows the presence of three components for the Cu 2p$_{3/2}$ region: a metallic component (Cu(0)) and two components related to oxidation states with NOX +2. These oxidation states were identified as due to Cu bonds to O (Cu(II)-O) and Cl (Cu(II)-Cl) atoms.

At the Ni2p$_{3/2}$ XPS region, a similar fitting process was performed. The values of FWHM and the binding energy positions constrained in the fitting procedure are also presented on table 4.3. Three components were identified on the Ni $2p_{3/2}$ region analysis: a metallic component (Ni(0)), a component related to Ni bonds to O (Ni(II)-O), and a component related to Ni bonds to Cl (Ni(II)-Cl) atoms.

Table 4.2 – Energy position and FWHM parameters used to fit the main peaks and correspondent satellites (sat.) associated to the chemical components observed at the Cu $2p_{3/2}$ region.

Chem. Component	Position [eV]	FWHM [eV]
Cu(0)	932.72	1.4
Cu(II)-O	Cu(0)+1.00	1.72
Cu(II)-O 1st sat.	Cu(0)+9.18	2.25
Cu(II)-O 2nd sat.	Cu(0)+10.90	2.01
Cu(II)-Cl	Cu(0)+2.30	2.48
Cu(II)-Cl 1st sat.	Cu(0)+12.20	2.01
Cu(II)-Cl 2nd sat.	Cu(0)+13.70	1.61

Table 4.3 – Energy position and FWHM parameters used to fit the main peaks and correspondent satellites (sat.) associated to the chemical components observed at the Ni $2p_{3/2}$ region.

Chem. Component	Position [eV]	FWHM [eV]
Ni(0)	852.85	1.20
Ni(II)-O	Ni(0)+2.90	2.02
Ni(II)-O sat.	Ni(0)+8.40	3.99
Ni(II)-Cl	Ni(0)+4.50	2.18
Ni(II)-Cl sat.	Ni(0)+9.90	4.57

The chemical components fractions found at the Cu $2p_{3/2}$ and Ni $2p_{3/2}$ regions on the as prepared NPs are presented in table 4.4. The analysis of the Ni $2p_{3/2}$ region shows that the Ni chemical states found in the NPs surface are essentially related to oxidized states. Only the $Cu_{0.35}Ni_{0.65}$ NPs presented a metallic component with a very small intensity. High intensity chemical components associated to a bond with Cl atoms are detected for the Cu 2p region in all the samples. On the other hand, the most important chemical component for the Ni $2p_{3/2}$ region was that associated to Ni-O bonds.

Table 4.4 – Components percentage used to fit the Cu $2p_{3/2}$ and Ni $2p_{3/2}$ XPS regions of the as prepared $Cu_xNi_{1\text{-}x}$ (x=0.25, 0.35, 0.60, 1.00) NPs.

Sample	%Cu(0)	%Cu(II)-O	%Cu(II)-Cl	%Ni(0)	%Ni(II)-O	%Ni(II)-Cl
Cu NPs	16.0	37.2	46.8	-	-	-
$Cu_{0.60}Ni_{0.40}$ NPs	26.8	20.8	52.4	0.0	68.8	31.2
$Cu_{0.35}Ni_{0.65}$ NPs	20.1	24.2	55.7	1.1	71.1	27.8
$Cu_{0.25}Ni_{0.75}$ NPs	20.0	36.0	44.0	0.0	72.2	27.8

4.2.3.3 Cu and Ni 3p regions analysis

Figure 4.2.4 shows the Cu 3p and Ni 3p XPS spectra for the as prepared $Cu_xNi_{1\text{-}x}$ (x=0.25, 0.35, 0.60) NPs. Aiming to study the atomic structure of the as prepared bimetallic NPs, the Cu and Ni 3p regions were fitted to determine the respective intensities. Due to the small photoionization cross section, the spectra of these regions present low intensity. Since the chemical components analysis using these regions is scarcely reported in the literature, the regions were fitted without constraints.

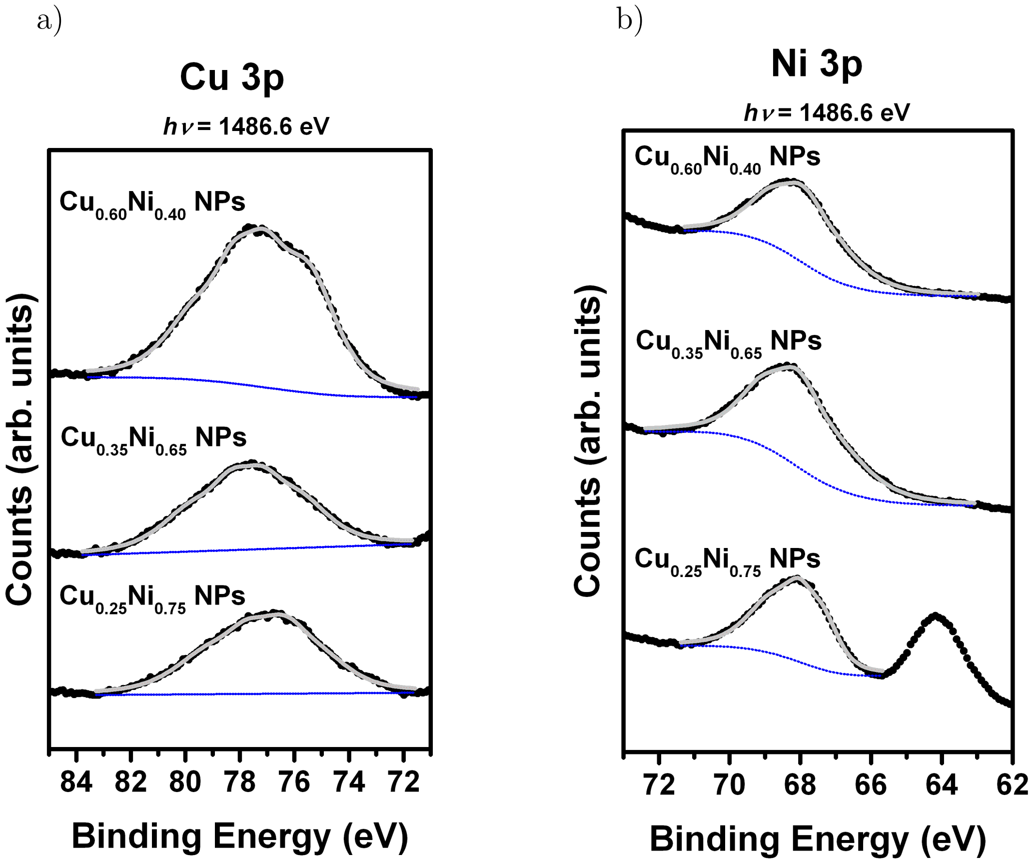

Figure 4.2.4 – a) Cu 3p and b) Ni 3p XPS spectra of the as prepared $Cu_xNi_{1\text{-}x}$ (x=0.25, 0.35, 0.60) NPs measured using an Al Kα X-ray source. The black points represent the experimental data, the dash blue line the Shirley background used, and the gray line the best fit result.

The peak observed around 64 eV in the Ni 3p XPS region of the $Cu_{0.25}Ni_{0.75}$ NPs was identified as coming from the Na 2s region. This peak is present due to the Na contamination previously related.

Using the areas correspondent to the fitted Cu $2p_{3/2}$, Ni $2p_{3/2}$, Cu 3p and Ni 3p regions, it was possible to determine the atomic structures of the as prepared samples. Table 4.5 relates the Cu/Ni normalized ratio found in samples analysis with the depths probed by the photoelectrons ejected from the 2p and 3p electronic levels.

Table 4.5 – Cu/Ni ratio normalized by the differential cross section at different depths in the as prepared bimetallic $Cu_xNi_{1\text{-}x}$ (x = 0.25, 0.35, 0.60) NPs. The depths of 11 Å and 20 Å corresponds, respectively, to the inelastic mean free path of photoelectrons ejected from the 2p and 3p electronic levels of Cu and Ni.

Sample	Cu/Ni normalized ratio	
	(λ = 11 Å)	(λ = 20 Å)
$Cu_{0.60}Ni_{0.40}$ NPs	0.99	2.73
$Cu_{0.35}Ni_{0.65}$ NPs	0.54	1.12
$Cu_{0.25}Ni_{0.75}$ NPs	0.41	1.31

Table 4.5 shows, for all the samples, a decrease on the Cu/Ni normalized ratio for regions closer to the surface of the NPs in comparison to more in depths regions. Since the ratio was normalized by the differential cross section, it is directly related to a higher Ni atomic population at the surface of the NPs than the inner region. On the other hand, the analysis associated to the large probed depth (inner region) shows a higher Cu atomic population in comparison to the Ni atomic population. It shows a Ni enrichment at the surface region for all the bimetallic samples synthesized. Moreover, it is possible to observe that the surface atomic population matches the Cu (Ni) concentration of the NPs obtained in the EDS analysis, *i.e.* the Cu-richer NPs also present the Cu-richer surfaces.

Ruban *et al.* [114] performed theoretical calculation aiming to determine the surface segregation energies of several different host-solute metal combination. The authors showed that the Cu-Ni system presents moderate segregation of Cu atoms to the surface. This result is in contradiction to those found in Table 4.5. The same tendency is observed theoretically in [115]. However, it is important to stress out that the theoretical calculations were performed for surface clean systems that does not correspond to the system used in the present work. As well known from the literature [116], NPs synthesized by using ionic liquids present important interaction at the surface region with the anion of the ionic liquid, then certainly changing the energy configuration for this system. A more detailed theoretical calculation is needed for comparison purposes. Concerning experimental studies, in the literature is possible to found Cu-Ni NPs synthesized with a Cu-rich surface [55], Ni rich surface [117] or both cases [118]. It shows the strong dependence of the surface atomic population on the synthesis method employed. For the method used in this work, by using ionic liquids, it observed a Ni enrichment at the surface of the bimetallic NPs.

Examining the NPs atomic structures, the observed Cu (Ni) concentration gradient is different from sample to sample: comparing the Cu/Ni normalized ratio on the NPs surface and inner region, it is observed an increase of this ratio in the inner region of 220% for $Cu_{0.25}Ni_{0.75}/CeO_2$ NPs, 107% for $Cu_{0.35}Ni_{0.65}/CeO_2$ NPs, and 176% for $Cu_{0.60}Ni_{0.40}/CeO_2$ NPs, in comparison to the surface region.

4.3 *In situ* characterization of the samples

After the characterization of the as prepared NPs, *in situ* X-ray based techniques were applied to probe the electronic and structural properties of the catalysts during the H_2 reduction treatment and the Reverse Water-Gas Shift (RWGS) reaction at 500 °C. The H_2 reduction is typically employed in catalysis aiming to bring the catalyst to the active form before the catalytic reaction (RWGS). During the reaction, the H_2O and CO formation was monitored by Mass Spectrometry measurements.

4.3.1 Time-resolved Mass Spectrometry measurements

In order to study the NPs reactivity towards $CO_2 \rightarrow CO$ conversion, time-resolved Mass Spectrometry measurements were conducted during *in situ* time-resolved XAS measurements performed on the supported $Cu_xNi_{1\text{-}x}/CeO_2$ (x=0.25, 0.35, 0.60, 1.00) NPs at the DXAS beamline [87] of the Brazilian Synchrotron Light Laboratory (LNLS). Due to the well known importance of the support in the catalytic reaction [119], only the supported NPs were studied.

Inside a tubular furnace, a sample's pellet produced by compacting a mix of 7 mg of NPs powder and 45 mg of BN was exposed to a 100ml/min 5% H_2 + 95% He flux and heated from room temperature to 500 °C with a 10 °C/min heating rate. At 500 °C, the samples were left in the reduction atmosphere during 30 min. After this reduction treatment, it was inserted a flux of 25ml/min 20% CO_2 + 80% He for 30 minutes, then starting the RWGS reaction. Using a *BROOKS* mass controller to control the gas fluxes, a *Pfeiffer Vacuum OminiStar* MS coupled to the tubular furnace (where the sample holder was placed) analyzed the gases after reacting with the sample. An initial Mass Spectrometry measurement of the H_2+CO_2 flux was performed without samples at the tubular furnace, aiming to determine the intrinsic $CO_2 \rightarrow CO + O$ conversion due to CO_2 dissociation by electron impact ionization at the MS detection.

The time-resolved Mass Spectrometry signal for the H_2O (18 g/mol) and CO (28 g/mol) productions during the RWGS reaction for the supported NPs can be observed in Figure 4.3.1. The sudden increase in the CO signal, at 0 s, indicates the beginning of the samples exposure to the H_2+CO_2 atmosphere. In order to discount the signal fluctuations coming from the flux variations on the inserted gas, the measured H_2O and CO data was normalized by the He detected signal. The earlier H_2O signal existing before the beginning of the reaction is related to residual molecules arriving at the spectrometer.

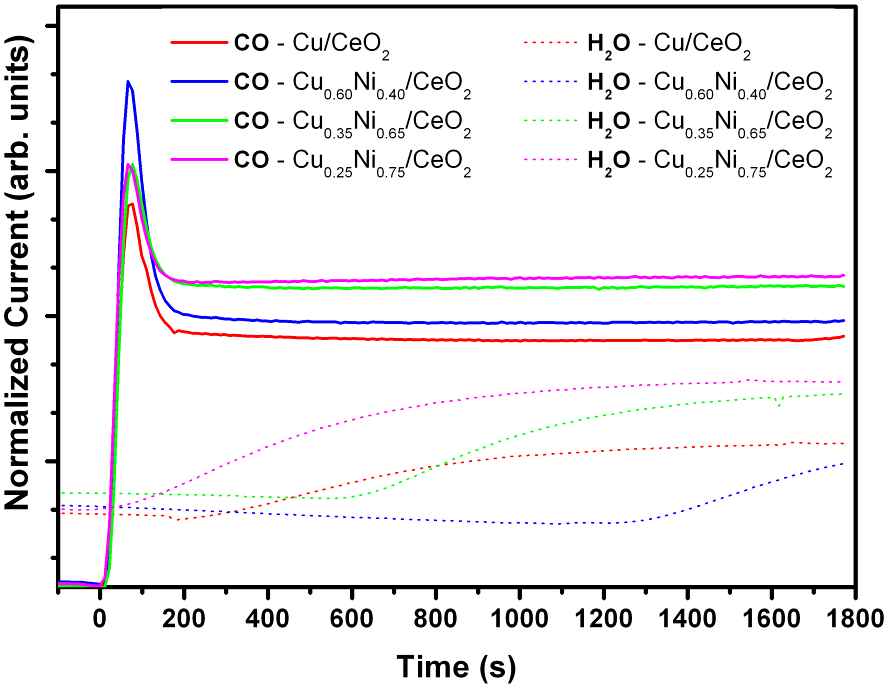

Figure 4.3.1 – CO (28 g/mol) and H_2O (18 g/mol) formation measured by the Mass Spectrometry during the exposition of the $Cu_xNi_{1\text{-}x}/CeO_2$ (x=0.25, 0.35, 0.60, 1.00) NPs to the H_2+CO_2 flux at 500 °C. The star index (*) indicates that the current intensities are presented normalized by the He signal detected during the measurements. Data is presented from the insertion of H_2+CO_2 flux (Time = 0 s) to the end of the reaction (Time = 1800 s).

It is noticed, in Figure 4.3.1, that H_2O and CO signals of a given sample does not follow the same trend over the RWGS reaction. Furthermore, is observed that the H_2O signal starts to increase after the reaction beginning and at different times for each sample. Moreover, it is observed that after the first 100 seconds of reaction there is a decrease on the CO normalized intensity and the catalysts presented a partial deactivation process that leaded to a stable reactivity on the gaseous atmosphere.

In a "reactivity ranking", the Cu/CeO_2 NPs present the lowest CO signal and a low H_2O signal throughout the reaction, evidencing the Ni collaboration on the enhancement of the samples reactivity in the RWGS reaction. By comparing the bimetallic samples behavior, the $Cu_{0.60}Ni_{0.40}/CeO_2$ NPs presents the highest reactivity in the beginning of the reaction, followed by the $Cu_{0.35}Ni_{0.65}/CeO_2$ NPs and

$Cu_{0.25}Ni_{0.75}/CeO_2$ NPs presenting about the same CO production. However, the $Cu_{0.60}Ni_{0.40}/CeO_2$ NPs presents the highest deactivation among the samples, becoming the worst bimetallic sample to the CO production at the end of the H_2+CO_2 treatment.

In order to perform a quantitative comparison among the samples reactivity, the detected signals associated to H_2O and CO were integrated during the H_2+CO_2 atmosphere exposition and normalized by the integration value associated to the total signal coming from H_2+CO_2 gases. The integrated values of the H_2O and CO signals in the measurements is presented in Figure 4.3.2.

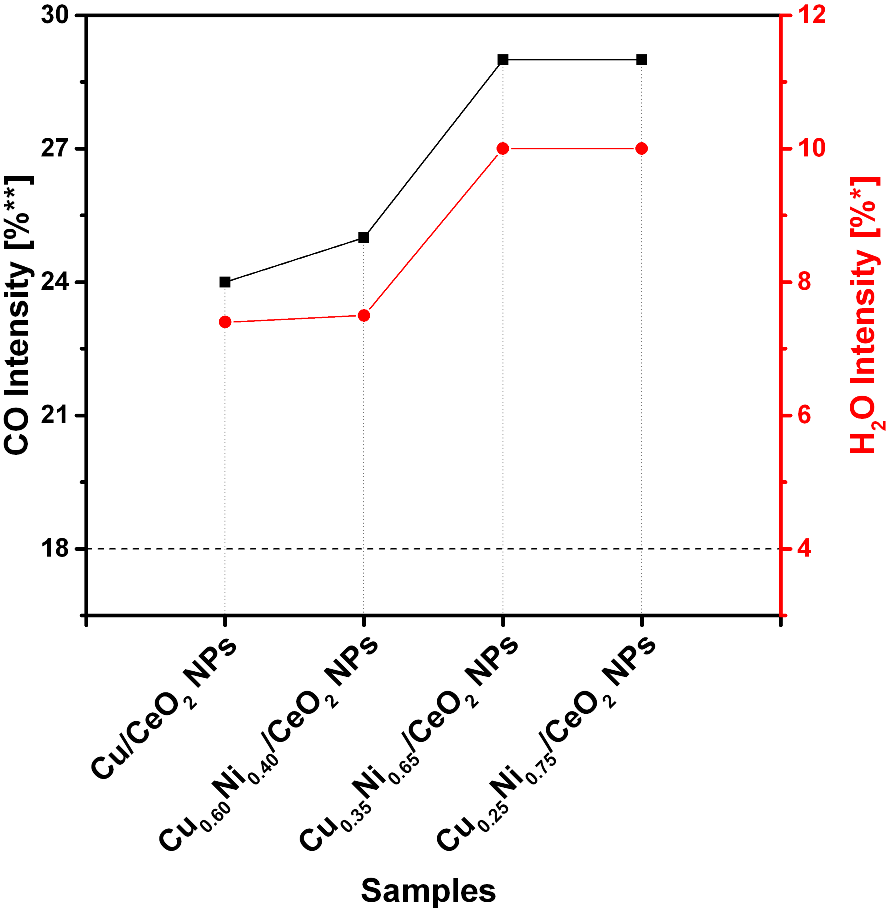

Figure 4.3.2 – CO and H_2O formation for the Cu_xNi_{1-x}/CeO_2 (x=0.25, 0.35, 0.60, 1.00) NPs, measured during 30 minutes in the H_2+CO_2 atmosphere. The star index (*) indicates that the intensity values associated to H_2O formation are presented normalized by the total H_2+CO_2 signal detected, integrated throughout the measurements. The double star index (**) indicates that the intensity values associated to CO formation are presented normalized only by the detected CO_2 signal, integrated during the measurements. The dashed black line correspond to the value measured from the intrinsic CO formation in the CO_2 detection without the samples, namely 18%.

Figure 4.3.2 shows that the H_2O and CO total production, then the CO_2 dissociation, follows a single trend, in which the reactivity towards the RWGS reaction is partially enhanced by the increase of the Ni amount in the NPs. The catalytic property of the samples is ensured by the improvement in CO_2 dissociation, since the intensities associated to the CO signal are higher than 18%, value detected for the CO formation without samples in the reaction chamber.

Aiming to elucidate the phenomena observed in the CO_2 dissociation reaction (water delayed detection and differences between samples in the reactivity toward CO_2 dissociation to CO), *in situ* X-ray based techniques were applied to probe the atomic phenomena occurring during the catalytic reaction.

4.3.2 NAP-XPS measurements

The NAP-XPS measurements were carried out at the CIRCE beamline at ALBA [95] in Barcelona, Spain. Using a plane grating monochromator, measurements in two different incident photon energies were realized: $h\nu$=1250 eV and $h\nu$=2000 eV. An electron hemispherical analyzer (*SPECS GmbH PHOIBOS 150 NAP*) was used to probe the Survey, Cu 2p, Ni 2p, Ce 3d, O 1s, and C 1s regions operating in the CAE mode. For high resolution measurements, the pass energy was 10 eV, the energy step was 0.1 eV and dwell time of 0.1 s, while in the Survey region, the pass energy was 20 eV, the energy step was 1 eV with dwell time of 0.1 s. The ejected photoelectrons were collected with an exit angle equal to the *magic angle* ($\approx$ 54.7°).

Pellets made of 10 mg Cu_xNi_{1-x}/CeO_2 (x=0.25, 0.35, 0.60, 1.00) NPs and non-supported Cu NPs powder were heated to 500 °C under a 5.0 mbar H_2 atmosphere. At 500 °C, the H_2 pressure was decreased to 1.0 mbar and the sample was left exposed to this atmosphere during 50 min. After that, 1.0 mbar CO_2 was inserted in the main chamber in order to accomplish the RWGS reaction. The sample was exposed to this H_2+CO_2 atmosphere during 30 min. The NAP-XPS measurements, with $h\nu$=1250 eV and $h\nu$=2000 eV were performed at the end of each gas treatment. After this, the gas was pumped out and the sample was cooled to room temperature under vacuum.

The Cu $2p_{3/2}$, Ni $2p_{3/2}$, O 1s and C 1s NAP-XPS data analysis was similar to that performed in conventional measurements data. A Shirley-type function [104] was used to fit the background contribution in all the analyzed regions. A gold sheet was measured and the analysis of its Au 4f region determined a 46% Lorentzian and 54% Gaussian contributions to the *Voigt profile*. Then, the energy calibration was fulfilled by comparing the adventitious carbon peak at C 1s to the reference value [91], 285.0 eV. The constrains in the components binding energy positions, and area ratios between main peaks and satellites used in the fits are presented on Tables tables 4.6, 4.8, 4.11 to 4.14 and 4.17. For each incident photon energy, the FWHM value of a given component was constrained to a given value for all the samples and atmospheric treatments. The exception to this procedure was the analysis in the Ce 3d region. In this case is not possible to associate the energy binding position of a given peak to a given chemical component. The complex Ce 3d region analysis allows the determination of the Ce(III) fraction existing at the surface of the sample. Details about the fitting procedure in this region are given in Section 4.3.2.3.

In order to study the atomic structure of the NPs during the reaction with the gaseous phase, an analogous data treatment to the conventional XPS data was applied. In this case, however, the probed depth was changed using different incident photon energies and probing always the same regions (Cu $2p_{3/2}$, Ni $2p_{3/2}$ and Ce 3d). It gives an inelastic mean free path around 8 Å ($h\nu = 1250$ eV) and 17 Å ($h\nu = 2000$ eV) for the photoelectrons coming from the Cu 2p, Ni 2p and Ce 3d regions (also determined using the *IMFP-TPP2M* code [105]). The total area from fitted regions were normalized by the correspondent photoionization differential cross sections, obtained by the same method used to fit the XPS measurements of the as prepared non-supported NPs.

4.3.2.1 Cu 2p region analysis

Figure 4.3.3 shows a comparison between the Cu $2p_{3/2}$ NAP-XPS spectra in the H_2 and H_2+CO_2 atmospheres for each sample. All the samples presented a Cu(0) metallic component at 933.1 eV. In the bimetallic samples appears also a small component associated to Cu(II) oxidation state due to Cu-O bonds at 933.9 eV. It occurs even during the reduction treatment employed. It is interesting to note that when increasing the photon energy, then increasing the probed depth, there is an increase of the Cu(II) component which is not expected since the oxidation procedure starts at the surface of the NPs. The study about the atomic configuration of the catalysts can explain this unexpected feature. The samples exposure to the H_2+CO_2 atmosphere did not present a significant oxidation effect for the Cu atoms. The constrained parameters used to fit the chemical components are presented in Table 4.6.

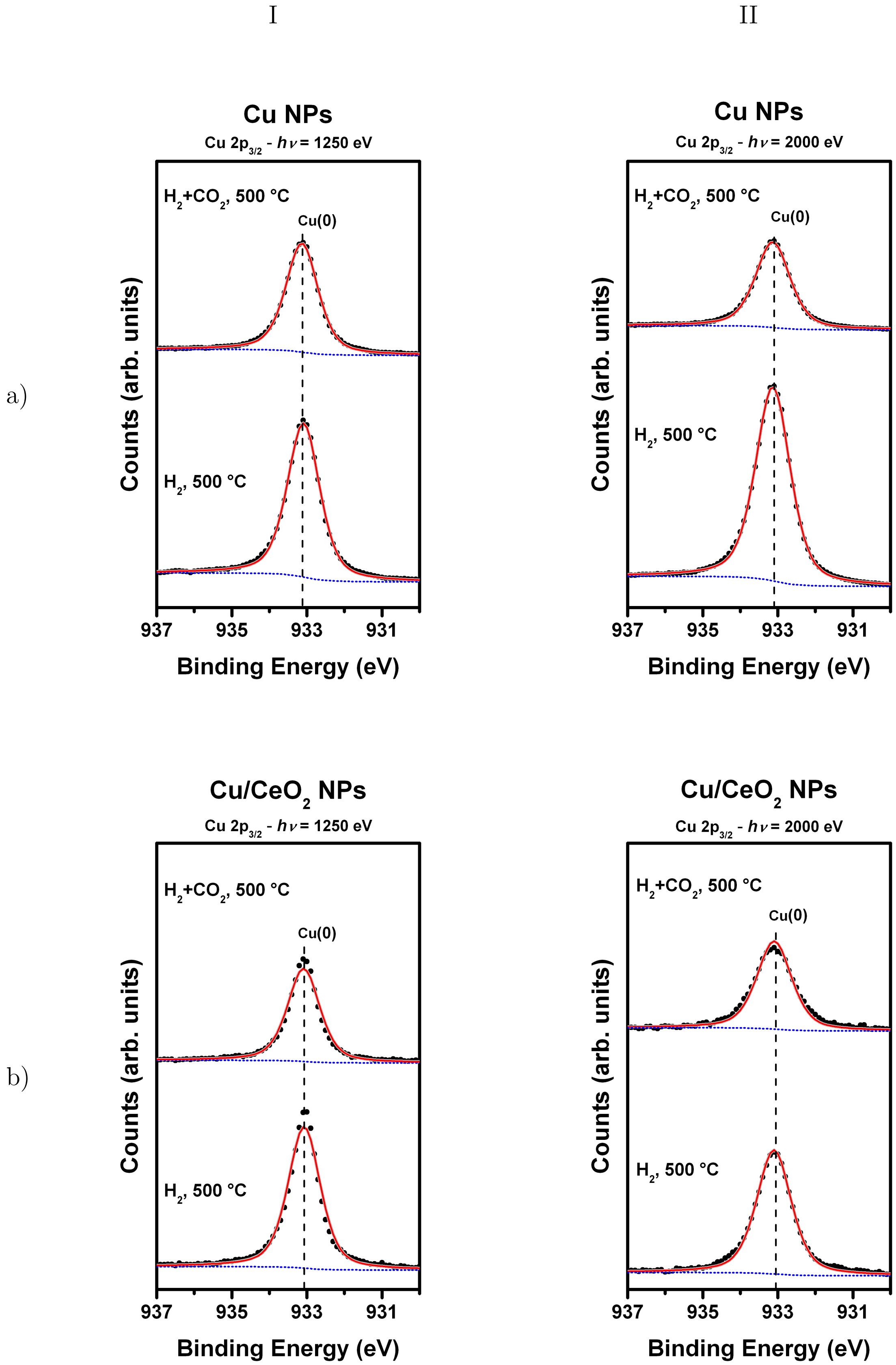
I
II
a)
b)
Cu NPs
Cu 2p3/2 - hν = 1250 eV
Cu 2p3/2 - hν = 2000 eV
Cu/CeO2 NPs
H2+CO2, 500 °C
H2, 500 °C
Cu(0)
Counts (arb. units)
Binding Energy (eV)
937
935
933
931

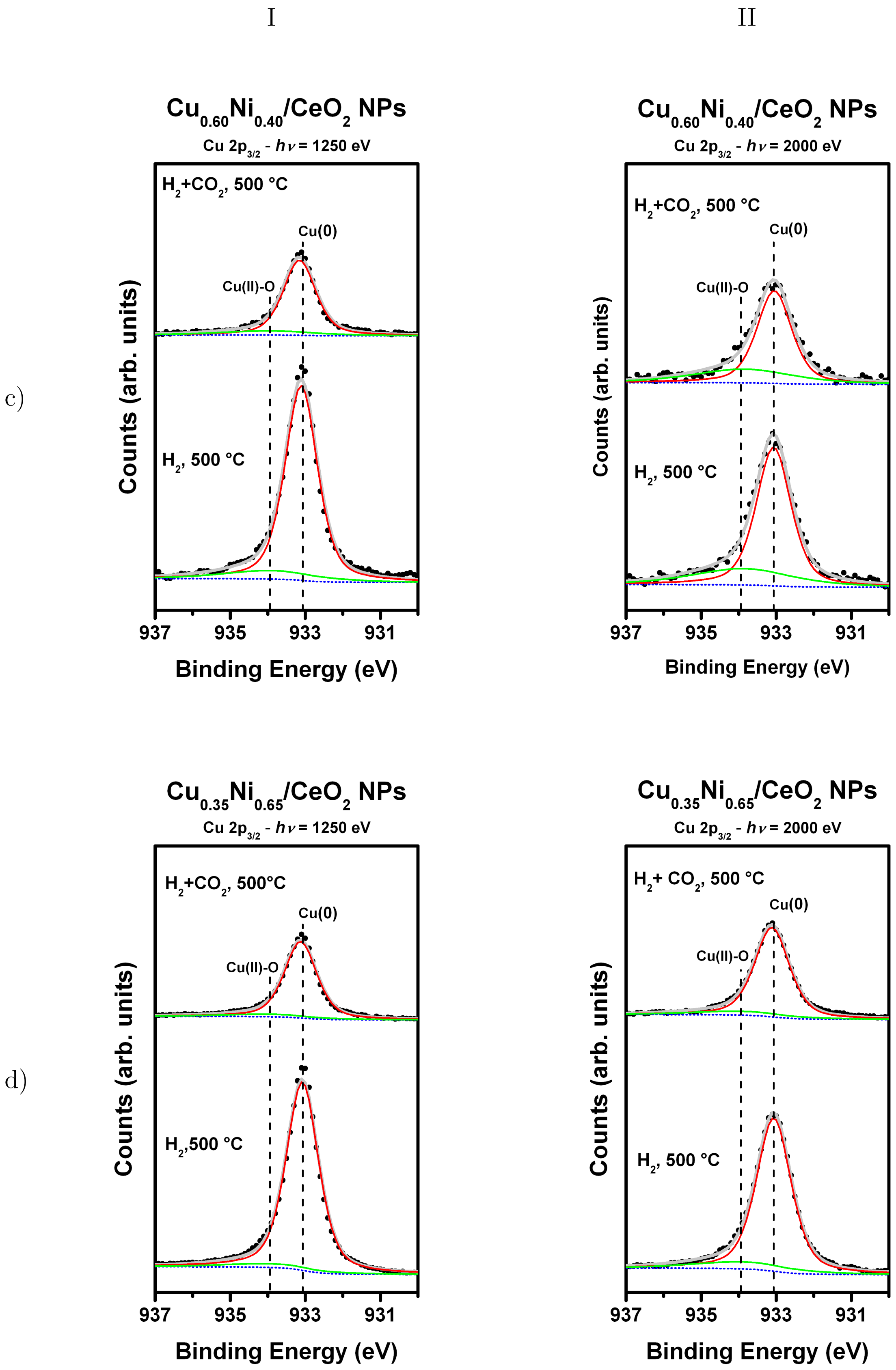
I
II
c)
Cu0.60Ni0.40/CeO2 NPs
Cu 2p3/2 - hν = 1250 eV
H2+CO2, 500 °C
Cu(0)
Cu(II)-O
H2, 500 °C
Counts (arb. units)
937
935
933
931
Binding Energy (eV)
Cu0.60Ni0.40/CeO2 NPs
Cu 2p3/2 - hν = 2000 eV
H2+CO2, 500 °C
Cu(0)
Cu(II)-O
H2, 500 °C
Counts (arb. units)
937
935
933
931
Binding Energy (eV)
d)
Cu0.35Ni0.65/CeO2 NPs
Cu 2p3/2 - hν = 1250 eV
H2+CO2, 500°C
Cu(0)
Cu(II)-O
H2,500 °C
Counts (arb. units)
937
935
933
931
Binding Energy (eV)
Cu0.35Ni0.65/CeO2 NPs
Cu 2p3/2 - hν = 2000 eV
H2+ CO2, 500 °C
Cu(0)
Cu(II)-O
H2, 500 °C
Counts (arb. units)
937
935
933
931
Binding Energy (eV)

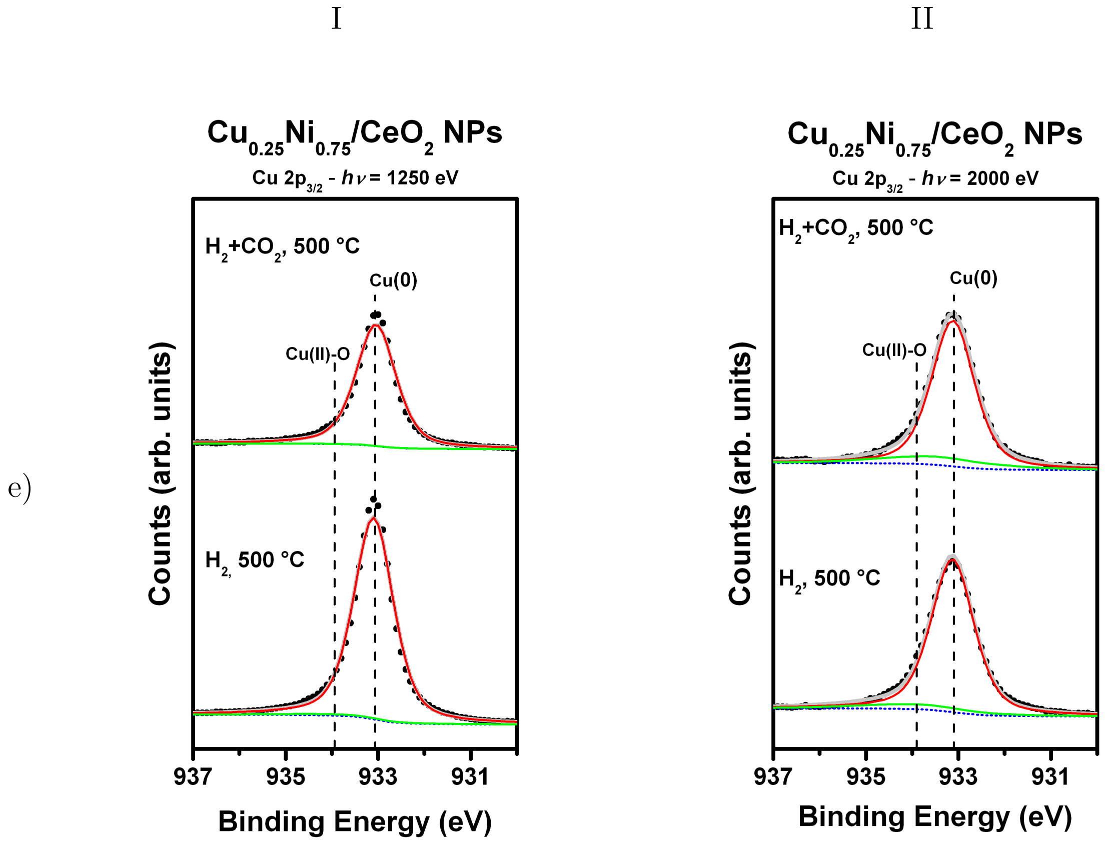

Figure 4.3.3 – Cu $2p_{3/2}$ NAP-XPS spectra for a) Cu NPs and $Cu_xNi_{1\text{-}x}/CeO_2$ NPs with b) x=1.00, c) x=0.60, d) x=0.35, and e) x=0.25, during reduction treatment (1 mbar H_2 atmosphere) and RWGS reaction (1 mbar H_2 + 1 mbar CO_2 atmosphere) measured with I) hν = 1250 eV, and II) hν = 2000 eV. The black points represent the experimental data, the dashed blue line the Shirley background used, the gray line the best fit performed with red and green solid lines representing the Cu(0) and Cu(II)-O components.

Table 4.6 – Binding energy positions and FWHM parameters used to fit the Cu $2p_{3/2}$ region in the $Cu_xNi_{1\text{-}x}/CeO_2$ (x=0.25, 0.35, 0.60, 1.00) and non-supported Cu NPs. The binding energy values are in accordance to [108, 110, 120].

Peak Identification	Position [eV]	FWHM [eV]	
		$h\nu$=1250 eV	$h\nu$=2000 eV
Cu(0)	933.1	1.02	1.09
Cu(II)-O	Cu(0)+0.8	3.00	3.21

Using the area associated to the different components determined in the fitting procedure of Cu $2p_{3/2}$ region, it was possible to determine the Cu(0) and Cu(II) fraction of each chemical compound in the Cu $2p_{3/2}$ region. Table 4.7 shows the fractions associated to the different chemical compounds found for the samples at $\lambda \approx 8$ Å (measurement at

$h\nu$=1250 eV) and $\lambda \approx 17$ Å(measurement at $h\nu$=2000 eV) depths, in the H_2 and H_2+CO_2 atmospheres.

Table 4.7 – Chemical component fraction used to fit the Cu2$p_{3/2}$ NAP-XPS region.

Atmosphere	Sample	$\lambda = 8$ Å		$\lambda = 17$ Å	
		%Cu(0)	%Cu(II)-O	%Cu(0)	%Cu(II)-O
1 mbar H_2	Cu NPs	100.0	0.0	100.0	0.0
	Cu/CeO_2 NPs	100.0	0.0	100.0	0.0
	$Cu_{0.60}Ni_{0.40}/CeO_2$ NPs	88.7	11.3	74.2	25.8
	$Cu_{0.35}Ni_{0.65}/CeO_2$ NPs	94.4	5.6	88.0	12.0
	$Cu_{0.25}Ni_{0.75}/CeO_2$ NPs	98.2	1.8	98.2	1.8
1 mbar H_2 +1 mbar CO_2	Cu NPs	100.0	0.0	100.0	0.0
	Cu/CeO_2 NPs	100.0	0.0	100.0	0.0
	$Cu_{0.60}Ni_{0.40}/CeO_2$ NPs	86.0	14.0	69.8	30.2
	$Cu_{0.35}Ni_{0.65}/CeO_2$ NPs	91.2	8.8	88.8	11.2
	$Cu_{0.25}Ni_{0.75}/CeO_2$ NPs	99.7	0.3	86.7	13.3

From the quantitative chemical component analysis shown in table 4.7 is clear to notice that, in the bimetallic cases, the Cu(II)-O fraction at the NPs is directly related to the amount of Cu on the samples. It is probably associated to a synergistic effect due to the presence of Ni atoms since no Cu oxidation is observed for supported and non-supported monometallic NPs. In order to clarify this effect is needed the study about the Cu surface population, as performed in Section 4.3.2.2.

4.3.2.2 Ni 2p region analysis

Figure 4.3.4 shows a comparison between the Ni 2$p_{3/2}$ NAP-XPS spectra in the H_2 and H_2+CO_2 atmospheres for each sample. It is clear the presence of a strong metallic component (Ni(0)), differently from the results observed on the as prepared NPs (see Figure 4.2.3). Also, there is the presence of a small chemical component associated to a hydroxide compound [112, 113]. The constrained parameters used to fit the Ni 2$p_{3/2}$ region are presented at Table 4.8.

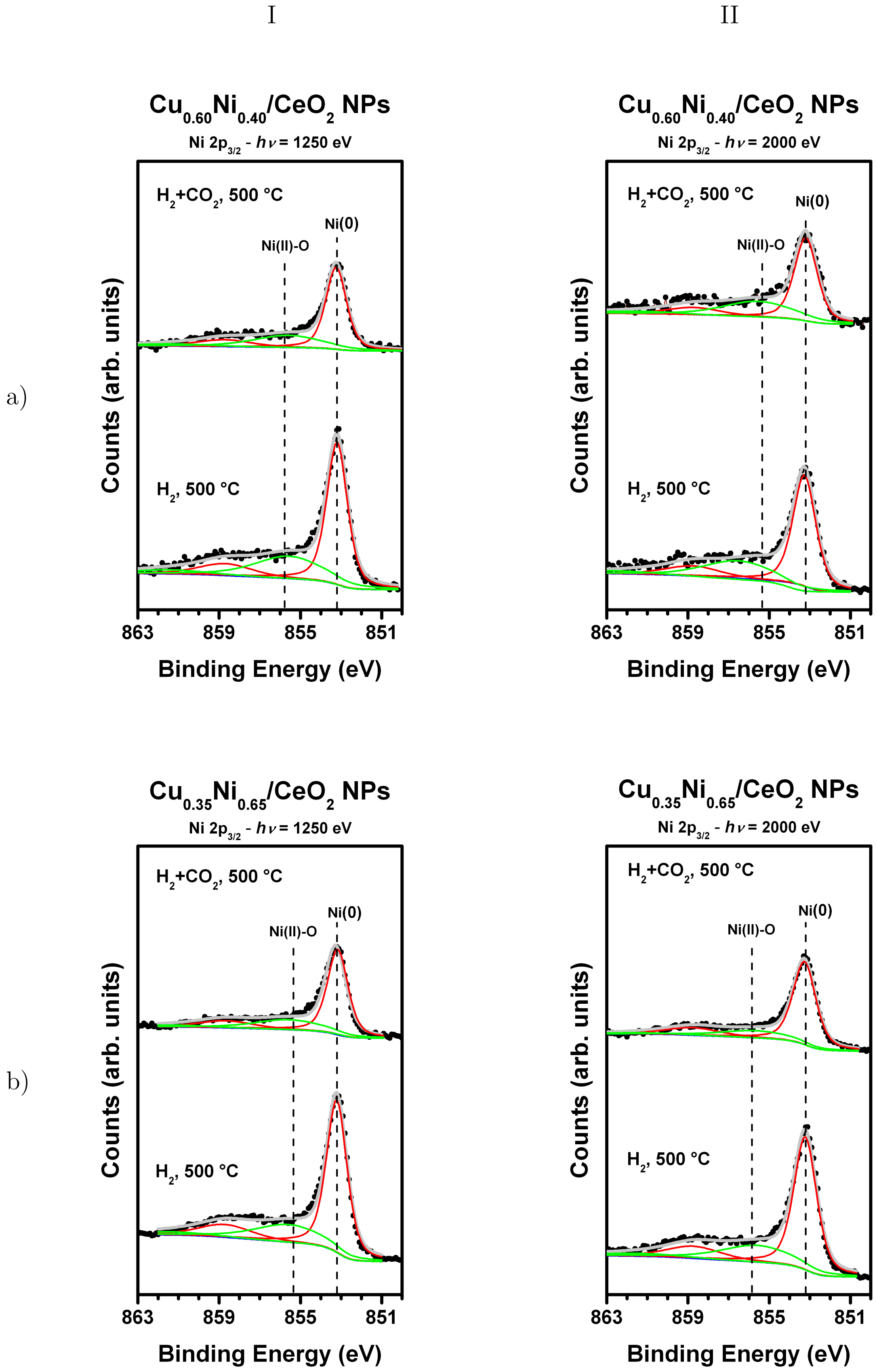
I
II
a)
b)
Cu0.60Ni0.40/CeO2 NPs
Ni 2p3/2 - hν = 1250 eV
Cu0.60Ni0.40/CeO2 NPs
Ni 2p3/2 - hν = 2000 eV
Cu0.35Ni0.65/CeO2 NPs
Ni 2p3/2 - hν = 1250 eV
Cu0.35Ni0.65/CeO2 NPs
Ni 2p3/2 - hν = 2000 eV
H2+CO2, 500 °C
H2, 500 °C
Ni(II)-O
Ni(0)
Counts (arb. units)
Binding Energy (eV)
863
859
855
851

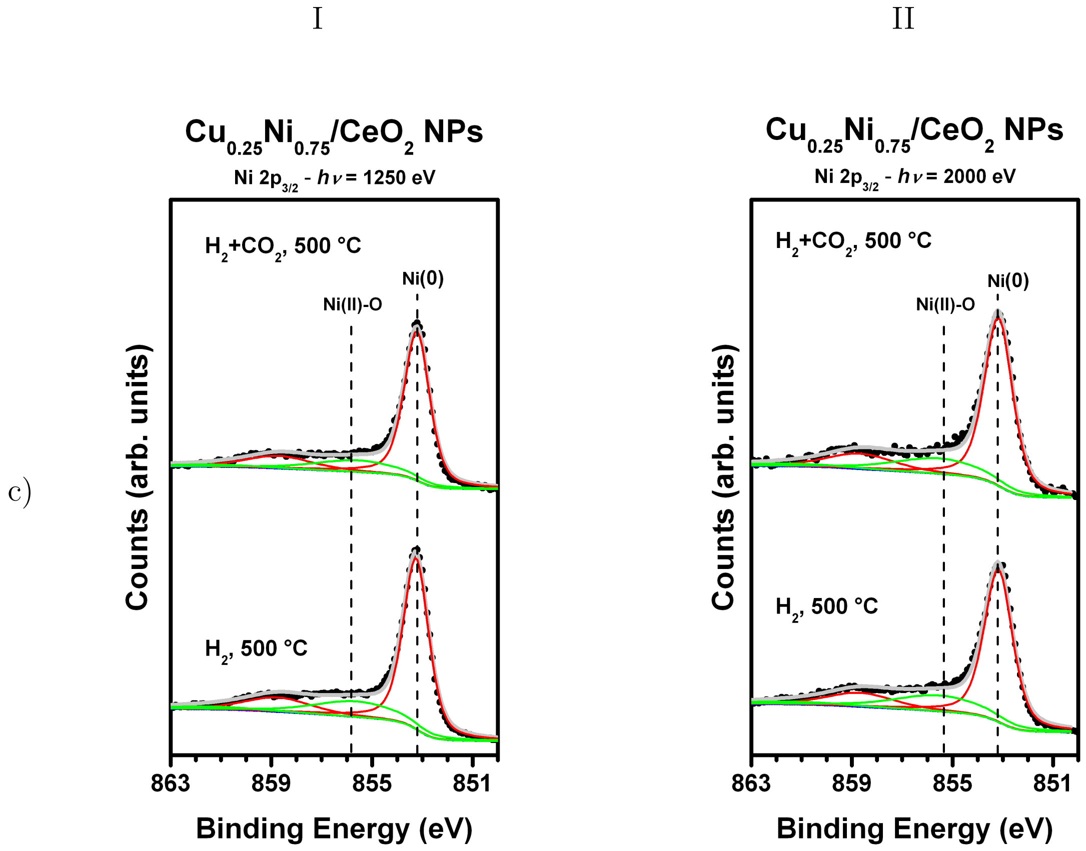

Figure 4.3.4 – Ni $2p_{3/2}$ NAP-XPS spectra for a) Cu NPs and Cu_xNi_{1-x}/CeO_2 NPs with b) x=1.00, c) x=0.60, d) x=0.35, and e) x=0.25, during reduction treatment (1 mbar H_2 atmosphere) and RWGS reaction (1 mbar H_2 + 1 mbar CO_2 atmosphere) measured with I) hν = 1250 eV, and II) hν = 2000 eV. The black points represent the experimental data, the dashed blue line the Shirley background used, the gray solid line the total fit performed using the red and green solid lines to represent the Ni(0) (with its respective satellite) and Ni(II)-O (with its respective satellite) components.

Table 4.8 – Binding energy positions and FWHM parameters used to fit the Ni $2p_{3/2}$ region in the Cu_xNi_{1-x}/CeO_2 (x=0.25, 0.35, 0.60) NPs. The binding energy values are in accordance to [112, 113, 121].

Peak Identification	Position [eV]	FWHM [eV]	
		$h\nu$=1250 eV	$h\nu$=2000 eV
Ni(0)	853.2	1.20	1.33
Ni(0) satellite	Ni(0)+5.5	3.16	3.20
Ni(II)-O	Ni(0)+2.35	4.00	4.20
Ni(II)-O satellite	Ni(II)-O+5.9	4.50	5.00

The chemical component fractions of the Ni $2p_{3/2}$ region was determined using the area values. These calculated percentages are presented in table 4.9.

Table 4.9 – Chemical components fractions used to fit the Ni $2p_{3/2}$ NAP-XPS region.

Atmosphere	Sample	$h\nu$=1250 eV		$h\nu$=2000 eV	
		%Ni(0)	%Ni(II)-O	%Ni(0)	%Ni(II)-O
1 mbar H_2	$Cu_{0.60}Ni_{0.40}/CeO_2$ NPs	66.1	33.9	65.7	34.3
	$Cu_{0.35}Ni_{0.65}/CeO_2$ NPs	72.6	27.4	72.0	28.0
	$Cu_{0.25}Ni_{0.75}/CeO_2$ NPs	77.0	23.0	81.6	18.4
1 mbar H_2 +1 mbar CO_2	$Cu_{0.60}Ni_{0.40}/CeO_2$ NPs	67.4	32.6	63.2	36.8
	$Cu_{0.35}Ni_{0.65}/CeO_2$ NPs	72.3	27.7	78.8	21.2
	$Cu_{0.25}Ni_{0.75}/CeO_2$ NPs	79.8	20.2	77.9	22.1

It is interesting to note that the Ni(0) component percentage is proportional to the Ni amount in the bimetallic NPs for both H_2 and H_2+CO_2 atmospheres. In other words, a lower Ni concentration gives a stronger Ni(II) component. Moreover, the same tendency is observed for the Cu, where the NPs with a lower amount of Ni (higher amount of Cu atoms) remains more oxidized during the reduction process. This effect is directly related to the Cu and Ni atomic population at the surface of the NPs as well the atomic structure of the catalyst. For the Ni $2p_{3/2}$ region is not observed a significant change in the Ni(II) fraction when changing the probed depth.

Combining the results from the fits of Cu $2p_{3/2}$ and Ni $2p_{3/2}$ regions is possible to analyze the atomic structure during thermal treatments in gaseous atmospheres by comparing the resultant intensities at the different depths probed by the $h\nu$=1250 eV and $h\nu$=2000 eV incident photons, *i.e.*, $\lambda \approx 8$ Å, and $\lambda \approx 17$ Å, respectively. Normalizing the areas from the Cu and Ni $2p_{3/2}$ fitted regions by the respective photoionization differential cross sections, the Cu/Ni normalized ratios were determined for the reduction treatment and RWGS reaction. Table 4.10 shows a sample comparison between the Cu/Ni normalized ratios on the surface and bulk regions from the Cu_xNi_{1-x}/CeO_2 (x=0.25, 0.35, 0.60) NPs for each characterization condition (as prepared; H_2, 500 °C; H_2+CO_2, 500 °C).

Table 4.10 – Cu/Ni normalized ratio at the Cu_xNi_{1-x}/CeO_2 (x=0.25, 0.35, 0.60) NPs for different probed depths during different treatments. The values presented in brackets indicates the probed depths by the XPS and NAP-XPS measurements and are associated to the inelastic mean free path of the photoelectrons analyzed.

Sample	Condition	Cu/Ni Intensity	
		Surface (λ)	Bulk (λ)
$Cu_{0.60}Ni_{0.40}/CeO_2$ NPs	As prepared	0.99 (11 Å)	2.73 (20 Å)
	1 mbar H_2, 500 °C	1.30 (8 Å)	1.56 (17 Å)
	1 mbar H_2+1 mbar CO_2, 500 °C	0.92 (8 Å)	1.42 (17 Å)
$Cu_{0.35}Ni_{0.65}/CeO_2$ NPs	As prepared	0.54 (11 Å)	1.12 (20 Å)
	1 mbar H_2, 500 °C	1.90 (8 Å)	1.51 (17 Å)
	1 mbar H_2+1 mbar CO_2, 500 °C	1.43 (8 Å)	1.53 (17 Å)
$Cu_{0.25}Ni_{0.75}/CeO_2$ NPs	As prepared	0.41 (11 Å)	1.31 (20 Å)
	1 mbar H_2, 500 °C	2.04 (8 Å)	2.06 (17 Å)
	1 mbar H_2+1 mbar CO_2, 500 °C	1.43 (8 Å)	1.94 (17 Å)

First of all, by comparing the Cu/Ni normalized ratio at the NPs surface for the H_2 atmosphere (8 Å) and the as prepared cases (11 Å), it is noticed an increase of this ratio with the H_2 reduction treatment. It is an indicative of Cu enrichment at the surface induced by the H_2 reduction treatment employed. It is in accordance to that predicted theoretically since Cu atoms have a smaller surface free energy than Ni atoms for a H_2 atmosphere (1.9 J/m^2 vs. 2.4 J/m^2) [122]. However, few studies exist in the literature concerning this issue but it is typically found the opposite behavior [54, 122]. Beaumont *et al.* [122] studied the surface segregation of atomic species in $Cu_{0.5}Ni_{0.5}$ and $Co_{0.5}Ni_{0.5}$ bimetallic NPs supported on SiO_2 and exposed to a H_2 (at 450 °C), CO (at 200 °C) or O_2 (at 350 °C) atmosphere by NAP-XPS and Scanning Transmission Electron Microscopy-Energy Dispersive Spectroscopy (STEM-EDS) techniques. The authors found that the H_2 atmosphere induces a Ni migration to the surface of $Cu_{0.5}Ni_{0.5}$ bimetallic NPs. The authors explain the difference found in comparison to the theoretical prediction by the fact that H_2 can dissociate easily on Ni surfaces and then the efficient chemisorption of H_2 molecules may induce the Ni segregation to the surface. In spite of this the authors affirm the need of a more detailed study about this system. One important difference between the present work and those found in the literature is the support used. The cited works study Cu-Ni/SiO_2 and Cu-Ni/TiO_2 NPs, not Cu-Ni/CeO_2 NPs. It is known that the support may have a strong influence on the atomic arrangement of bimetallic NPs as demonstrated in [42]. It may account for the differences found in both works. Table 4.10 also shows a change on the Cu/Ni normalized ratio when changing the incident photon energy for the H_2 reduction treatment case of a given sample. Depending on the case, this ratio at hν = 2000 eV may increase, decrease or to be the same than that for hν = 1250 eV. It shows that the core region of the NPs may have different atomic configurations with a Cu concentration higher, smaller or equal to that at the surface region. It occurs probably because the Cu migration to the surface of the NPs is not complete after 50 min of H_2 reduction treatment and the kinetics of Cu migration to the surface depends on the Cu and Ni concentrations.

The addition of CO_2 to the gaseous atmosphere induced a Ni enrichment process at the NPs surface for every sample, noticed by the decrease of the Cu/Ni ratio in about 28 % when compared to the H_2 atmosphere. The Ni migration towards NPs surface is probably due to the stronger interactions with CO_2, if compared to those presented by Cu [12].

The Cu/Ni ratios determined for the bimetallic samples in H_2 or H_2+CO_2 atmosphere can be directly related to the RWGS reactivity, where the samples presenting the higher Cu/Ni normalized ratios at NPs surface also yields higher CO and H_2O formation (presented in Figure 4.3.2). It is valid for the beginning of the RWGS reaction, that corresponds to the Cu/Ni normalized ratios at the end of the H_2 reduction treatment, or for the end of the RWGS reaction, associated to the measurement in the Ni/CeO2 NPs (not shown here), that corresponds to the Cu/Ni normalized ratios at the end of the H_2+CO_2 treatment. On the other hand, a surface with 100 % of Cu atoms, as the case of monometallic Cu/CeO_2 NPs, presents the lowest reactivity towards CO formation in the RWGS reaction. It shows an indicative of a synergistic effect between Cu and Ni atoms influencing the reactivity of these bimetallic NPs in the RWGS reaction. Furthermore, analyzing the beginning of the RWGS reaction, it is possible to notice a trend relating the Cu and Ni oxidation states at the bimetallic samples surface to the water desorption delay observed in the Figure 4.3.1. It is observed that higher Cu and Ni metallic fractions after H_2 reduction are associated to smaller delays in the H_2O detection at the MS. Since the same trend observed in the Cu and Ni metallic fraction is also observed for both H_2 or H_2+CO_2 atmospheres, it shows that the H_2O produced in the RWGS reaction may be bonded to specific sites associated to the oxidized species, being desorbed from the sample after a given period. It occurs between the end of the reduction treatment and the end of the RWGS reaction, then being not possible to see any change in the oxidation states in the NAP-XPS measurements, performed at the end of each H_2 and H_2+CO_2 treatment.

In this way, important features observed were clarified by the analysis at the Cu 2p and Ni 2p regions. However, some questions still remains open and the analysis at the Ce 3d region helps to clarify these points.

4.3.2.3 Ce 3d region analysis

Figure 4.3.5 shows the measured Ce 3d NAP-XPS region for each sample exposed to H_2 and H_2+CO_2 atmospheres at 500 °C as well the best fit result found. The fitting procedure of the Ce 3d NAP-XPS region was rather challenging. This region is characterized by complex distinct features related to the final state occupation of the Ce 4f level, changes in hybridization due to oxidation processes, and rearrangement of the electronic levels following the creation of a core hole [123]. This analysis was performed based on the binding energy constrains described by Schierbaum *et al.* [124], and using Burroughs's notation [125]. A total of 10 Gaussian peaks were used to fit the Ce 3d NAP-XPS region, in which 4 corresponds to the Ce(III) component (V_0, U_0, V', U') and 6 to the Ce(IV) component (V, U, V'', U'', V''', U'''). The Ce 3d spectra of the Ce(III) component consists of two pairs of $3d_{5/2}$-$3d_{3/2}$ doublets, therefore the area intensity ratio was set to 1.5 between the V and U doublets due to the degenerecency of these levels. The assignment of these peaks is somewhat controversial, however, they are usually associated to the initial state $Ce3d^{10}O2p^{6}Ce4f^{0}$ and $Ce3d^{10}O2p^{6}Ce4f^{1}$.

The peak labeled U''' at around 916 eV is a direct indicative of the oxidation state of the cerium oxide. The intensity of this single peak is proportional to the Ce(IV) fraction. Based on this, it is possible to observe a difference on the oxidation state of Ce atoms between samples for a given atmosphere. For a given sample exposed to a given atmosphere, the intensity of the U''' peak increases when increasing the incident photon energy (increase on the probed depth), then showing a higher Ce(III) fraction at the surface region of the cerium oxide. It shows that the cerium oxide reduction process starts at the surface region, as expected from the literature [126]. Also, the insertion of CO_2 gas did not change at all the intensity of the U''' peak in comparison to the case in the H_2 atmosphere for all the samples studied. In order to quantify the Ce(III) fraction present for each case, the fit of the Ce 3d region was performed.

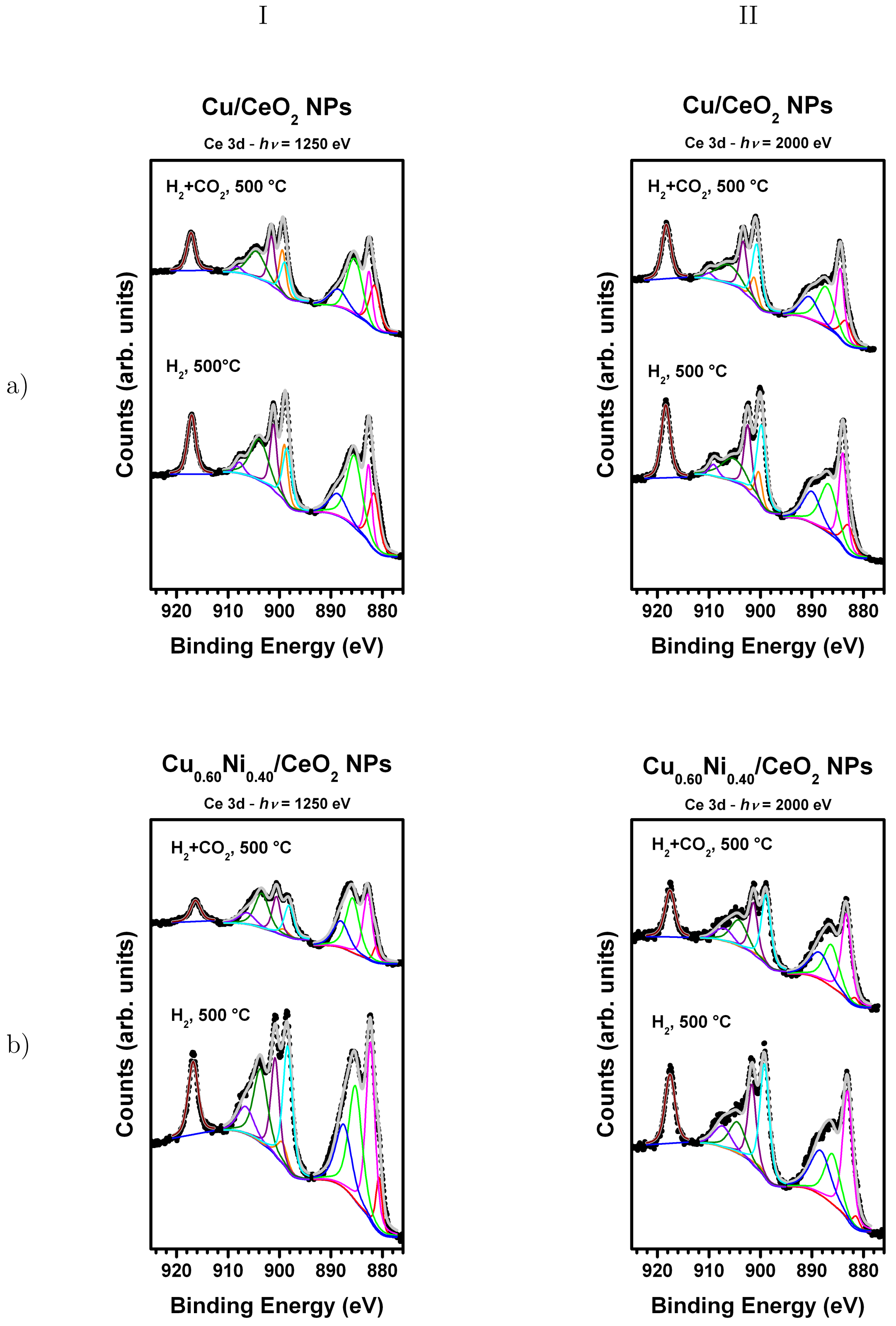
I
II
a)
b)
Cu/CeO2 NPs
Ce 3d - hν = 1250 eV
Ce 3d - hν = 2000 eV
Cu0.60Ni0.40/CeO2 NPs
H2+CO2, 500 °C
H2, 500°C
H2, 500 °C
Counts (arb. units)
Binding Energy (eV)
920
910
900
890
880

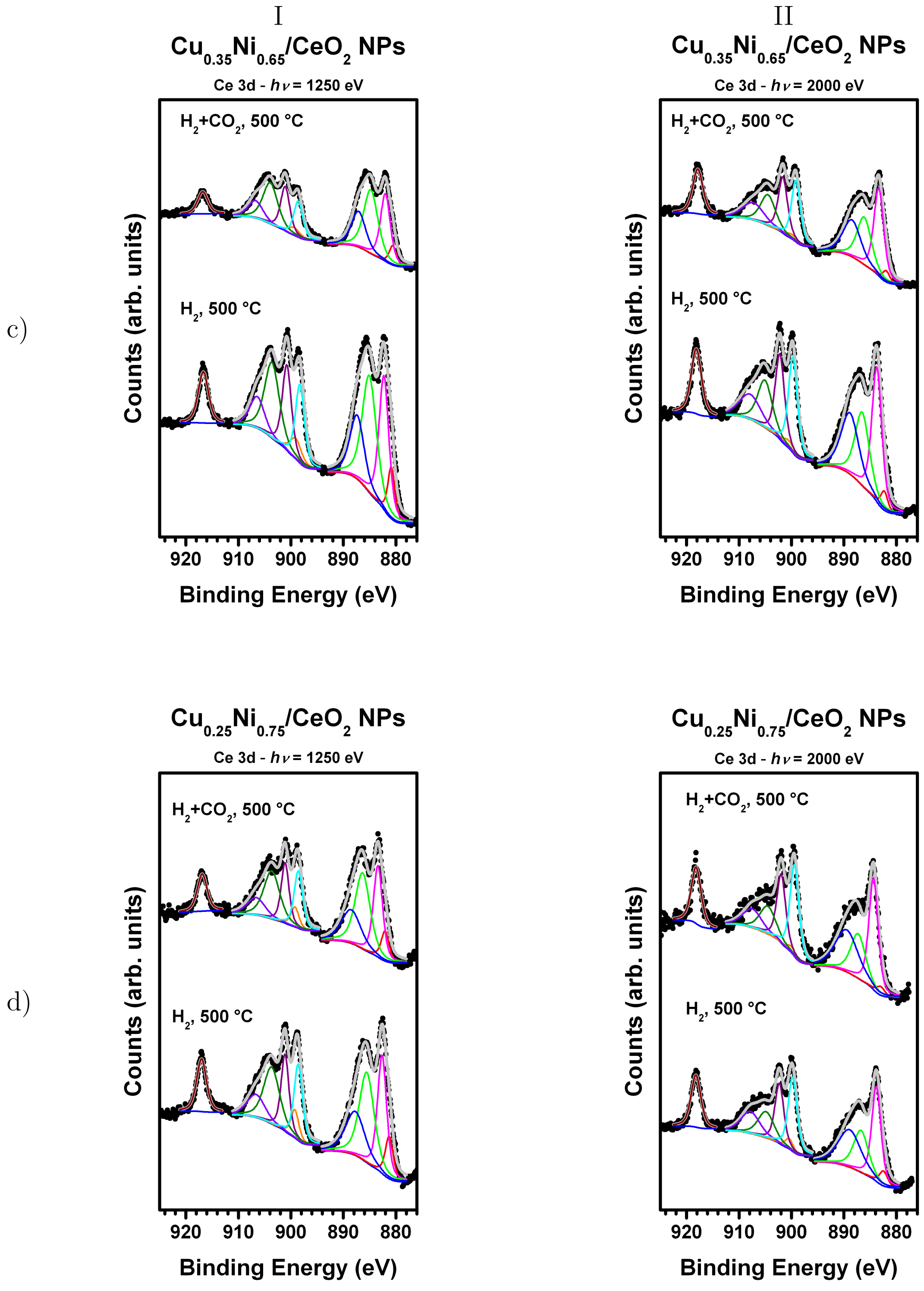

Figure 4.3.5 – Ce 3d NAP-XPS spectra for $Cu_xNi_{1\text{-}x}/CeO_2$ NPs with a) x=1.00, b) x=0.60, c) x=0.35, and d) x=0.25, during reduction treatment (1 mbar H_2 atmosphere) and RWGS reaction (1 mbar H_2 + 1 mbar CO_2 atmosphere) measured with I) hν = 1250 eV, and II) hν = 2000 eV. The black points represent the experimental data, the dashed blue line the Shirley background used, the gray solid line the total fit performed using the red, magenta, green, blue, orange, purple, olive, violet, cyan and wine solid lines to represent the V_0, V, V', V'', U_0, U, U', U'', V''', U''' components following the notation of Burroughs *et al.* [125].

Using a single parameters set for the Gaussian peaks used is not possible to perform a consistent fit throughout the atmospheric treatments for all the samples. Therefore, in order to achieve the best fit for all the samples at both incident photon energies, a *relaxation process* of the binding energy values was performed resulting in a set of parameters for each sample, though common to both atmospheres. However, some peaks needed energy shifts to fit the Ce 3d NAP-XPS region in the Cu/CeO_2 and $Cu_{0.60}Ni_{0.40}/CeO_2$ NPs exposed to the H_2 atmosphere. The parameters used to fit the Ce 3d peaks are presented in tables 4.11 to 4.14, in which the values colored in red indicate the shift needed to fit the Cu/CeO_2 and $Cu_{0.60}Ni_{0.40}/CeO_2$ NPs Ce 3d NAP-XPS region in the H_2 atmosphere.

The binding energy values are presented always constrained to the V_0 peak position, which has the energy position value coherent to that described in the Schierbaum discussion [127]. The energy shifts indicated in red corresponds to the case where a lower $\mathcal{R}$-factor was found in the fitting procedure between several possible parameters of the peaks used.

Table 4.11 – Parameters used to fit the Ce 3d region in the Cu/CeO_2 NPs exposed to 1 mbar H_2 and 1 mbar H_2 + 1 mbar CO_2 atmospheres. The values colored in red are shifts needed to fit the $V' - U'$ peaks in the H_2 atmosphere.

Peak Identification	Position [eV]	FWHM [eV]	
		$h\nu$=1250 eV	$h\nu$=2000 eV
V_0	882.04	2.36	2.51
V	V_0+1.05	1.51	1.80
V'	V_0+3.85(-0.05)	3.48	3.97
V''	V_0+7.04	3.93	3.93
V'''	V_0+16.88	1.98	2.09
U_0	V_0+17.38	1.57	1.62
U	V_0+19.50	1.59	1.73
U'	V_0+22.40(-0.14)	4.04	5.63
U''	V_0+26.12	2.05	2.05
U'''	V_0+35.44	1.95	2.12

Table 4.12 – Parameters used to fit the Ce3d region in the $Cu_{0.60}Ni_{0.40}/CeO_2$ NPsexposed to 1 mbar H_2 and 1 mbar H_2 + 1 mbar CO_2 atmospheres. The values colored in red indicate the shift needed to fit the $V'' - U''$ peaks in H_2 atmosphere.

Peak Identification	Position [eV]	FWHM [eV]	
		$h\nu$=1250 eV	$h\nu$=2000 eV
V_0	881.58	1.42	1.69
V	V_0+1.65	2.10	2.22
V'	V_0+4.58	3.07	3.52
V''	V_0+6.86(+0.24)	3.61	4.64
V'''	V_0+17.74	2.16	2.16
U_0	V_0+18.80	2.46	2.88
U	V_0+20.18	1.93	1.93
U'	V_0+23.01	3.20	3.78
U''	V_0+25.89(+0.41)	3.66	3.84
U'''	V_0+36.11	2.34	2.34

Table 4.13 – Parameters used to fit the Ce3d region in the $Cu_{0.35}Ni_{0.65}/CeO_2$ NPsexposed to 1 mbar H_2 and 1 mbar H_2 + 1 mbar CO_2 atmospheres.

Peak Identification	Position [eV]	FWHM [eV]	
		$h\nu$=1250 eV	$h\nu$=2000 eV
V_0	881.77	1.60	1.62
V	V_0+1.40	2.22	2.22
V'	V_0+4.19	3.22	3.22
V''	V_0+6.52	3.21	3.98
V'''	V_0+17.40	2.02	2.02
U_0	V_0+18.20	2.70	2.70
U	V_0+19.89	2.06	2.09
U'	V_0+22.73	3.32	3.32
U''	V_0+25.54	3.28	4.79
U'''	V_0+35.81	2.34	2.34

Table 4.14 – Parameters used to fit the Ce3d region in the $Cu_{0.25}Ni_{0.75}/CeO_2$ NPs exposed to 1 mbar H_2 and 1 mbar H_2 + 1 mbar CO_2 atmospheres.

Peak Identification	Position [eV]	FWHM [eV]	
		$h\nu$=1250 eV	$h\nu$=2000 eV
V_0	881.77	1.81	1.89
V	V_0+1.35	2.07	2.07
V'	V_0+4.28	3.37	3.37
V''	V_0+6.45	4.35	5.09
V'''	V_0+17.32	1.91	2.02
U_0	V_0+17.97	1.83	1.83
U	V_0+19.84	1.78	1.99
U'	V_0+22.39	3.57	3.60
U''	V_0+25.36	4.01	4.17
U'''	V_0+35.75	2.22	2.22

The necessity for the energy shift in the V', U' and V'', U'' peaks in the different atmospheres can be explained by the electronic states related to these peaks. It is known that the Ce 4f orbitals may overlap to the O 2p ones [127, 128]. The states associated to the $V'{-}U'$ and $V''{-}U''$ peaks are $|Ce3d^{10}O2p^6Ce4f^1\rangle$ and $|Ce3d^{10}O2p^64f^0\rangle$, which corresponds to Ce(III) and Ce(IV) oxidation states, respectively. The interactions between Ce 4f and O 2p electronic levels are probably associated to changes in the Ce atoms neighborhood, shifting the Ce(III) doublet to lower binding energies and the Ce(IV) doublet to higher binding energies.

It is possible to determine the Ce(III) fraction in the cerium oxide support during the gas treatments. This fraction was determined by the fractional contribution of the $V_0 - U_0$ and $V' - U'$ doublets to the total area of the Ce 3d region. The fraction is calculated as

$$\%Ce(III) = \frac{[V_0]+[V']+[U_0]+[U']}{[V_0]+[V]+[V']+[V'']+[V''']+[U_0]+[U]+[U']+[U'']+[U''']} \tag{4.1}$$

where the brackets indicate the peaks intensities. The fractions calculated using 4.1 are presented on table 4.15.

Table 4.15 – Ce(III) fraction of the samples during the 1 mbar H_2 and 1 mbar H_2 + 1 mbar CO_2 exposition at 500 °C.

Atmosphere	Sample	%Ce(III)	
		$h\nu$=1250 eV	$h\nu$=2000 eV
1 mbar H_2	Cu/CeO_2 NPs	53	55
	$Cu_{0.60}Ni_{0.40}/CeO_2$ NPs	34	23
	$Cu_{0.35}Ni_{0.65}/CeO_2$ NPs	42	27
	$Cu_{0.25}Ni_{0.75}/CeO_2$ NPs	41	25
1 mbar H_2 + 1 mbar CO_2	Cu/CeO_2 NPs	53	40
	$Cu_{0.60}Ni_{0.40}/CeO_2$ NPs	41	27
	$Cu_{0.35}Ni_{0.65}/CeO_2$ NPs	42	27
	$Cu_{0.25}Ni_{0.75}/CeO_2$ NPs	42	22

A common trend is observed in Table 4.15 concerning the Ce(III) fraction values, in which the samples have its surface more reduced then its inner regions. This feature was expected since the atoms at the samples surface reacts more with the atmosphere than the inner ones [126]. The treatment into the H_2+CO_2 atmosphere did not presented effective oxidation on the Ce support since the Ce(III) fraction values presented essentially no alteration.

Based on the results presented in Table 4.15 is still not clear the reason for the energy shift observed for peaks in the Ce 3d region for the Cu/CeO_2 and $Cu_{0.60}Ni_{0.40}/CeO_2$ NPs.

Thereafter, the total intensity of the Ce 3d region was associated to the Cu and Ni $2p_{3/2}$ NAP-XPS regions and used to calculate the (Cu $2p_{3/2}$ + Ni $2p_{3/2}$)/(Ce 3d) ratio normalized by the differential cross section values. The (Cu $2p_{3/2}$ + Ni $2p_{3/2}$)/(Ce 3d) fraction is presented on Table 4.16 as a function of the gaseous atmosphere and sample for the depths of 8 Å and 17 Å.

Table 4.16 – (Cu $2p_{3/2}$ + Ni $2p_{3/2}$)/(Ce 3d) normalized ratio obtained from the NAP-XPS measurements in 1 mbar H_2 and 1 mbar H_2 + 1 mbar CO_2 atmospheres for Cu_xNi_{1-x}/CeO_2 (x = 0.25, 0.35, 0.60, 1.00) NPs.

Sample	Atmosphere	(Cu $2p_{3/2}$ + Ni $2p_{3/2}$)/(Ce 3d) Intensity (8 Å)	(17 Å)
Cu/Ce_2 NPs	1 mbar H_2	0.22	0.38
	1 mbar H_2+1 mbar CO_2	0.21	0.23
$Cu_{0.60}Ni_{0.40}/CeO_2$ NPs	1 mbar H_2	0.29	0.34
	1 mbar H_2+1 mbar CO_2	0.36	0.37
$Cu_{0.35}Ni_{0.65}/CeO_2$ NPs	1 mbar H_2	0.80	0.82
	1 mbar H_2+1 mbar CO_2	0.73	0.73
$Cu_{0.25}Ni_{0.75}/CeO_2$ NPs	1 mbar H_2	2.41	2.19
	1 mbar H_2+1 mbar CO_2	2.07	2.07

The analysis of Table 4.16 shows that, by comparing the (Cu $2p_{3/2}$ + Ni $2p_{3/2}$)/(Ce 3d) fractions in H_2 atmosphere observed for the surface (8 Å) and inner (17 Å) regions of the $Cu_{0.60}Ni_{0.40}/CeO_2$ and Cu/CeO_2 NPs, it is possible to observe that there is a decrease of the ratio when decreasing the probed depth (from the inner to the surface region). It shows a higher contribution of the Ce 3d NAP-XPS intensity for regions closer to the surface of the catalysts. It is a strong indicative of the existence of the SMSI effect with a CeO_x capping layer covering the metallic NPs. After insertion of the CO_2 atmosphere, the change on the ratio with the probed depth disappears and there is no more evidence of the SMSI effect occurrence. In fact, it is known from the literature that an oxidizing treatment at high temperatures recover the catalyst to the initial condition, without the capping layer presence [58]. It is interesting to note that the geometrical factor of the SMSI effect occurs only for those samples that presented an energy shift in some peak positions used in the fit of the Ce 3d NAP-XPS region and that this energy shift exists only for the H_2 atmosphere, when is observed the capping layer covering the NPs. Then, there is a strong evidence for the elucidation of the nature of the SMSI effect, that occurs trough interaction of the $Ce3d^{10}O2p^6Ce4f^1$ (Cu/CeO_2 NPs) and $Ce3d^{10}O2p^6Ce4f^0$ ($Cu_{0.60}Ni_{0.40}/CeO_2$ NPs) initial states with the neighborhood composed by Cu and Ni atoms. Moreover, the changes observed in the Ce(III) fraction in H_2 atmosphere between samples can be explained by the nature of the SMSI effect too. For the case of $Cu_{0.60}Ni_{0.40}/CeO_2$ NPs the SMSI effect occurs through interaction of the NPs with Ce atoms in the $Ce3d^{10}O2p^6Ce4f^0$ initial state, associated to a Ce(IV) oxidation state. This sample has the smaller Ce(III) fraction at the surface between all the cases studied (Table 4.15). On the other hand, the Cu/CeO_2 NPs presents the SMSI effect occuring via interaction of the NPs with the Ce atoms in the $Ce3d^{10}O2p^{6}Ce4f^{1}$ initial state, associated to the Ce(III) oxidation state. Moreover, this sample is the case of highest Ce(III) fraction observed in Table 4.15. Even considering the SMSI effect is greatly investigated nowadays [62, 46], for the best of our knowledge this is the first time that such a detailed description of the nature of the SMSI effect is obtained.

Table 4.16 also shows a dependence of the existence of the SMSI effect with the Cu amount in the NPs. It is observed that the SMSI effect occurs only for those samples with higher Cu concentrations, namely $x = 1.0$ and $x = 0.60$. It shows the existence of a threshold for the beginning of the SMSI effect. However, in a previous work, Matte *et al.* studied the reduction process of Cu/CeO_2 and Ni/CeO_2 monometallic NPs exposed to a H_2 atmosphere at 500 °C by *ex situ* XPS, *in situ* XAS and *in situ* time-resolved XAS measurements, and the SMSI effect was observed only for the Ni/CeO_2 NPs [60]. The difference between both works lays on the chemical composition of the NPs surface before the reduction treatment under H_2 atmosphere. The NPs studied here presented a surface rich in Cu-Cl and Ni-O chemical states, while the NPs studied by *Matte et al.* presented Cu-O and Ni-Cl rich surfaces. These differences may explain the opposite observations, since Cl atoms have important influence on the SMSI occurrence as reported in [129, 130, 131, 132].

In the NAP-XPS analysis at the Cu $2p_{3/2}$ region (Table 4.7) was observed an increase on the Cu(II) fraction for increasing probed depths in bimetallic NPs. It can be explained considering the SMSI effect. The effect should be understood as a statistical process that happens significantly for Cu amounts higher than a given threshold value. Then, when probing the surface region of the NPs in fact it is being probed the surface region of clean surface bimetallic NPs and the capping layer of the bimetallic NPs that suffered the SMSI effect. When probing a higher depth it is being probed the inner region of clean surface bimetallic NPs but also the surface region of bimetallic NPs covered by the capping layer, then probing oxidizes states. The change of Cu(II) fraction with the change of probed depth depends on the mean shell thickness value of the capping layer, which was not investigated and may depend on the bimetallic NPs nature.

The observation related in Section 4.3.2.1 and 4.3.2.2 concerning the higher fraction of Cu(II) and Ni(II) oxidized states for higher amounts of Cu concentration (Tables 4.7 and 4.9) can now be explained considering the SMSI effect. The higher Cu amount in bimetallic NPs gives a more evident SMSI effect which induces the existence of Cu(II) and Ni(II) oxidized states. The case of monometallic Cu/CeO_2 NPs presents no Cu(II) component and the SMSI effect is detected for this system. It may be related to the different interaction of the capping layers with Cu atoms in this case which happens via Ce(III) entities ($Ce3d^{10}O2p^{6}Ce4f^{1}$ initial state).

The occurrence of the SMSI effect may be related to the low H_2O-CO productions observed for these samples in Figure 4.3.2. Once the NPs promote the CO_2 dissociation, the Cu/CeO_2 and $Cu_{0.60}Ni_{0.40}/CeO_2$ NPs surface are partially hidden by a CeO_x capping layer which inhibits the H_2 chemisorption capacity, as stated in the literature [133, 134]. Furthermore, considering the known cerium oxide hydrophilicity, the shell formed covering these NPs may induce a long time interaction between water molecules and the cerium oxide support until a H_2O saturation concentration is reached and the H_2O desorption process starts. This phenomenon explains the longer delay for the H_2O desorption process in Cu/CeO_2 NPs than for the $Cu_{0.25}Ni_{0.75}/CeO_2$ NPs, even considering the higher fraction of oxidized species in the $Cu_{0.25}Ni_{0.75}/CeO_2$ NPs case. As discussed in Section 4.3.2.2, the H_2O desorption process is directly related to the metal oxidized species amount for bimetallic NPs. The monometallic case, Cu/CeO_2 NPs, does not present the Cu-O component during H_2 reduction treatment but the capping layer accounts for the delay on the H_2O desorption observed. The case with longer delay of H_2O desorption between all the samples analyzed occurs for the $Cu_{0.60}Ni_{0.40}/CeO_2$ NPs sample that presents the highest Cu-O and Ni-O fractions and the existence of the SMSI effect.

4.3.2.4 O 1s region analysis

Figure 4.3.6 shows a comparison between the O 1s region for the $Cu_xNi_{1\text{-}x}/CeO_2$ (x=0.25, 0.35, 0.60, 1.00) NPs and the non-supported Cu NPs. The NAP-XPS measurements at this region revealed several chemical components, in which some of them are related to Ce-O, Ni-O, Cu-O bonds or molecules adsorbed in the samples surface.

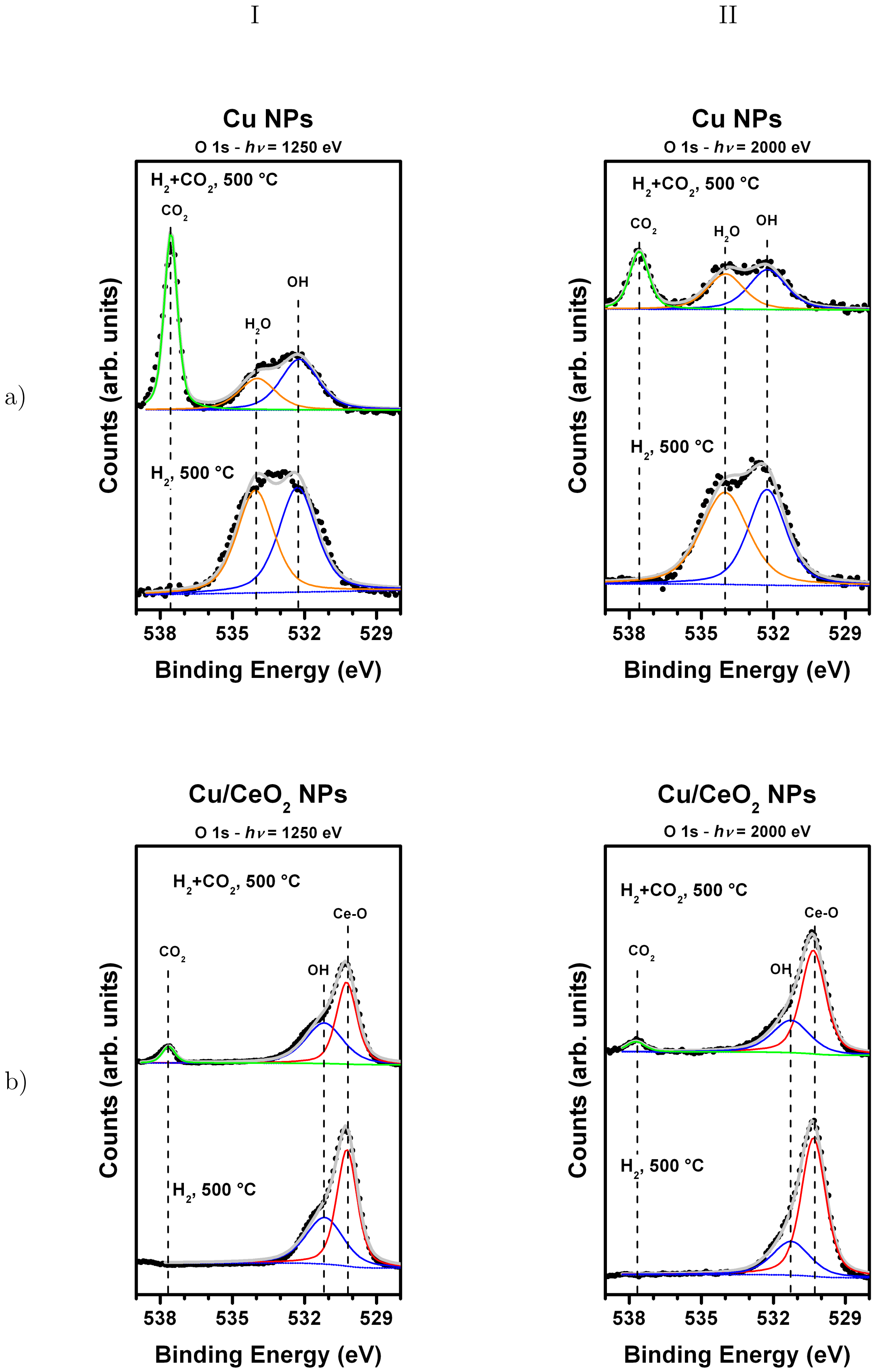
I
II
a)
b)
Cu NPs
O 1s - hν = 1250 eV
O 1s - hν = 2000 eV
H2+CO2, 500 °C
H2, 500 °C
CO2
H2O
OH
Cu/CeO2 NPs
Ce-O
Counts (arb. units)
Binding Energy (eV)
538
535
532
529

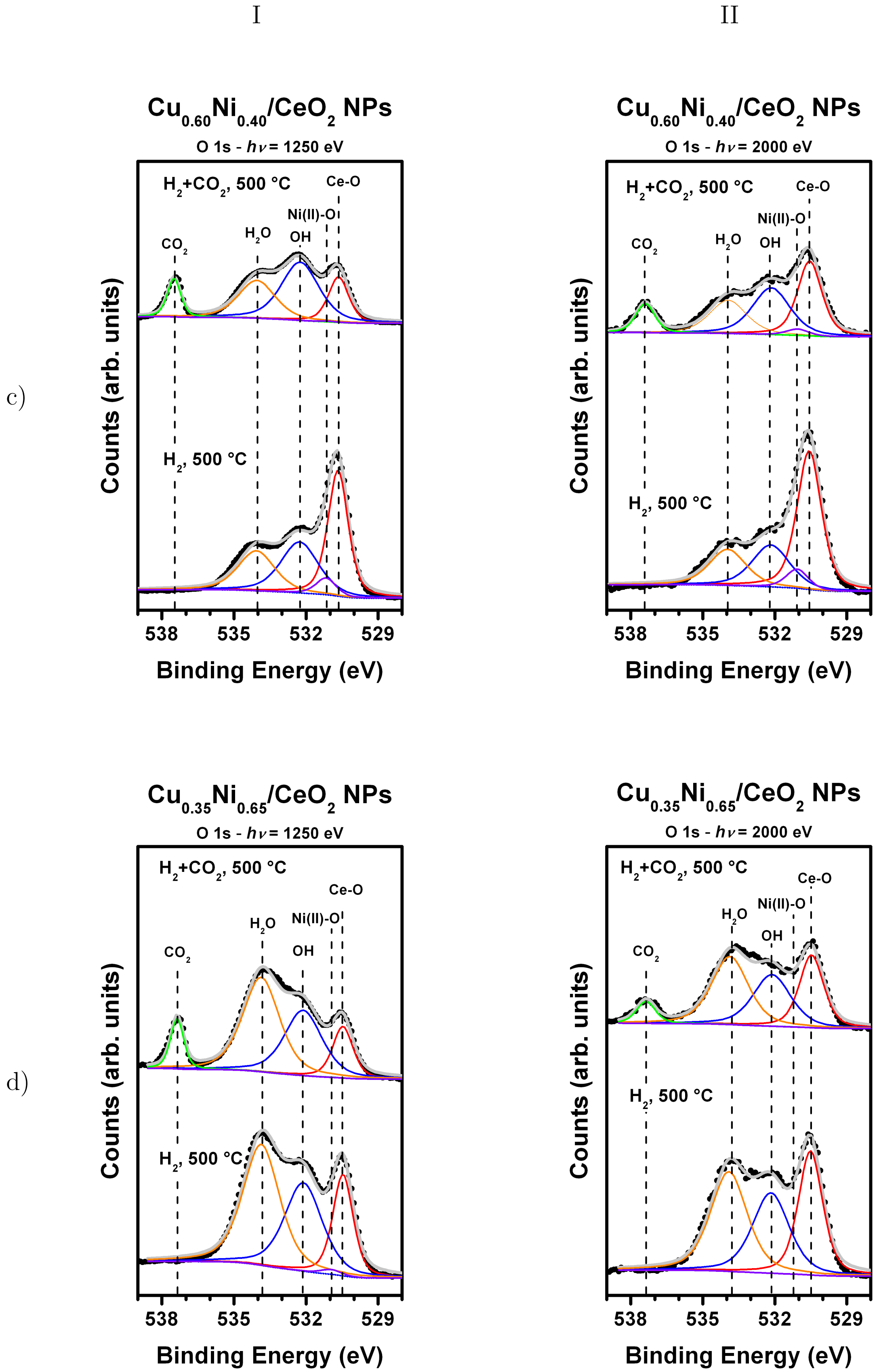
I
II
c)
Cu0.60Ni0.40/CeO2 NPs
O 1s - hν = 1250 eV
H2+CO2, 500 °C
H2, 500 °C
CO2
H2O
OH
Ni(II)-O
Ce-O
Counts (arb. units)
538
535
532
529
Binding Energy (eV)
Cu0.60Ni0.40/CeO2 NPs
O 1s - hν = 2000 eV
d)
Cu0.35Ni0.65/CeO2 NPs
O 1s - hν = 1250 eV
Cu0.35Ni0.65/CeO2 NPs
O 1s - hν = 2000 eV

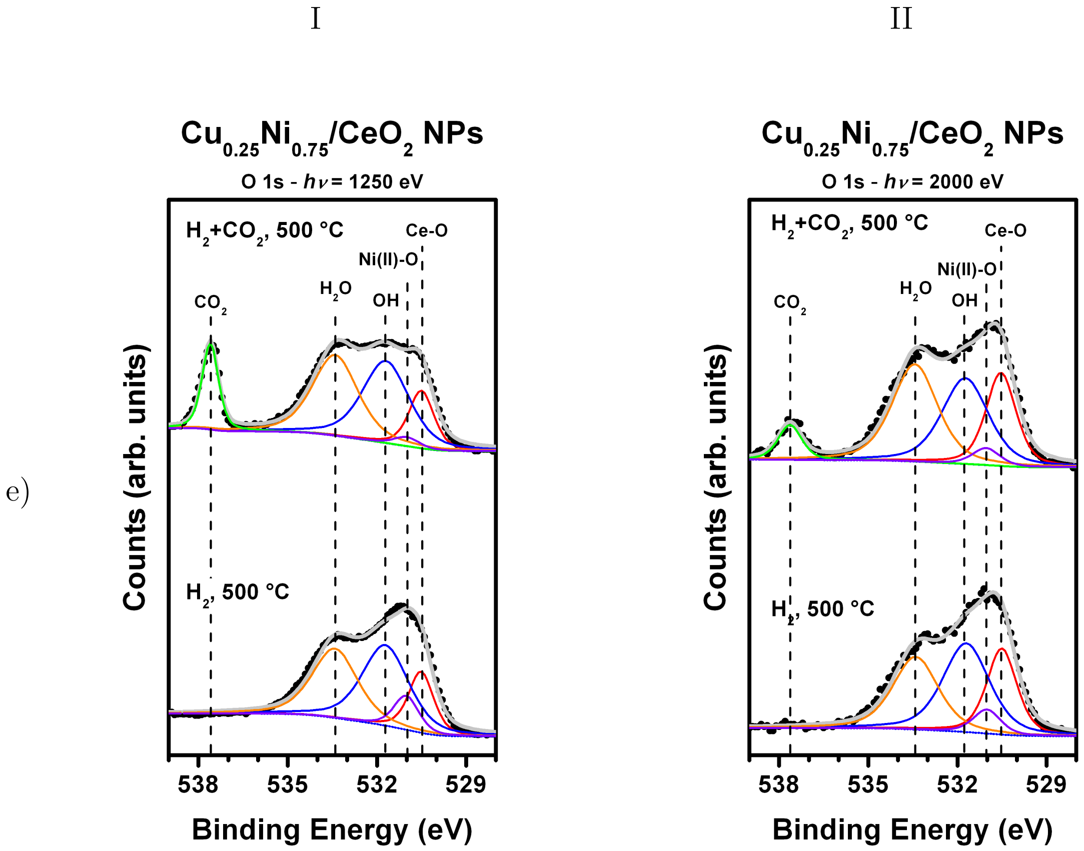

Figure 4.3.6 – O1s NAP-XPS spectra for a) Cu NPs and $Cu_xNi_{1\text{-}x}/CeO_2$ NPs with b) x=1.00, c) x=0.60, d) x=0.35, and e) x=0.25, during reduction treatment (1 mbar H_2 atmosphere) and RWGS reaction (1 mbar H_2 + 1 mbar CO_2 atmosphere) measured with I) hν = 1250 eV, and II) hν = 2000 eV. The black points represent the experimental data, the dashed blue line the Shirley background used, the gray line is the total fit performed using the red, blue, orange, green and violet solid lines to represent the Ce-O, OH, H_2O, CO_2 and Ni(II)-O components.

Table 4.17 – Binding energy positions and FWHM parameters used to fit the O 1s region in the $Cu_xNi_{1\text{-}x}/CeO_2$ (x=0.25, 0.35, 0.60, 1.00) and non-supported Cu NPs. Values are in accordance to [90, 111, 112, 113, 135, 136].

Peak Identification	Position [eV]	FWHM [eV]	
		$h\nu$=1250 eV	$h\nu$=2000 eV
OH	532.29	1.80	1.80
Ce-O	OH-1.65	1.00	1.20
H_2O	OH+1.75	1.85	1.85
CO_2	OH+5.3	0.65	0.94
Ni(II)-O	OH-1.15	1.00	1.10

The CO_2 component at 537.59 eV comes from the gas phase present during the RWGS reaction. The Ce-O component at 530.64 eV comes due to the support, then not occurring for the non-supported NPs. This component is visually more pronounced for the Cu/CeO_2 and $Cu_{0.60}Ni_{0.40}/CeO_2$ NPs during the H_2 reduction treatment at 500 °C. It corroborates the existence of the capping layer covering the metallic NPs since in this case the Ce-O component comes from the support and the capping layer region. The OH and H_2O components around 533 eV shows the existence of transient species during RWGS reaction. The Cu-O component is expected around 530.7 eV, that is very similar to the Ce-O component, then being hard to distinguish between them in this analysis. H_2O bonds are still detected, though in low intensity, on the Cu/CeO_2 NPs and $Cu_{0.60}Ni_{0.40}/CeO_2$ NPs. This result is in accordance with the Mass Spectrometry measurements, since these are the samples that present lower H_2O formation. The detection of this signal in the H_2 atmosphere indicates a tendency for the H_2O molecules (in this case, from the synthesis process) to stay adsorbed at samples surface, while these signal in the H_2+CO_2 is primarily due to the RWGS reaction formations.

4.3.3 *In situ* XAS measurements

In situ XAS measuremets were carried out at the XDS and DXAS beamlines [87, 137] at the Brazilian Synchrotron Light Laboratory (LNLS) in Campinas, Brazil.

At the XDS beamline, X-rays emitted by a superconducting wiggler source are vertically collimated by a Si mirror, passes through a Si(111) double crystal monochromator and are focused in a toroidal Rh mirror. This radiation was measured in a primary ionization chamber filled with 20% Ar + 80%N_2, then passed through the sample, and the transmitted radiation was detected in a secondary ionization chamber filled with 10% Ar + 90%N_2. The XAS measurements, performed in the transmission mode, probed the Ni K edge at 8333 eV and the Cu K edge at 8979 eV of the Cu_xNi_{1-x}/CeO_2 (x=0.25, 0.35, 0.60, 1.00) and non-supported Cu NPs. For these measurements, pellets were produced by compressing a mix of the as prepared samples powder and BN. For the non-supported NPs pellet was used 30mg of the sample's powder and 80mg of BN, while in the supported samples each pellet used a mix of 45mg of sample's powder and 55mg of BN. XANES and EXAFS measurements were performed in the as prepared samples. After this, the pellets were inserted in a tubular furnace, where they were exposed to a 100ml/min 5% H_2 + 95% He atmosphere and heated to 500 °C with a 10 °C/min heating rate. At 500 °C, the samples were treated under the 100ml/min 5% H_2 + 95% He atmosphere for 2 h. After, the CO_2 atmosphere was inserted leaving the sample exposed to 100ml/min 5% H_2 + 95% He + 25ml/min 20% CO_2 + 80% He atmosphere for 2 hr. At the end, the sample was cooled to RT under 200ml/min N_2. *In situ* time-resolved XANES measurements at the Cu K edge were performed every 1.5 min of exposure to the H_2 atmosphere, intending to characterize the mechanism related to the Cu reduction process. Moreover, *in situ* XANES and EXAFS measurements at the Cu and Ni K edges were also performed at the end of the H_2 and H_2+CO_2 treatments.

For the measurements at the DXAS beamline, Be windows separates the bending-magnets at the storage ring from a Rh-coated glass mirror. The incoming radiation from the ring is vertically focused, passes through a curved Si(111) crystal monochromator and reaches the sample holder where the X-rays transmitted through the sample are focused into a position-sensible CCD. Intending to investigate the reduction of the support by probing the Ce L_3 edge, at 5723 eV, pellets containing a mix of 7mg Cu_xNi_{1-x}/CeO_2 (x=0.25, 0.35, 0.60, 1.00) NPs powder and 35mg of BN were made. The pellets were inserted in a tubular furnace, where they were exposed to a 100ml/min 5% H_2 + 95% He atmosphere and heated to 500 °C with a 10 °C/min heating rate, while *in situ* XANES measurements were performed every 5 s. After 10 min at 500 °C in the H_2 atmosphere, the sample was cooled to RT under 200 ml/min N_2 atmosphere.

Besides the synthesized samples, standard compounds were measured and used for the XAS analysis. XANES measurements at XDS beamline were performed in standards of Cu(0), CuO, Cu_2O, $CuCl_2{\cdot}2H_2O$, Ni(0), NiO, $NiCl_2{\cdot}6H_2O$. The standards measured at the DXAS beamline corresponds to $CeOHCO_3$, and CeO_2.

All the *in situ* XANES measured data were initially treated in the *Athena* software, from the IFEFFIT package [138]. This treatment began with the calibration process, which allows the identification of chemical components during the analysis. In order to calibrate the photon energy, the corresponding Cu(0), Ni(0) and CeO_2 standards were used as reference. After the calibration process, the next step was the removal of spurious points from the measured data following the procedure described in [139, 140]. The last step in the data treatment before analysis is the data normalization. This normalization process was performed by regressing a straight line to the pre-edge region, and a quadratic polynomial function to the post-edge data, leaving the measured data "flattened". Then, the data were normalized in order to have the edge step equal to 1.

For the EXAFS data treatment, besides the procedure described above for the XANES data treatment, the theoretical contribution of single atom was extracted from the measured data in order to obtain the EXAFS oscillations. In this way, the measured *in situ* XANES and EXAFS data were ready to be analyzed by specific data treatment procedure of XANES and EXAFS spectra at the Ce L_3, Cu K or Ni K edge, described in the next sections.

4.3.3.1 *In situ* XANES measurements

In situ XANES measurements in transmission mode at the Cu K edge and Ni K edge were performed in the as prepared samples and at the end of each step of the gaseous treatment performed in order to identify the compounds present in the NPs. The Cu and Ni K edges measurements were fitted by a linear combination of the XANES measurements of standards. The standards used to fit the Cu K edge were Cu(0), CuO, Cu_2O, and $CuCl_2{\cdot}2H_2O$, while the Ni K edges were fitted using Ni(0), NiO, and $NiCl_2{\cdot}6H_2O$ standards.

Figure 4.3.7 shows a typical fit performed in the Cu K edge of the as prepared $Cu_{0.25}Ni_{0.75}/CeO_2$ NPs. The Cu K edge corresponds to an allowed transition from the 1s to 3p electronic state. As can be observed in the Figure 4.3.7, the Cu(0) standard has a small intensity after absorption edge, which is characteristic of filled electronic states at the 3p electronic level. On the other hand, the density of empty states increases on oxidized compounds, the electronic transition from the 1s to 3p electronic levels has higher probability to occur and the intensity after edge is consequently higher for CuO and $CuCl_2{\cdot}2H_2O$ compounds. Analogous interpretation can be applied to Ni(0), NiO and $NiCl_2{\cdot}6H_2O$ compounds. The percentage of each component found in the fit is presented schematically by the intensity of the standard XANES spectra used in the fit.

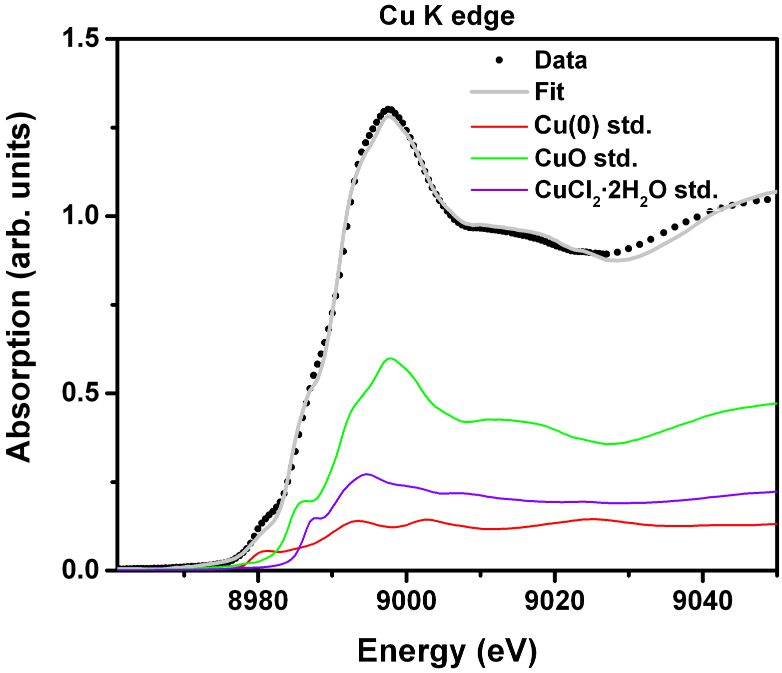

Figure 4.3.7 – XANES measurement at the Cu K edge of the as prepared $Cu_{0.25}Ni_{0.75}/CeO_2$ NPs. The measured data, standards used and resultant fit are presented.

For the Cu K edge measurements, the fit was performed between 20 eV before to 50 eV after the absorption edge, in the as prepared samples and after gaseous treatments. It allowed the identification of the chemical compounds present in each case. The results are presented in Table and 4.18. The $\mathcal{R}$-*factor* values lower than 0.005 shows the excellent quality of the fit performed, which is confirmed visually by the profile traced by the linear combination once compared to the measurement.

Table 4.18 – Analysis of the Cu compounds percentage in the samples for XAS measurements at the Cu K edge before and at the end of each gaseous treatment.

Treatment	Sample	Fractions (%)			
		Cu(0)	$CuCl_2{\cdot}2H_2O$	CuO	Cu_2O
As prepared	Cu NPs	0.0	9.3	90.7	0.0
	Cu/CeO_2 NPs	0.0	24.3	75.7	0.0
	$Cu_{0.60}Ni_{0.40}/CeO_2$ NPs	31.4	3.6	65.0	0.0
	$Cu_{0.35}Ni_{0.65}/CeO_2$ NPs	30.2	1.7	53.4	14.7
	$Cu_{0.25}Ni_{0.75}/CeO_2$ NPs	33.4	2.7	47.3	16.6
H_2 500 °C	Cu NPs	98.1	0.0	1.9	0.0
	Cu/CeO_2 NPs	100.0	0.0	0.0	0.0
	$Cu_{0.60}Ni_{0.40}/CeO_2$ NPs	100.0	0.0	0.0	0.0
	$Cu_{0.35}Ni_{0.65}/CeO_2$ NPs	100.0	0.0	0.0	0.0
	$Cu_{0.25}Ni_{0.75}/CeO_2$ NPs	100.0	0.0	0.0	0.0
H_2+CO_2 500 °C	Cu NPs	95.0	0.0	5.0	0.0
	Cu/CeO_2 NPs	100.0	0.0	0.0	0.0
	$Cu_{0.60}Ni_{0.40}/CeO_2$ NPs	100.0	0.0	0.0	0.0
	$Cu_{0.35}Ni_{0.65}/CeO_2$ NPs	100.0	0.0	0.0	0.0
	$Cu_{0.25}Ni_{0.75}/CeO_2$ NPs	100.0	0.0	0.0	0.0

The analysis at the Cu K edge, presented on Table 4.18, showed that CuO is the main compound existing in the as prepared NPs. It is also observed a relation between Cu concentration at the NPs and its oxide compounds: the percentages of Cu oxides are directly related to the amount of Cu in the NPs. The presence of the Cu_2O component is expected as an intermediary stage of reduction from CuO to Cu(0). The trend in the CuO behavior is also present in the conventional XPS measurements, though the absence of the Cu_2O compound. It occurs because in fact is hard to distinguish between Cu(0) and Cu_2O compounds in the XPS measurements of the as prepared samples due to the similarity between both Cu $2p_{3/2}$ peaks and the presence of other components (Cu-Cl, Cu-O) that gives a wide peak measured and makes the analysis difficult. Then, in fact, this result is consistent with the conventional XPS measurements but here is possible to see the presence of the Cu_2O component. The presence of the $CuCl_2 \cdot 2H_2O$ is also consistent with the conventional XPS data measurements.

The measured *in situ* XANES spectra at the Cu K edge during the thermal treatments (not shown here) presented a very similar shape to the typical *fingerprint* of metallic Cu, though smoothed due to thermal disorder. It is similar to Cu_2O XANES spectra as well. However, by comparing the derivative spectra of Cu(0) and Cu_2O standards it is possible to distinguish each case. By this comparison, it was possible to determine that the Cu_2O component does not appearsin the NPs after the H_2 exposition, as shown in the NAP-XPS measurements. Note that in this case, after gaseous treatment, the NAP-XPS measurements allows distinguishing between Cu(0) and Cu_2O due to the narrow and less complex peak existing in the Cu $2p_{3/2}$ region measurement.

Table 4.19 – Analysis of the Ni components percentage used to fit the XANES region at the Ni K edge measurements on the $Cu_xNi_{1\text{-}x}/CeO_2$ (x=0.25, 0.35, 0.60) NPs through gaseous treatments.

Treatment	Sample	Fractions (%)		
		Ni(0)	$NiCl_2 \cdot 6H_2O$	NiO
As prepared	$Cu_{0.60}Ni_{0.40}/CeO_2$ NPs	29.1	14.8	56.1
	$Cu_{0.35}Ni_{0.65}/CeO_2$ NPs	45.2	9.0	45.8
	$Cu_{0.25}Ni_{0.75}/CeO_2$ NPs	45.3	7.0	47.7
H_2, 500 °C	$Cu_{0.60}Ni_{0.40}/CeO_2$ NPs	95.4	0.0	4.6
	$Cu_{0.35}Ni_{0.65}/CeO_2$ NPs	96.0	0.0	4.0
	$Cu_{0.25}Ni_{0.75}/CeO_2$ NPs	96.8	0.0	3.2
H_2+CO_2, 500 °C	$Cu_{0.60}Ni_{0.40}/CeO_2$ NPs	96.0	0.0	4.0
	$Cu_{0.35}Ni_{0.65}/CeO_2$ NPs	96.0	0.0	4.0
	$Cu_{0.25}Ni_{0.75}/CeO_2$ NPs	96.9	0.0	3.1

Table 4.19 shows the fitting results for the $Cu_xNi_{1\text{-}x}/CeO_2$ (x=0.25, 0.35, 0.60) NPs in the as prepared case and after each gaseous treatment employed. It is shown that the main component of as prepared samples is related to NiO, which is consistent to the XPS data (Table 4.4). The NiO fraction obtained in the XANES measurements is lower (around 50%) than those obtained in XPS analysis (around 70%), which shows the NiO component has a stronger contribution at the surface region. It is consistent to the oxidation of the Ni atoms due to the air exposition after synthesis. Moreover, the

comparison between results from XPS and XANES measurements shows that the Ni(0) component is evidenced to be at the NPs inner region. A similar comparison can be done for the Ni-Cl components, that are concentrated at the surface region since its intensity is high on the XPS measurements (surface sensitive) and low on the XANES measurements (bulk sensitive). Further, the analysis of the components after the H_2 treatment showed the strong reduction of the Ni compounds, also consistent with the surface results presented in the NAP-XPS measurements in which the NPs containing more Ni atoms are also the most reduced ones. It is also observed that during thermal treatments, the Ni-Cl components no longer presents relevant contributions to the absorption measurements while the oxide component keeps its collaborations (mostly at the surface). Moreover, the exposition to the RWGS reaction atmosphere did not promoted effective oxidation on the NPs, as shown in the NAP-XPS analysis.

In order to elucidate the Cu and Ce reduction kinetics for the NPs, *in situ* time-resolved XANES measurements were performed at the Cu K edge (XDS beamline) and Ce L_3 edge (DXAS beamline).

4.3.3.2 *In situ* time-resolved XANES measurements

In order to elucidate the Cu behavior during the H_2 reduction treatment, *in situ* XANES measurements at the Cu K edge were taken every 1.5 min during the H_2 reduction treatment from RT to 500 °C. Figure 4.3.8 shows the typical *in situ* time-resolved XANES data at the Cu K edge of the Cu/CeO_2 NPs measured during the H_2 reduction treatment. It is possible to see clearly the decrease in the intensity after edge with the increase of the temperature, which is an indicative of the decrease on the number of electronic empty states at the Cu 3p electronic level. It is consistent with the reduction of the sample from Cu(II) to Cu(0) oxidation state. Moreover, the reduction treatment gives a shift of the binding energy to smaller values, characteristic of the reduction behavior of the sample.

The spectra analysis was performed for selected XANES spectra, namely every 5 min of reduction treatment. A linear combination of Cu(0), $CuCl_2{\cdot}2H_2O$, CuO, and Cu_2O standards was used to fit these measured spectra. This analysis resulted in a time-evolution study of compound fractions from the as prepared state to the reduced state presented at the end of the H_2 reduction treatment. The fit of the selected *in situ* XANES measurements at Cu K edge allowed obtaining the time evolution of each compounds fraction. It is presented in Figure 4.3.9.

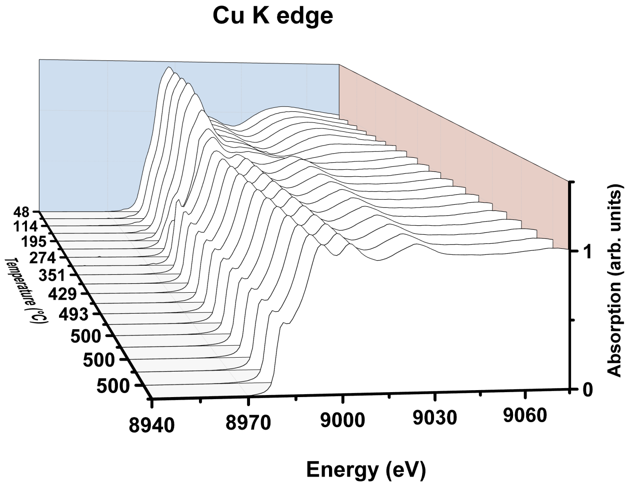

Figure 4.3.8 – Time-evolution of the XANES spectra at the Cu K edge of the Cu/CeO_2 NPs during the H_2 treatment.

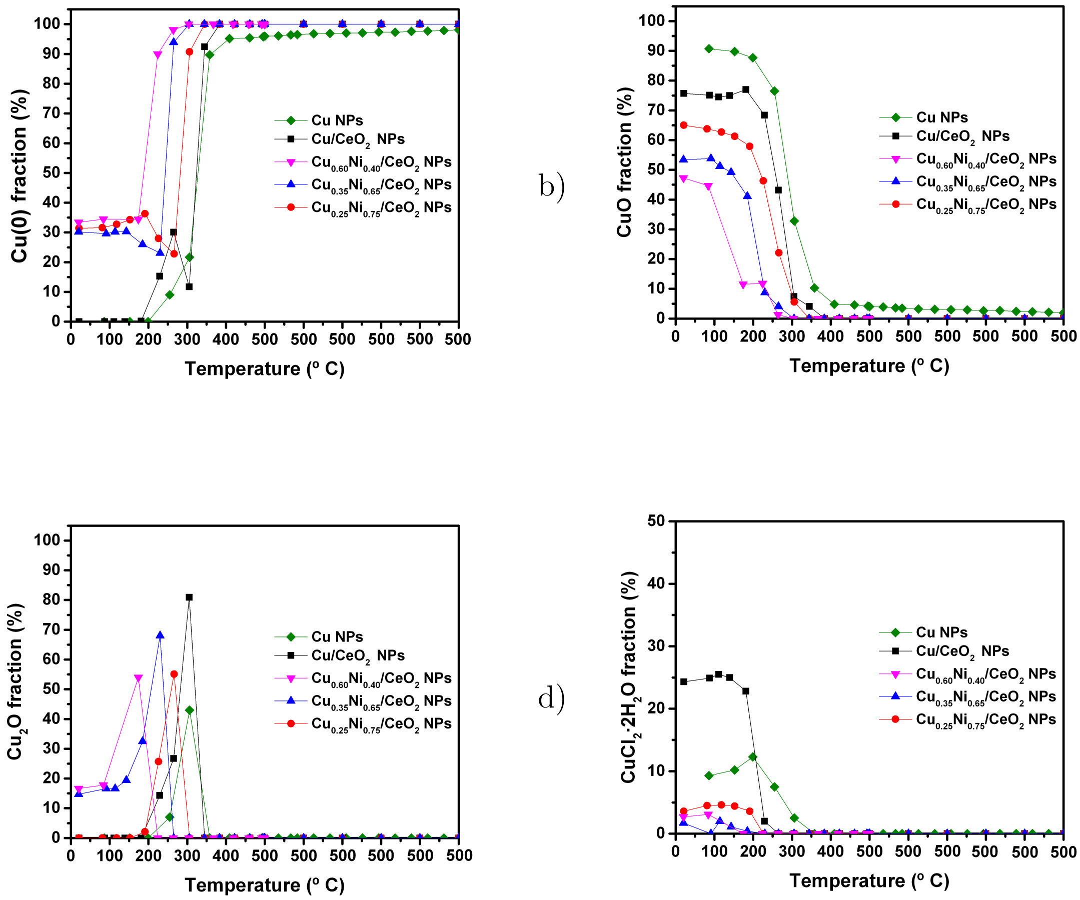

a) b) c) d)

Figure 4.3.9 – Time-evolution of the a) Cu(0), b) CuO, c) Cu_2O, and d) $CuCl_2 \cdot 2H_2O$ fractions obtained by a linear combination analysis in the XANES region at the Cu K edges of the $Cu_xNi_{1\text{-}x}/CeO_2$ (x=0.25, 0.35, 0.60, 1.00) and non-supported Cu NPs during the H_2 reduction treatment.

During the fitting procedure of the XANES region at the Cu K edge, it was noticed that even after half hour at the 500 °C H_2 reduction treatment a high fraction of Cu_2O was accused in the linear combination results. Furthermore, the observed *fingerprint* at the Cu K edge evolved to a smoothed Cu(0) shape at high temperatures ($T > 300$ °C). The analysis of the first derivative on the measured spectra indicated that after a given temperature, for distinct samples, the pattern observed matched the metallic component in energy and shape though with intensity smoothed. On the other hand, the same analysis of the first derivative on the measured spectra for the Cu_2O component showed oscillations out of phase and with a poor agreement between standard and measured data. This feature allowed the Cu_2O standard removal from the linear combination from this point on, matching its absence observed in the NAP-XPS measurements at surface and inner regions of the NPs. The temperature corresponding to this removal procedure is evidenced by a sudden drop to zero in the Cu_2O fraction graph presented in Figure 4.3.9, inducing a "break" in the evolution trend observed for the other compounds fractions of the fitted samples (more evident in the Cu(0) fraction graph).

It is noticed that the $Cu_{0.60}Ni_{0.40}/CeO_2$ sample is the first bimetallic sample that starts to reduce. The reduction temperature in this case is as low as 200 °C, in comparison to the smaller Cu concentration case, that is around 300 °C. It shows the reduction temperature of Cu atoms is inversely related to the Cu concentration of the bimetallic NPs. However, the same trend cannot be established for the monometallic case that presents the higher reduction temperature between samples even with 100% of Cu atoms. In fact, the Cu/CeO_2 NPs present a smaller reduction temperature than the non-supported Cu monometallic case. It is interesting to note that both samples presenting the SMSI effect (Cu/CeO_2 and $Cu_{0.60}Ni_{0.40}/CeO_2$) have lower reduction temperature in comparison to similar samples without the SMSI effect occurrence. It may be an indicative of the electronic factor of the SMSI effect that occurs for low temperatures [58] and typically with a charge transfer from the support to the NPs, then helping on the reduction process [60]. Analogous conclusion was obtained in previous work for Ni/CeO_2 and Cu/CeO_2 monometallic NPs [60] where the Cu NPs reduced at around 300 °C, in accordance to the results found in this work. Another possibility is the reduction of the NPs induced by the cerium oxide capping layer surrounding the NPs. In this case, the cerium oxide would present a small oxidation during the reduction process. It is important to stress out also that the initial Cu(0) fraction is the same between bimetallic NPs, then it is not influencing on this result. On the other hand, the smaller is the initial CuO fraction the smaller is the reduction temperature, showing that the CuO fraction is an important factor to be considered too. Based on the Cu reduction process described as follows, the small amounts of CuO fraction also helps on an earlier reduction of Cu atoms.

From the analysis of the graphs presented in Figure 4.3.9 is possible to deduce the steps of the Cu reduction. This behavior, common to every sample, can be summarized as $CuO \rightarrow Cu_2O \rightarrow Cu(0)$, or, ir more details

(i) Cleavage of oxygen bonds starts at different temperatures (depending on the sample), decreasing the CuO fractions while turning it into Cu_2O

(ii) Cl atoms start to leave the NPs around 200 °C

(iii) The Cu_2O fraction starts to decrease, being converted to Cu(0) at different temperatures (depending on the sample).

(iv) Samples present a metallic component with essentially no oxide fractions

Reduction mechanisms for the CuO component have been reported and the CuO $\rightarrow Cu_2O \rightarrow Cu(0)$ reaction path is well established for Cu reduction [141, 142].

Figure 4.3.10 shows a typical XANES spectrum at the Ce L_3 edge of $Cu_{0.25}Ni_{0.75}/CeO_2$ NPs exposed to H_2 atmosphere at 60 °C. The Ce L_3 edge corresponds to an electronic transition from the 2p to 5d electronic level. The double peak after absorption edge is characteristic of Ce(IV) oxidation state and the case of a single peak is characteristic of Ce(III) oxidation state. The XANES spectra were analyzed applying an analytical method based on combinations of arctangent and Lorentzian functions as described in the literature [143]. The arctangent function describes an electronic transition from the 2p electronic level to continuum. One of the Lorentzian functions is associated to the Ce(III) oxidation state and corresponds to an electronic transition from the $2p_{3/2}$ to $4f^1 5d$ electronic state. The other two Lorentzian functions are associated to Ce(IV) oxidation state and corresponds to the $2p_{3/2} \rightarrow 4f^L 5d$ and $4f^0 5d$ transitions, where "L" denotes that an electron in 2p orbital of oxygen is transferred to 4f orbital of Ce [143]. The energy range used in the fitting includes the single and double peak characteristic of the Ce(III) and Ce(IV) compounds, respectively. Initially, the XANES spectrum of the Ce(IV) standard (CeO_2) was fitted using one arctangent and two Lorentzian functions. This fitting was performed without any constraints in the parameters of the functions used (width and position). After this, the spectrum of the Ce(III) standard ($CeOHCO_3$) was fitted using one arctangent and one Lorentzian function. In this way, it was possible to obtain the parameters (width and position) of the Lorentzian and arctangent functions for the Ce(IV) and Ce(III) standards that were then used as fixed parameters in the fitting of the *in situ* XANES spectra of the samples.

In equation 4.2, the right-side subscripts identify the oxidation state of the Ce component fitted. Parameters associated to the arctangent functions are A_{III}, A'_{IV} and A''_{IV} to describe their amplitudes; B_{III}, B'_{IV} and B''_{IV} to describe their concavities; and

C_{III}, C'_{IV} and C''_{IV} to describe the energy positions. The Lorentzian functions are determined by the parameters D_{III}, D'_{IV} and D''_{IV} to describe their heights; E_{III}, E'_{IV} and E''_{IV} to describe their widths ; and F_{III}, F'_{IV} and F''_{IV} to describe the energy positions. The π factor multiplying the arctangent functions was used to account for the previous normalization process in the data. These parameters, obtained from the standards analysis, are presented on Table 4.20.

$$\begin{aligned} f(x) = \pi \cdot \frac{A_{III}}{2} + A_{III} \cdot arctan(B_{III} \cdot (x - C_{III})) + \frac{D_{III} \cdot E_{III}^2}{(x - F_{III})^2 + E_{III}^2} \\ + \pi \cdot \frac{A'_{IV}}{2} + A'_{IV} \cdot arctan(B'_{IV} \cdot (x - C'_{IV}) + \frac{D'_{IV} \cdot {E'_{IV}}^2}{(x - F'_{IV})^2 + {E'_{IV}}^2} + \\ + \pi \cdot \frac{A''_{IV}}{2} + A''_{IV} \cdot arctan(B''_{IV} \cdot (x - C''_{IV})) + \frac{D''_{IV} \cdot {E''_{IV}}^2}{(x - F''_{IV})^2 + {E''_{IV}}^2} \end{aligned} \tag{4.2}$$

The amplitude values of the arctangent functions related to the Ce(IV) converged to zero in every fit through the different gaseous treatments, therefore only one arctangent function (A_{III}) was used in the fitting procedure of the XANES spectra of the samples. An example of this fits is presented on Figure 4.3.10, with the respective Lorentzians and arctangent functions used.

Table 4.20 – Parameters determined in the $CeOHCO_3$ (Ce(III)) and CeO_2 (Ce(IV)) standards fits. The parameters associated to the amplitude of the Lorentzian and arctangent functions are not presented because these are the fitted parameters in the samples spectra.

Ce component	Parameter	Value
Ce(III)	B_{III}	0.41
	C_{III}	5723.80
	E_{III}	4.35
	F_{III}	5725.87
Ce(IV)	B'_{IV}	0.74
	C'_{IV}	5724.34
	E'_{IV}	4.01
	F'_{IV}	5730.74
	B''_{IV}	0.01
	C''_{IV}	5733.08
	E''_{IV}	5.04
	F''_{IV}	5739.11

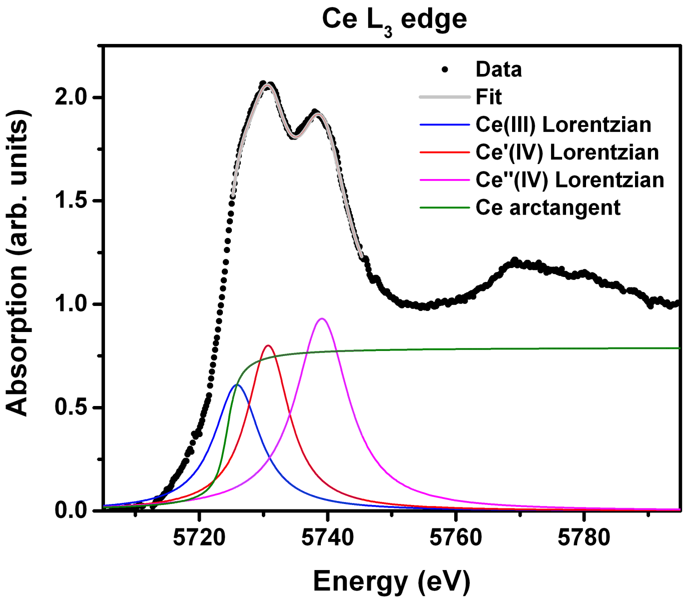

Figure 4.3.10 – Typical *in situ* XANES measurement at the Ce L_3 edge and the correspondent fit for the $Cu_{0.25}Ni_{0.75}/CeO_2$ NPs at 65 °C in the H_2 atmosphere. The arctangent and Lorentzian functions used to fit the spectrum are highlighted and identified.

The time-evolution of the Ce(III) components during the H_2 treatment was obtained fitting spectra for every 5 min of reduction treatment. From the intensities determined by these fits, the Ce(III) fraction was calculated. This fraction was determined using the area of the Lorentzian function fitted, using the equation

$$\%Ce(III) = \frac{B_{III} \cdot E_{III}}{B_{III} \cdot E_{III} + B'_{IV} \cdot E'_{IV} + B''_{IV} \cdot E''_{IV}} \tag{4.3}$$

Figure 4.3.11 shows a comparison between the Ce(III) fraction time evolution for different samples, where is possible to observe that the support presents a different kinetics of reduction depending on the sample.

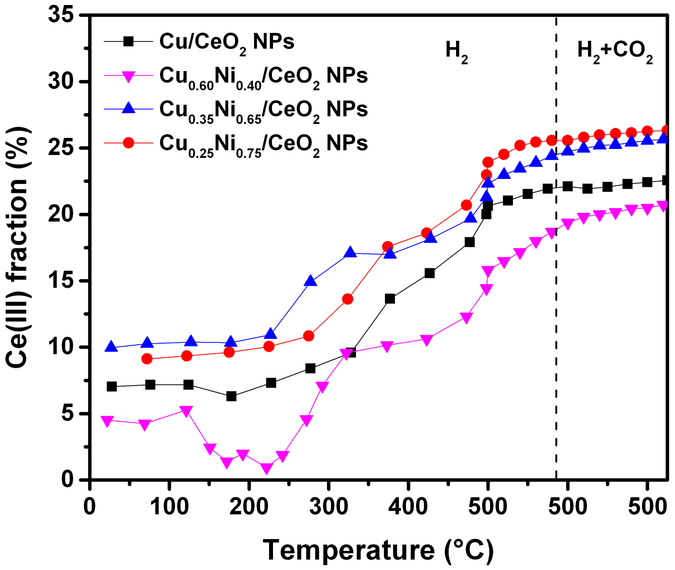

Figure 4.3.11 – Time-evolution of the Ce(III) fraction obtained from the analysis of the *in situ* XANES spectra during the H_2 treatment from RT to 500 °C for the $Cu_xNi_{1\text{-}x}/CeO_2$ (x = 0.25, 0.35, 0.60, 1.00) NPs.

It is possible to observe in Figure 4.3.11 that the less reduced samples at the end of the reduction treatment at 500 °C are those previously related to the SMSI effect, Cu/CeO_2 and $Cu_{0.60}Ni_{0.40}/CeO_2$ NPs. It supports the idea of strong interaction between the capping layer and the surface of NPs. In fact, it can be used to explain the shift in the reduction temperature of Cu observed for these NPs in comparison to those without the SMSI effect (Figure 4.3.9). The capping layer may act as a reducing agent of Cu and Ni atoms, then being oxidized. It is also observed a "two-stage" reduction process for all the samples, where the first stage is observed starting between T=250 °C and T=350 °C, and the second stage starting around T=400 °C. At the best of our knowledge, this behavior was not reported yet and represents an important information on the reduction kinetics of cerium oxide support. In the previous work [60] where Cu/CeO_2 and Ni/CeO_2 NPs were exposed to the same H_2 reduction treatment, there is no evidence for two stages in the reduction process of cerium oxide support. The reasons for the difference found will be subject of a further detailed work.

It is interesting to note that there is a period between 150 °C and 250 °C where the Ce(III) fraction of $Cu_{0.60}Ni_{0.40}/CeO_2$ and Cu/CeO_2 NPs decreases even with the sample exposed to the H_2 reduction atmosphere. It is more evident for the $Cu_{0.60}Ni_{0.40}/CeO_2$ NPs than for the Cu/CeO_2 ones. This oxidation phenomena may evidence the oxygen donation process from the NPs to the capping layer surrounding it, as proposed earlier. Note that the temperature of this oxidation phenomenon of the cerium oxide supports matches perfectly to the temperature of the Cu reduction (Figure 4.3.9), then giving a stronger evidence that the Cu reduction of $Cu_{0.60}Ni_{0.40}/CeO_2$ and Cu/CeO_2 NPs is induced by the cerium oxide capping layer surrounding the NPs. Considering this, it is possible to identify the exact time where the geometrical factor of the SMSI effect occurs. Thereby, these data shows, for the first time, evidence for the beginning of the geometrical factor of the SMSI effect and gives an interesting method to identify the SMSI effect based on this fingerprint in the time evolution of the Ce(III) fraction.

4.3.3.3 *In situ* EXAFS measurements

In situ EXAFS measurements were performed at the Cu K edge and Ni K edge of $Cu_xNi_{1\text{-}x}/CeO_2$ (x = 0.25, 0.35, 0.60, 1.00) NPs and non-supported Cu NPs at the end of the reduction treatment and RWGS reaction aiming the characterization of the neighborhood of the absorbing Cu and Ni atoms. In order to perform this characterization, the EXAFS oscillations were extracted from the XAS data measured. Fourier Transforms were performed on the k^2-weighted $\chi(k)$ EXAFS oscillations using a Kaiser-Bessel window [140], with a *k space* interval of Δ=8.3 Å^{-1} for the Cu K edge measurements. For the Ni K edge, the FT were obtained from the k^2-weighted $\chi(k)$ EXAFS oscillations and the interval used was Δ=8.0 Å^{-1}. The data was analyzed by the Artemis software (also from IFEFFIT package [138]). In the Artemis software, the EXAFS oscillations, $\chi(k)$, were fitted using multiple-scattering paths from a theoretical calculation previously performed using the FEFF6L code [144].

FEFF is an *ab initio* multiple-scattering code for calculating the X-ray absorption fine structure for clusters of atoms. It is based on a real space Green's function approach including a screened core-hole, inelastic losses, self-energy shifts, and Debye-Waller factors. To determine the scattering paths, a file containing information of the crystalline structure of the system (lattice parameters, space group and atomic positions) is used as the input data. Then, the code sequentially (i) calculates the scattering potentials, phase-shifts, dipole matrix elements and absolute energies; (ii) enumerates the scattering paths for the cluster; (iii) calculates the effective scattering amplitudes (and other XAS parameters) for each path; (iv) combines scattering paths and calculates the total XAS spectrum. Once the multiple-scattering path expansion is imported, the measured oscillations can be fitted. For each path included in the fit, the EXAFS equation parameters associated to coordination number N_s, Debye-Waller factor σ^2_{as}, absorption edge position E_0, and absorber-scatterer distance ΔR_{as} are evaluated.

Cu and Ni clusters of 10 Å radius, generated by their ccp crystal structures (atoms arranged in a Fm-3m space group presenting lattice parameters of 3.615 Å (Cu) and 3.524 Å (Ni)) were used to calculate the phase-shifts and scattering amplitudes. The calculated single and multiple-scattering paths were used to fit up to the fourth coordination shell of the FTs obtained from the $\chi(k)$ measured in the Cu(0) and Ni(0) standards, determining the S_0^2 factor values of 0.88 and 0.99 for the Cu and Ni absorbing atoms, respectively. The FT of the EXAFS oscillations of the NPs were adjusted using these amplitude reduction factors obtained from the standard analysis. The fitting was performed only in the coordination shell around Cu and Ni atoms. Two cumulants [140] were included in the fittings, in which they presented typical values of 10^{-4}. It was also used a background spline to fit the FTs. The fits were performed in the *R space* using paths computed for monometallic clusters (Cu or Ni) even for the bimetallic NPs since the technique is not sensitive enough to distinguish atoms with close atomic numbers. In this way, the data were analyzed in terms of metallic scatterers *M* (Cu or Ni) around the absorbing atom. The paths provided from the calculation of these monometallic clusters did not accounted for light scatterers, so additional calculations were performed using the crystal structures of CuO and NiO crystals. These calculations were also imported to fit the FT of the EXAFS oscillations at Cu and Ni K edge.

Figures 4.3.12 to 4.3.15 show a comparison between the EXAFS oscillations and the corresponding FT at the Cu K edge and Ni K edge for different gaseous treatments and the standard case. By comparing the EXAFS oscillations measured after reduction treatment and RWGS reaction to the metallic standards, it is noticed a very similar pattern of oscillations, though damped. The damping effect was expected by the higher atomic disorder at higher temperatures, increasing the destructive superpositions of the scattered waves in the sample. It is possible to observe also a high similarity between the EXAFS oscillations of the sample after reduction treatment and RWGS reaction at 500 °C. It is expected since the previous characterizations showed no significant Cu and Ni oxidation effect during RWGS reaction.

The FT of the EXAFS oscillations at the Cu K edge and Ni K edge shows the presence of a single important contribution at the coordination shell corresponding to Cu-M and Ni-M scattering (M = Cu or Ni), respectively. The peaks associated to the second shell and so on are small in intensity due to the thermal disorder associated to the temperature of 500 °C during the measurements. It is important to observe a small contribution at $R \approx 1.5$ Å (not phase corrected) which can be associated to Cu-O or Ni-O scattering paths. However, the same contribution is observed in the FT of the EXAFS oscillations of standard samples(in this case showing that it is not due to Cu-O and Ni-O scatterings, for sure), and then, the Cu-O and Ni-O scattering could be discarded. Even considering this, it was observed the need of including a Cu-O and Ni-O scattering path in order to have a good fit quality in this region for the data associated to the NPs measured, differently to the standard case.

Tables 4.21 to 4.25 shows the parameters obtained from the fitting procedure in comparison to those obtained for the standard sample. The $\mathcal{R}$-*factor* obtained in the fits presented values always lower than 0.03, showing the good quality of the fits.

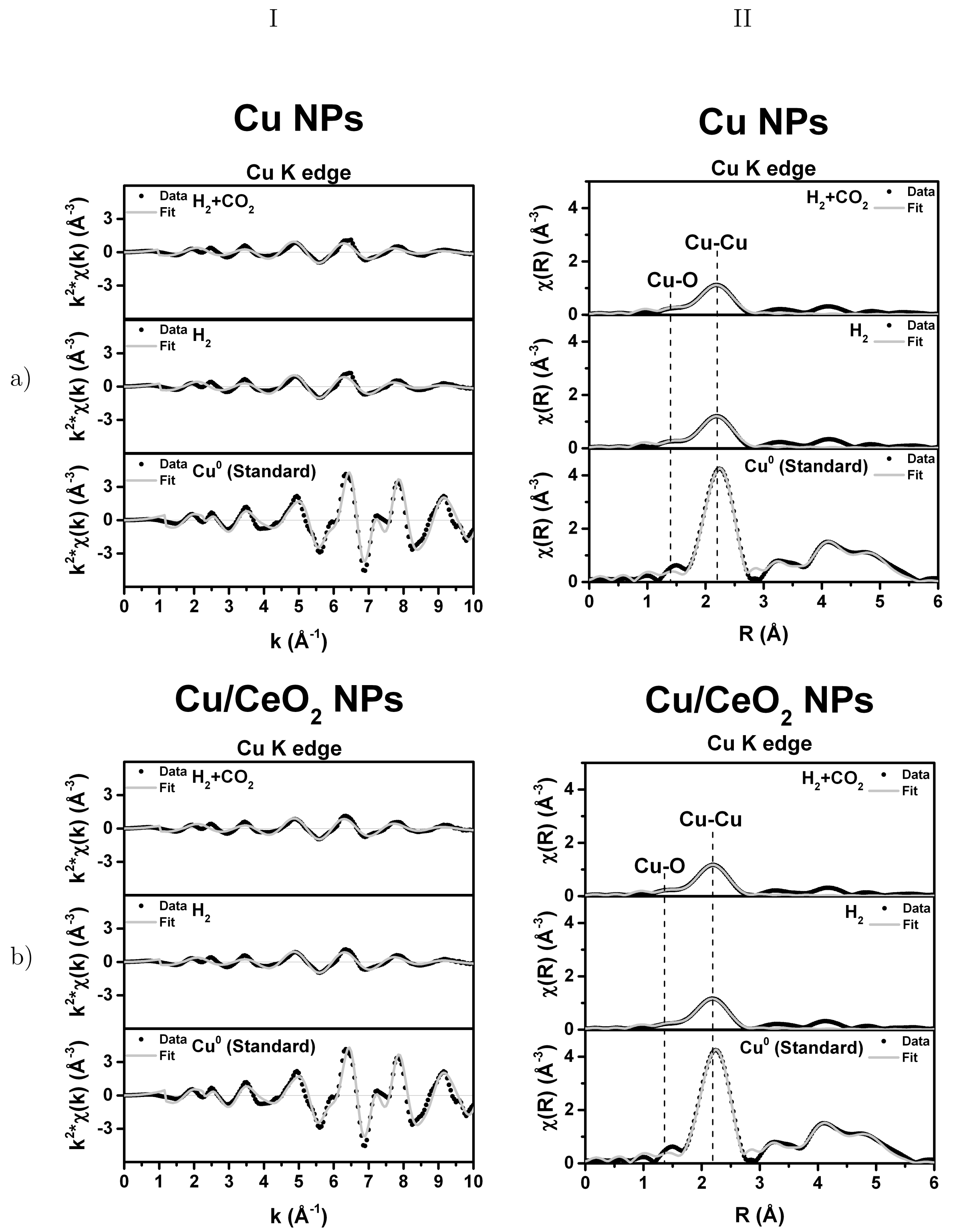

Figure 4.3.12 – EXAFS oscillations I), and the corresponding FTs II) of a) Cu NPs, and b) Cu/CeO$_2$ NPs, measured at the Cu K edge during H$_2$ reduction treatment and RWGS reaction at 500 °C. Scattering contributions are identified in the graphs. The data is presented without the phase-shift correction.

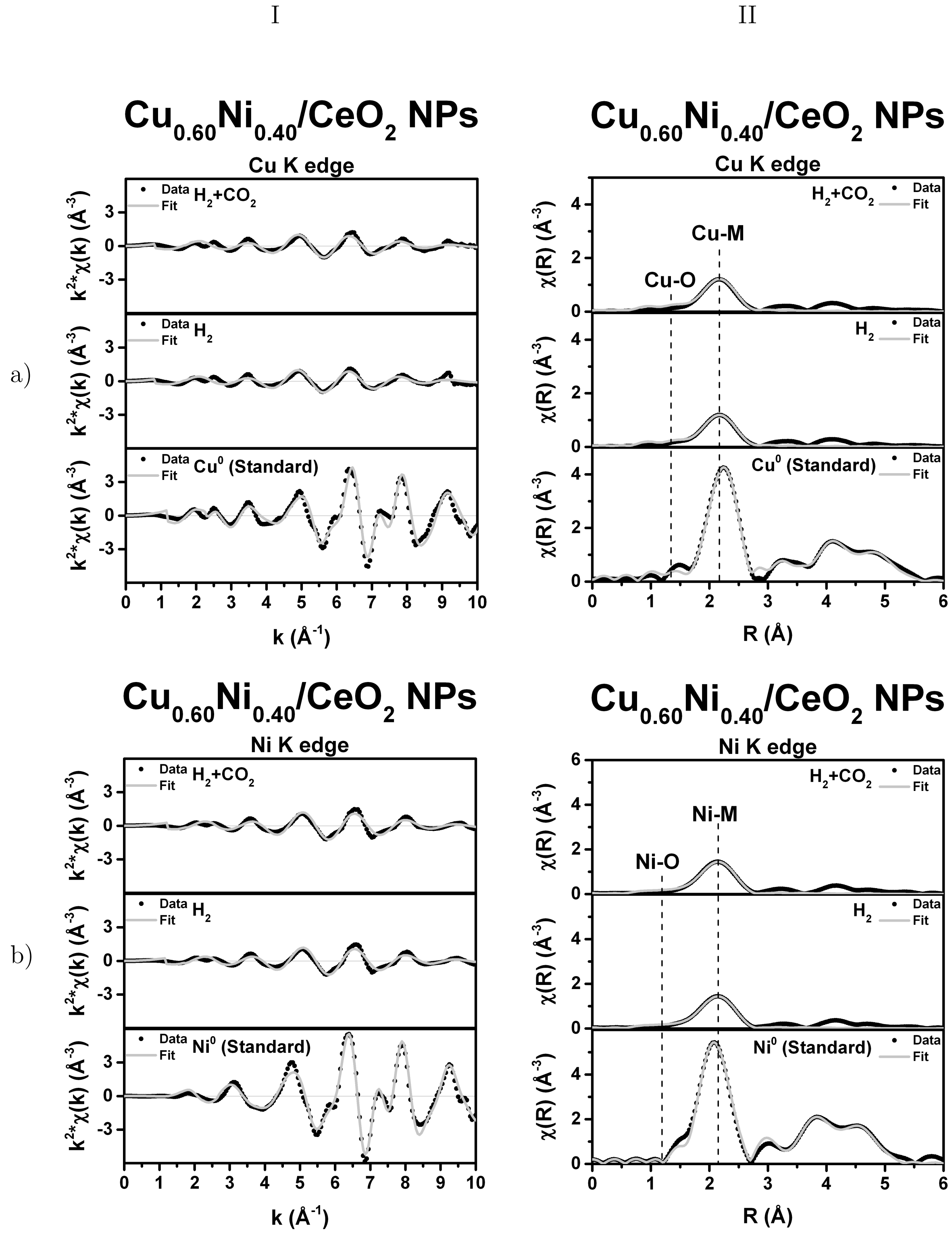

Figure 4.3.13 – EXAFS oscillations I), and the corresponding FTs II) of $Cu_{0.60}Ni_{0.40}/CeO_2$ NPs measured at the a) Cu K edge, and b) Ni K edge, during H_2 reduction treatment and RWGS reaction at 500 °C. Scattering contributions are identified in the graphs, where M indicates the metallic neighbor. The data is presented without the phase-shift correction.

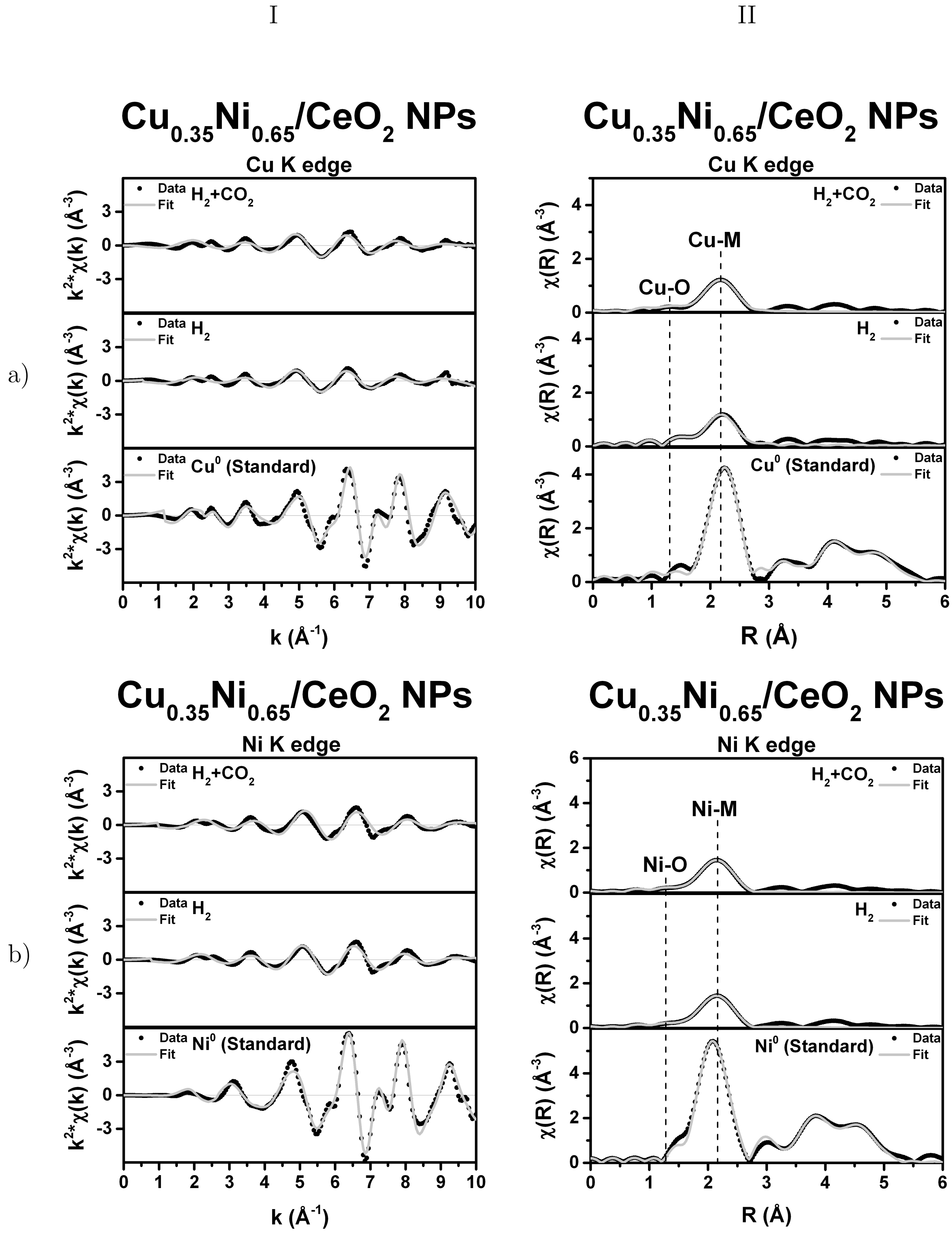

Figure 4.3.14 – EXAFS oscillations I), and the corresponding FTs II) of $Cu_{0.35}Ni_{0.65}/CeO_2$ NPs measured at the a) Cu K edge, and b) Ni K edge, during H_2 reduction treatment and RWGS reaction at 500 °C. Scattering contributions are identified in the graphs, where M indicates the metallic neighbor. The data is presented without the phase-shift correction.

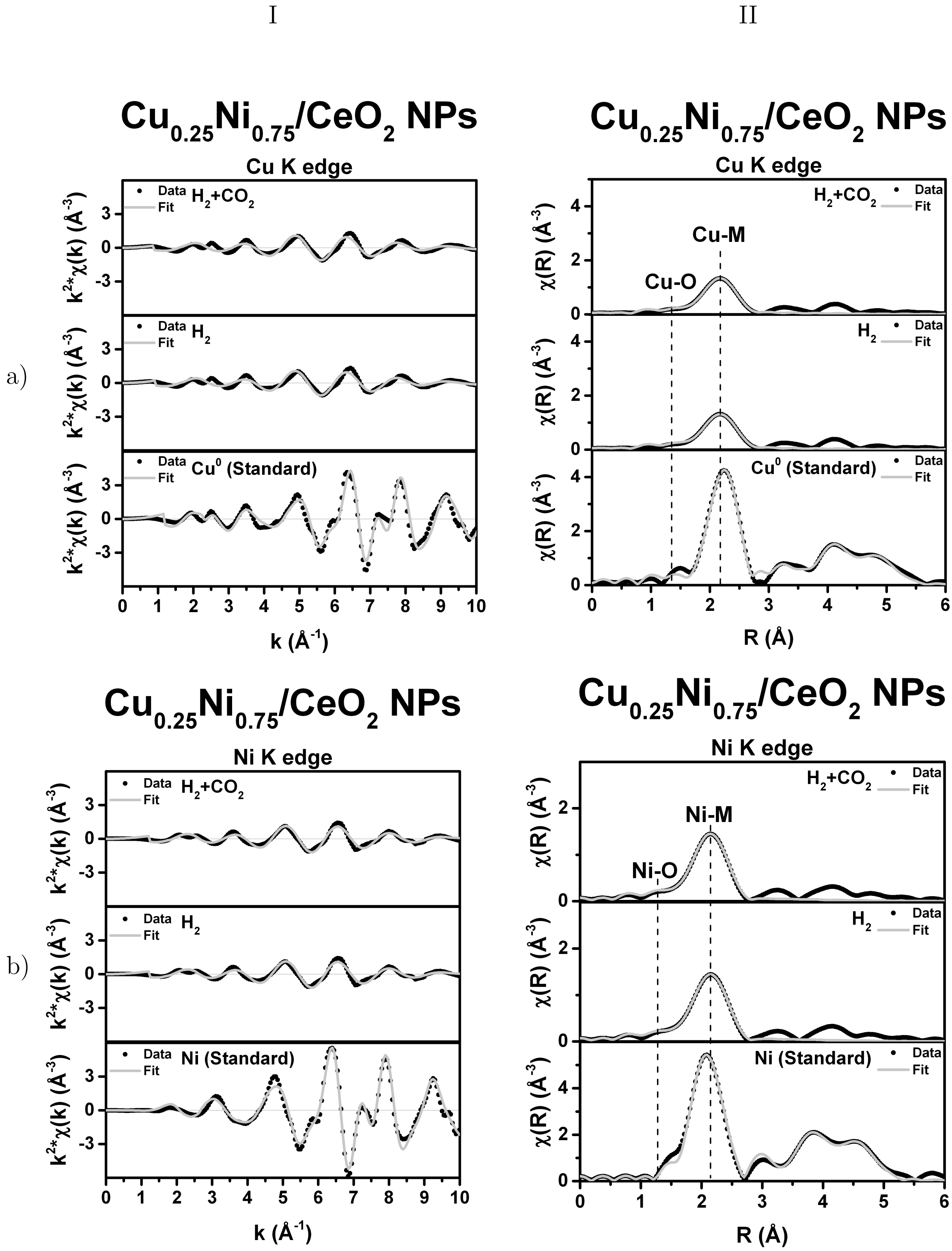

Figure 4.3.15 – EXAFS oscillations I), and the corresponding FTs II) of $Cu_{0.25}Ni_{0.75}/CeO_2$ NPs measured at the a) Cu K edge, and b) Ni K edge, during H_2 reduction treatment and RWGS reaction at 500 °C. Scattering contributions are identified in the graphs, where M indicates the metallic neighbor. The data is presented without the phase-shift correction.

Table 4.21 – Parameters determined in the quantitative analysis of the FTs of the EXAFS oscillations for the Cu NPs measured at the Cu K edge during H_2 reduction treatment and RWGS reaction at 500 °C.

Atmosphere	Path	R_{as} (Å)	N_s	σ^2_{as} (10^{-2} Å^2)
H_2	Cu-Cu	2.559 ± 0.003	11 ± 1	1.4 ± 0.1
	Cu-O	2.4 ± 0.5	1 ± 1	1.8 ± 0.8
H_2+CO_2	Cu-Cu	2.559 ± 0.003	10 ± 1	1.4 ± 0.1
	Cu-O	2.4 ± 0.05	1 ± 1	1.8 ± 0.8

Table 4.22 – Parameters determined in the quantitative analysis of the FTs of the EXAFS oscillations for the Cu/CeO_2 NPs measured at the Cu K edge during H_2 reduction treatment and RWGS reaction at 500 °C.

Atmosphere	Path	R_{as} (Å)	N_s	σ^2_{as} (10^{-2} Å^2)
H_2	Cu-Cu	2.557 ± 0.001	9.5 ± 0.7	1.3 ± 0.6
	Cu-O	2.4 ± 0.5	1.0 ± 0.9	1.7 ± 0.3
H_2+CO_2	Cu-Cu	2.562 ± 0.006	9.5 ± 0.8	1.3 ± 0.6
	Cu-O	2.4 ± 0.05	1.0 ± 0.8	1.7 ± 0.3

Table 4.23 – Parameters determined in the quantitative analysis of the FTs of the EXAFS oscillations for the $Cu_{0.60}Ni_{0.40}$/CeO_2 NPs measured at the Cu K edge and Ni K edge during H_2 reduction treatment and RWGS reaction at 500 °C.

Atmosphere	Path	R_{as} (Å)	N_s	σ^2_{as} (10^{-2} Å^2)
H_2	Cu-M	2.53 ± 0.03	10 ± 1	1.36 ± 0.06
	Cu-O	2.4 ± 0.5	0.9 ± 0.9	1.8 ± 0.9
	Ni-M	2.48 ± 0.01	7.5 ± 0.9	0.92 ± 0.07
	Ni-O	2.12 ± 0.04	0.4 ± 0.4	1.7 ± 0.8
H_2+CO_2	Cu-M	2.52 ± 0.04	10.7 ± 0.9	1.36 ± 0.06
	Cu-O	2.4 ± 0.5	0.7 ± 0.7	1.8 ± 0.9
	Ni-M	2.483 ± 0.008	7.6 ± 0.9	0.92 ± 0.07
	Ni-O	2.12 ± 0.04	0.3 ± 0.3	1.7 ± 0.8

Table 4.24 – Parameters determined in the quantitative analysis on the FTs of the EXAFS oscillations from the $Cu_{0.35}Ni_{0.65}/CeO_2$ NPs measured at the Cu K edge and Ni K edge during H_2 reduction treatment and RWGS reaction at 500 °C.

Atmosphere	Path	R_{as} (Å)	N_s	σ^2_{as} (10^{-2} Å^2)
H_2	Cu-M	2.49 ± 0.07	10 ± 2	1.3 ± 0.2
	Cu-O	2.4 ± 0.5	1 ± 1	1.7 ± 0.9
	Ni-M	2.44 ± 0.06	7.9 ± 0.6	0.9 ± 0.2
	Ni-O	2.00 ± 0.08	0.6 ± 0.4	1.7 ± 0.5
H_2+CO_2	Cu-M	2.48 ± 0.08	11 ± 2	1.3 ± 0.2
	Cu-O	2.4 ± 0.5	0 ± 1	1.7 ± 0.9
	Ni-M	2.42 ± 0.08	7.5 ± 0.7	0.9 ± 0.2
	Ni-O	2.0 ± 0.1	0.7 ± 0.5	1.7 ± 0.5

Table 4.25 – Parameters determined in the quantitative analysis on the FTs of the EXAFS oscillations from the $Cu_{0.25}Ni_{0.75}/CeO_2$ NPs measured at the Cu K edge and Ni K edge during H_2 reduction treatment and RWGS reaction at 500 °C.

Atmosphere	Path	R_{as} (Å)	N_s	σ^2_{as} (10^{-2} Å^2)
H_2	Cu-M	2.54 ± 0.05	11.1 ± 0.8	1.33 ± 0.01
	Cu-O	2.4 ± 0.5	1 ± 1	1.9 ± 0.2
	Ni-M	2.486 ± 0.006	7.2 ± 0.8	0.88 ± 0.01
	Ni-O	2.12 ± 0.03	0.4 ± 0.4	1.6 ± 0.9
H_2+CO_2	Cu-M	2.54 ± 0.02	11.2 ± 0.8	1.33 ± 0.07
	Cu-O	2.4 ± 0.4	2 ± 2	1.9 ± 0.9
	Ni-M	2.486 ± 0.009	7.2 ± 0.8	0.88 ± 0.08
	Ni-O	2.12 ± 0.03	0.4 ± 0.4	1.6 ± 0.9

The monometallic samples present constant values for the Cu-M distance, not dependent on the atmospheric treatment, and slightly bigger than that obtained for the first coordination shell of the Cu standard (2.53 A). The reason is associated to the thermal expansion existing since the monometallic NPs were measured at 500 °C and the standard sample was measured at RT. On the other hand, bimetallic NPs present the same or smaller Cu-M distance than the distance found for the Cu-Cu standard. The reason may be associated to the presence of Ni atoms that induces a change on the Cu-M length. Similar effect is observed for the Ni K edge since the Ni-Ni distance at the coordination shell obtained from the fit of Ni standard is 2.48 Å. The non-supported NPs present higher Cu-M coordination numbers ($N_{Cu\text{-}M}$) than the supported NPs, though both of them shows lower values than the Cu standard ($N_{\text{Cu-Cu}} = 12$). An explanation relies on a possible agglomeration of the non-supported Cu NPs since it is known that CeO_2 support acts avoiding agglomeration of metallic NPs [145]. Moreover, it is not observed a significant change on the Cu-M coordination number with the change of gaseous atmosphere for a given sample. Similar conclusion can be obtained for the measurements at the Ni K edge and the Ni-M coordination numbers. It is important to note that for a given sample, for all the cases, the Ni-M coordination number is always smaller than the Cu-M coordination number. It is explained due to the presence of a significant Ni-O contribution in this case, in opposition to the Cu-O contribution that is not important as observed in the NAP-XPS measurements (Table 4.7 and 4.9).

The Debye-Waller factor of the Cu-M scattering is always bigger than the Debye-Waller factor of the Cu-Cu scattering at the Cu standard sample ($0.7 \cdot 10^{-2}$ Å^2). It is associated to the bigger thermal disorder of the samples that are at 500 °C during the measurements. Analogous observation can be made for the Ni K edge measurements since the Ni standard presents Debye-Waller factor of $0.57 \cdot 10^{-2}$ Å^2 for the Ni-Ni scattering at the coordination shell. For a given sample and at a given reaction condition, the Cu-M Debye-Waller factor is always bigger than the corresponding Ni-M Debye-Waller factor. It can be associated to the higher Cu concentration at the surface of the NPs (see Table 4.10), then increasing the structural disorder for the Cu-M scattering. Finally, all the Cu-M and Ni-M parameters are in accordance to typical values found for Cu/CeO_2 and Ni/CeO_2 NPs in the literature [60].

The coordination numbers associated to the Cu-O and Ni-O scatterings are in the limit of the detection and in the same order of the uncertainty associated to the fitting procedure. In spite of this, the exclusion of these contributions to the FT fit decreases significantly the quality of the fit performed. The Cu-O and Ni-O coordination numbers are consistent with the small Cu-O and Ni-O fractions observed in the NAP-XPS measurements.

4.4 The empirical-based design of a viable RWGS catalyst

According to the characterization procedures performed, the samples response to atmospheric stimuli is related to their atomic structure. It was observed that for supported NPs, a bimetallic composition promotes an synergistic effect enhancing the NPs reactivity [146, 147, 148, 149] towards the reverse water-gas shift reaction. Particularly, the Cu fraction on the NPs surface is the main factor related to their interaction with the support, during the activation process in H_2, and the ability to dissociate the CO_2 molecule.

The NPs synthesis can be related to the SMSI effect, since high Cu fractions used in the synthesis and, consequently, at the surface of the NPs ($Cu_{0.60}Ni_{0.40}/CeO_2$ and Cu/CeO_2 NPs) induced a interaction with the oxide support during the H_2 treatment, strong enough to present a capping layer surrounding the NPs and evidenced by the NAP-XPS measurements at $h\nu$=1250 eV and $h\nu$=2000 eV. This SMSI involves O donations from the NPs to the capping layer, indicated by the Cu oxidation states during H_2 reduction treatment observed by *in situ* time-resolved XANES measurements (Figure 4.3.9), and corroborated by the *in situ* time-resolved XANES measurements at the Ce L_3 edge (Figure 4.3.11). At the same time, a Cu (Ni) migration to the outer (inner) region of the NPs was observed. Later on, the exposure to carbon dioxide in the reaction $H_2+CO_2 \rightarrow H_2O+CO$ induced a Cu (Ni) migration to the NPs inner (outer) region, removing the CeO_2 capping layer around Cu/CeO_2 and $Cu_{0.60}Ni_{0.40}/CeO_2$ NPs.

The behavior established by the supported samples towards the RWGS reaction is diagrammatically explored at Figure 4.4.1. The graphic relates schematically the features induced by the H_2 treatment at NPs to the total reactivity of the sample during RWGS reaction. In the diagram is also presented the indicative of SMSI effect on each case at the beginning of the RWGS reaction (end of the reduction treatment).

In Figure 4.4.1 is possible to notice that the Ni migration to the surface of $Cu_{0.60}Ni_{0.40}/CeO_2$ NPs during RWGS reaction, associated to the CeO_x capping layer, reduces the NPs reactivity by the low fraction of $H_2+CO_2 \rightarrow H_2O+CO$ conversion. The reactivity worsening promoted by the cerium oxide capping layer effect is even more evidenced if comparing to the representation of $Cu_{0.25}Ni_{0.75}/CeO_2$ NPs and Cu/CeO_2 NPs. These both samples begins the reaction presenting high Cu concentrations at the surface, though the capped NPs are able to dissociate a small fraction of CO_2 while the uncapped NPs present high reactivity.

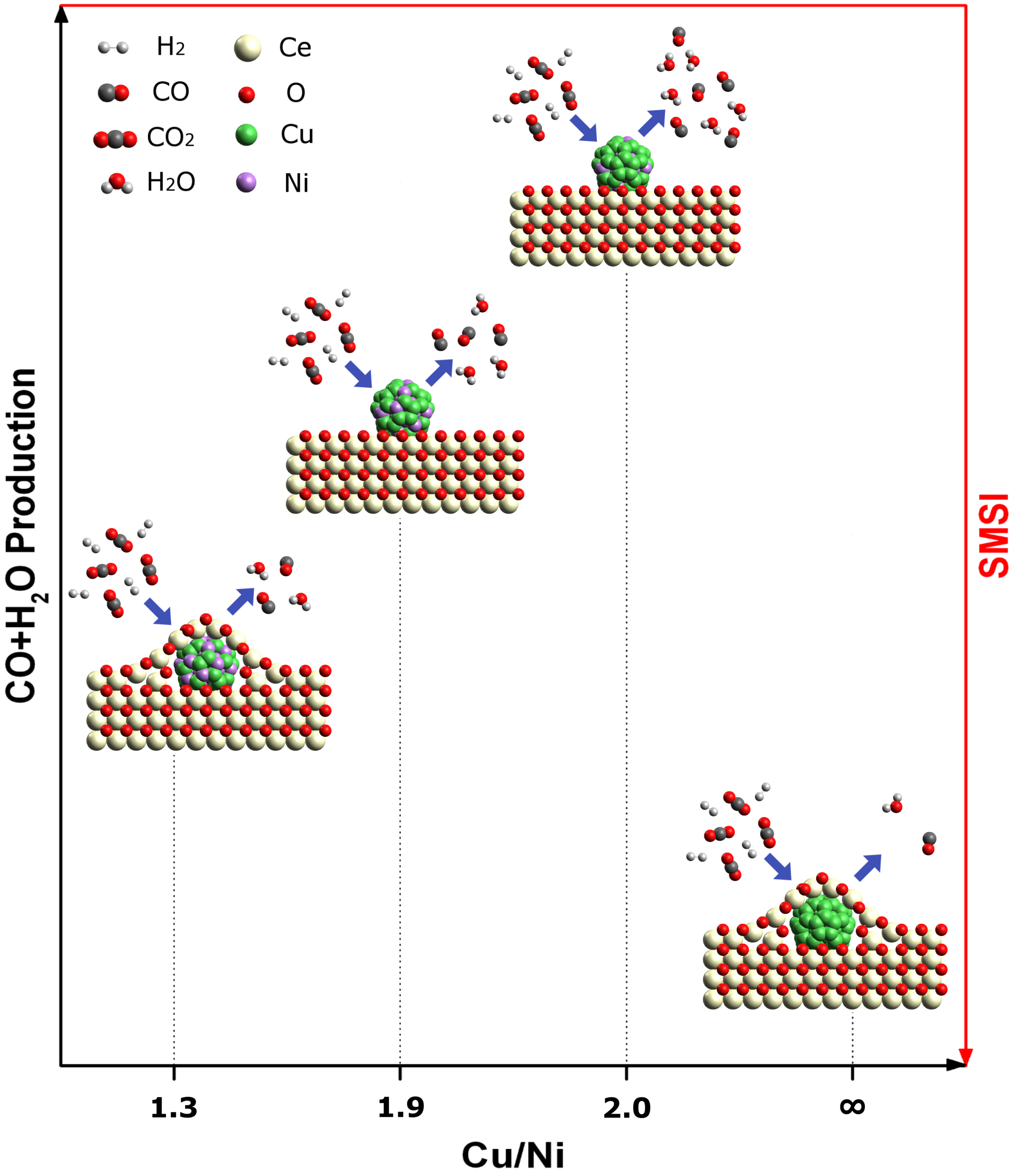

Figure 4.4.1 – Diagrammatic representation of the $Cu_{0.60}Ni_{0.40}/CeO_2$ NPs, $Cu_{0.35}Ni_{0.65}/CeO_2$ NPs, $Cu_{0.25}Ni_{0.75}/CeO_2$ NPs and Cu/CeO_2 NPs reactivity on the H_2+CO_2 atmosphere, evidencing the respective 1.3, 1.9, 2.0 and ∞ Cu/Ni fractions induced by the H_2 treatment, including the SMSI effect observed on the $Cu_{0.60}Ni_{0.40}/CeO_2$ NPs and Cu/CeO_2 NPs. The carbon dioxide dissociation reaction steps are represented by the blue arrows, indicating H_2 and CO_2 molecules flow inwards the NPs followed by outwards flow of CO and H_2O molecules.

Considering all these phenomena observed, a design of NPs synthesized with a high Ni concentration, mainly at the NPs surface, is encouraged in order to prevent interactions with the support (SMSI effect) and to enhances the reactivity/stability towards the RWGS reaction. This higher reactivity, in fact, occurs due to a Cu richer surface in NPs with smaller Cu concentrations during the RWGS reaction. Furthermore, due to the synergistic effect between Cu and Ni into the CO_2 dissociation reaction, a small Cu fraction is needed into the NPs in order to promote the RWGS with high reactivity. Further measurements of the catalytic activity and stability of the NPS are desired to improve this initial design.

5 CONCLUSIONS AND PERSPECTIVES

The present work was dedicated to shedding light on the elucidation of catalytic events at the atomic level in Cu_xNi_{1-x}/CeO_2 (x = 0.25, 0.35, 0.60, 1.00) NPs that have influence on the reactivity towards the CO_2 dissociation *via* reverse water-gas shift reaction at 500 °C. *In situ* measurements using synchrotron radiation techniques (NAP-XPS, time-resolved XANES, and EXAFS) were performed to characterize the catalysts surface and bulk structural and electronic properties during the activation of the catalyst (namely the H_2 reduction treatment) and the RWGS reaction, both at 500 °C.

NAP-XPS measurements showed that the Cu/Ni atomic concentration at the surface of the NPs is very dependent on the redox properties of the gaseous environment, in which the H_2 reducing atmosphere induced the migration of copper atoms to the surface region of the NPs, while the CO_2 oxidizing atmosphere promoted a nickel enrichment of the NPs surface. In this way, the surface atomic population was monitored by means of synthesis and atmospheric treatment.

The *in situ* time-resolved XANES measurements at the Cu K edge for the H_2 reduction treatment during heating from RT to 500 °C showed that the copper reduction follows a two-step process, initiated with a $2CuO \rightarrow Cu_2O+O$ dissociation and followed by the $Cu_2O \rightarrow 2Cu+O$ reduction. As the first step of the reduction process in copper begins, at ≈ 150 °C, a simultaneous oxidation process at the cerium oxide support can be observed for the copper-richer NPs (x = 1 and 0.60) by *in situ* time-resolved XANES measurements at the Ce L_3 edge. These associated processes characterize oxygen atoms donations, from the NPs to the support, indicating the existence of the geometrical factor of the SMSI effect (cerium oxide capping layer surrounding the NPs) in these Cu-rich NPs. The SMSI effect occurrence was confirmed by *in situ* NAP-XPS measurements, that showed also the surface recovery to the initial state after insertion of the CO_2 atmosphere. As a consequence of the SMSI effect, Cu atoms reduce earlier (lower temperatures) if compared to similar cases without the occurrence of the SMSI effect. Moreover, by means of NAP-XPS measurements at the Ce 3d region, it is demonstrated the nature of the SMSI effect that occurs trough interaction of the $Ce3d^{10}O2p^6Ce4f^1$ (Cu/CeO_2 NPs) and $Ce3d^{10}O2p^6Ce4f^0$ ($Cu_{0.60}Ni_{0.40}/CeO_2$ NPs) initial states with the neighborhood composed by Cu and Ni atoms at the surface of the NPs. It is the first time that such a detailed description of the nature of the SMSI effect is elucidated.

The CO_2 dissociation *via* RWGS reaction was explored. Among the supported systems, a synergistic effect improved the catalytic activity of bimetallic NPs, if compared to the copper monometallic case. A CO_2-induced nickel migration to NPs surface was observed, worsing the NPs reactivity towards carbon monoxide and water formation. Higher copper concentrations at NPs surface showed higher reactivity and longer copper-water interactions at the reaction's begin, however, the copper-richer systems at this stage presented the SMSI effect. The cerium oxide capping layer surrounding the NPs, characteristic of the SMSI effect, hinded the metallic catalysts from the H_2 and CO_2 molecules, reducing the amount of active sites available for the reaction. Associated to this phenomenon, it is observed that the SMSI effect influences negatively the reactivity of the NPs towards CO_2 dissociation via RWGS reaction.

The analysis of the systems led to the design of an optimized catalyst, thought as a Cu-Ni bimetallic NPs containing high amounts of Ni atoms in order to (i) avoid the geometrical factor of the SMSI effect, (ii) to give a Cu richer surface and, consequently, a higher reactivity towards CO_2 dissociation via RWGS reaction.

Future perspectives include the synthesis of the designed catalyst, and measurements of catalytic properties such as activity and selectivity. Further, we intend to investigate the influence of ceria properties such as pore density, surface area, grain size and Ce(III) fraction, when associated to the synthesized system towards the RWGS reaction.

BIBLIOGRAPHY

[1] Kazumasa Oshima, Tatsuya Shinagawa, Yukako Nogami, Ryo Manabe, Shuhei Ogo, and Yasushi Sekine. Low temperature catalytic reverse water-gas shift reaction assisted by an electric field. *Catalysis Today*, 232:27–32, 2014.

[2] D. Qin G.-K. Plattner M. Tignor S.K. Allen J. Boschung A. Nauels Y. Xia V. Bex Stocker, T.F. and P.M. Midgley (eds.). Cubasch, u., d. wuebbles, d. chen, m.c. facchini, d. frame, n. mahowald, and j.-g. winther, 2013: Introduction. in: Climate change 2013: The physical science basis. contribution of working group i to the fifth assessment report of the intergovernmental panel on climate change. Technical report, Cambridge University Press, Cambridge, United Kingdom and New York, NY, USA, 2013.

[3] D. Qin G.-K. Plattner M. Tignor S.K. Allen J. Boschung A. Nauels Y. Xia V. Bex Stocker, T.F. and P.M. Midgley (eds.). Hartmann, d.l., a.m.g. klein tank, m. rusticucci, l.v. alexander, s. brönnimann, y. charabi, f.j. dentener, e.j. dlugokencky, d.r. easterling, a. kaplan, b.j. soden, p.w. thorne, m. wild and p.m. zhai, 2013: Observations: Atmosphere and surface. in: Climate change 2013: The physical science basis. contribution of working group i to the fifth assessment report of the intergovernmental panel on climate change. Technical report, Cambridge University Press, Cambridge, United Kingdom and New York, NY, USA, 2013.

[4] D. Qin G.-K. Plattner M. Tignor S.K. Allen J. Boschung A. Nauels Y. Xia V. Bex Stocker, T.F. and P.M. Midgley (eds.). Rhein, M., S.R. Rintoul, S. Aoki, E. Campos, D. Chambers, R.A. Feely, S. Gulev, G.C. Johnson, S.A. Josey, A. Kostianoy, C. Mauritzen, D. Roemmich, L.D. Talley and F. Wang, 2013: Observations: Ocean. In: Climate Change 2013: The Physical Science Basis. Contribution of Working Group I to the Fifth Assessment Report of the Intergovernmental Panel on Climate Change. Technical report, Cambridge University Press, Cambridge, United Kingdom and New York, NY, USA, 2013.

[5] R.K. Pachauri Core Writing Team and L.A. Meyer (eds.). Ipcc, 2014: Climate change 2014: Synthesis report. contribution of working groups i, ii and iii to the fifth assessment report of the intergovernmental panel on climate change. Technical report, IPCC, Geneva, Switzerland, 2014.

[6] Alex Scott. Learning to love CO_2. *Chemical and Engineering News*, 93(45):10–16, 2015.

[7] J Skrzypek, M Lachowska, and D Serafin. Methanol synthesis from CO_2 and H_2: dependence of equilibrium conversions and exit equilibrium concentrations of components on the main process variables. *Chemical engineering science*, 45(1):89–96, 1990.

[8] Nada H Elsayed, Nathan RM Roberts, Babu Joseph, and John N Kuhn. Low temperature dry reforming of methane over Pt-Ni-Mg/ceria-zirconia catalysts. *Applied Catalysis B: Environmental*, 179:213–219, 2015.

[9] Dharik S Mallapragada, Navneet R Singh, Vlad Curteanu, and Rakesh Agrawal. Sun-to-fuel assessment of routes for fixing CO_2 as liquid fuel. *Industrial & Engineering Chemistry Research*, 52(14):5136–5144, 2013.

[10] Carl Bosch and Wilhelm Wild. Producing hydrogen., 1914. US Patent 1,115,776.

[11] Gabriele Centi and Siglinda Perathoner. Opportunities and prospects in the chemical recycling of carbon dioxide to fuels. *Catalysis Today*, 148(3):191–205, 2009.

[12] Cong Liu, Thomas R Cundari, and Angela K Wilson. CO_2 reduction on transition metal (Fe, Co, Ni, and Cu) surfaces: In comparison with homogeneous catalysis. *The Journal of Physical Chemistry C*, 116(9):5681–5688, 2012.

[13] Ching S Chen, Jia H Wu, and Tzu W Lai. Carbon dioxide hydrogenation on Cu nanoparticles. *The Journal of Physical Chemistry C*, 114(35):15021–15028, 2010.

[14] Ching-Shiun Chen, Wu-Hsun Cheng, and Shou-Shiun Lin. Mechanism of CO formation in reverse water-gas shift reaction over Cu/Al_2O_3 catalyst. *Catalysis letters*, 68(1):45–48, 2000.

[15] Ching-Shiun Chen, Wu-Hsun Cheng, and Shou-Shiun Lin. Study of reverse water-gas shift reaction by TPD, TPR and CO_2 hydrogenation over potassium-promoted Cu/SiO_2 catalyst. *Applied Catalysis A: General*, 238(1):55–67, 2003.

[16] Elise B Fox, Adam F Lee, Karen Wilson, and Chunshan Song. In-situ xps study on the reducibility of pd-promoted Cu/CeO_2 catalysts for the oxygen-assisted water-gas shift reaction. *Topics in Catalysis*, 49(1-2):89–96, 2008.

[17] WANG Luhui, Shaoxing ZHANG, and LIU Yuan. Reverse water-gas shift reaction over Co-precipitated Ni-CeO_2 catalysts. *journal of rare earths*, 26(1):66–70, 2008.

[18] Laura Barrio, Ania Kubacka, Gong Zhou, Michael Estrella, Arturo Martinez-Arias, Jonathan C Hanson, Marcos Fernandez-Garcia, and Jose A Rodriguez. Unusual physical and chemical properties of Ni in $Ce_{1\text{-}x}Ni_xO_{2\text{-}y}$ oxides: Structural

characterization and catalytic activity for the water-gas shift reaction. *The Journal of Physical Chemistry C*, 114(29):12689–12697, 2010.

[19] Yan Liu and Dazhuang Liu. Study of bimetallic Cu-Ni/γ-Al_2O_3 catalysts for carbon dioxide hydrogenation. *International Journal of Hydrogen Energy*, 24(4):351–354, 1999.

[20] Pedro A Derosa, Jorge M Seminario, and Perla B Balbuena. Properties of small bimetallic Ni-Cu clusters. *The Journal of Physical Chemistry A*, 105(33):7917–7925, 2001.

[21] Sung Su Kim, Hyun Hee Lee, and Sung Chang Hong. A study on the effect of support's reducibility on the reverse water-gas shift reaction over Pt catalysts. *Applied Catalysis A: General*, 423:100–107, 2012.

[22] DJ Pettigrew, DL Trimm, and NW Cant. The effects of rare earth oxides on the reverse water-gas shift reaction on palladium/alumina. *Catalysis letters*, 28(2-4):313–319, 1994.

[23] Jun Yoshihara and Charles T Campbell. Methanol synthesis and reverse water-gas shift kinetics over Cu (110) model catalysts: Structural sensitivity. *Journal of Catalysis*, 161(2):776–782, 1996.

[24] Shin-Ichiro Fujita, Masahito Usui, and Nobutsune Takezawa. Mechanism of the reverse water-gas shift reaction over Cu/ZnO catalyst. *Journal of Catalysis*, 134(1):220–225, 1992.

[25] Yolanda A Daza and John N Kuhn. CO_2 conversion by reverse water-gas shift catalysis: comparison of catalysts, mechanisms and their consequences for CO_2 conversion to liquid fuels. *RSC Advances*, 6(55):49675–49691, 2016.

[26] Wei Wang, Shengping Wang, Xinbin Ma, and Jinlong Gong. Recent advances in catalytic hydrogenation of carbon dioxide. *Chemical Society Reviews*, 40(7):3703–3727, 2011.

[27] G Ranga Rao, Sumanta Kumar Meher, Braja G Mishra, and P Hari K Charan. Nature and catalytic activity of bimetallic CuNi particles on CeO_2 support. *Catalysis today*, 198(1):140–147, 2012.

[28] Yue Li, Qi Fu, and Maria Flytzani-Stephanopoulos. Low-temperature water-gas shift reaction over Cu- and Ni- loaded cerium oxide catalysts. *Applied Catalysis B: Environmental*, 27(3):179–191, 2000.

[29] Jean-François Le Page. *Applied heterogeneous catalysis: design, manufacture, use of solid catalysts*. Editions Technip, 1987.

[30] Wolfgang Ruettinger, Xinsheng Liu, and Robert Farrauto. Enhanced stability water-gas shift reaction catalysts, November 9 2001. US Patent App. 10/039,447.

[31] Yang-guang Chen and Jie Ren. Conversion of methane and carbon dioxide into synthesis gas over alumina-supported nickel catalysts. Effect of Ni-Al_2O_3 interactions. *Catalysis Letters*, 29(1):39–48, 1994.

[32] A Goguet, R Burch, Y Chen, C Hardacre, P Hu, RW Joyner, FC Meunier, BS Mun, D Thompsett, and D Tibiletti. Deactivation mechanism of a Au/$CeZrO_4$ catalyst during a low-temperature water-gas shift reaction. *The Journal of Physical Chemistry C*, 111(45):16927–16933, 2007.

[33] Weiling Deng and Maria Flytzani-Stephanopoulos. On the issue of the deactivation of Au-ceria and Pt-ceria water-gas shift catalysts in practical fuel-cell applications. *Angewandte Chemie*, 118(14):2343–2347, 2006.

[34] Alexandre Goguet, Frederic C Meunier, Daniele Tibiletti, John P Breen, and Robbie Burch. Spectrokinetic investigation of reverse water-gas shift reaction intermediates over a Pt/CeO_2 catalyst. *The Journal of Physical Chemistry B*, 108(52):20240–20246, 2004.

[35] Frederick John Humphreys and Max Hatherly. *Recrystallization and related annealing phenomena*. Elsevier, 2012.

[36] Casey N Brodsky, Allison P Young, Ka Chon Ng, Chun-Hong Kuo, and Chia-Kuang Tsung. Electrochemically induced surface metal migration in well-defined core-shell nanoparticles and its general influence on electrocatalytic reactions. *ACS nano*, 8(9):9368–9378, 2014.

[37] Ebbe Christoffersen, Per Stoltze, and Jens Kehlet Nørskov. Monte carlo simulations of adsorption-induced segregation. *Surface science*, 505:200–214, 2002.

[38] Riccardo Ferrando, Julius Jellinek, and Roy L Johnston. Nanoalloys: from theory to applications of alloy clusters and nanoparticles. *Chemical reviews*, 108(3):845–910, 2008.

[39] Hanbin Liao, Adrian Fisher, and Zhichuan J Xu. Surface segregation in bimetallic nanoparticles: a critical issue in electrocatalyst engineering. *Small*, 11(27):3221–3246, 2015.

[40] Bing-Joe Hwang, Loka Subramanyam Sarma, Jiun-Ming Chen, Ching-Hsiang Chen, Shou-Chu Shih, Guo-Rung Wang, Din-Goa Liu, Jyh-Fu Lee, and Mau-Tsu Tang. Structural models and atomic distribution of bimetallic nanoparticles as investigated by X-ray absorption spectroscopy. *Journal of the American Chemical Society*, 127(31):11140–11145, 2005.

[41] Fabiano Bernardi, Gerhard H Fecher, Maria CM Alves, and Jonder Morais. Unraveling the formation of core-shell structures in nanoparticles by S-XPS. *The Journal of Physical Chemistry Letters*, 1(6):912–917, 2010.

[42] Fabiano Bernardi, Michael E Grass, Young P Hong, Rui Chang, Naila Jabeen, Chunjuan Zhang, Bryan W Eichhorn, Bora Seo, Selim Alayoglu, Zahid Hussain, et al. Control of the surface atomic population of $Rh_{0.5}Pd_{0.5}$ bimetallic nanoparticles supported on CeO_2. *Catalysis Today*, 260:95–99, 2016.

[43] Fabiano Bernardi, Maria CM Alves, Agnes Traverse, Dagoberto O Silva, Carla W Scheeren, Jairton Dupont, and Jonder Morais. Monitoring atomic rearrangement in Pt_xPd_{1-x} (x= 1, 0.7, or 0.5) nanoparticles driven by reduction and sulfidation processes. *The Journal of Physical Chemistry C*, 113(10):3909–3916, 2009.

[44] Andreas Weilhard, Gabriel Abarca, Janine Viscardi, Martin HG Prechtl, Jackson D Scholten, Fabiano Bernardi, Daniel L Baptista, and Jairton Dupont. Challenging thermodynamics: Hydrogenation of benzene to 1, 3-cyclohexadiene by Ru@Pt nanoparticles. *ChemCatChem*, 9(1):204–211, 2017.

[45] Dagoberto O Silva, Leandro Luza, Aitor Gual, Daniel L Baptista, Fabiano Bernardi, Maximiliano JM Zapata, Jonder Morais, and Jairton Dupont. Straightforward synthesis of bimetallic Co/Pt nanoparticles in ionic liquid: atomic rearrangement driven by reduction-sulfidation processes and Fischer-Tropsch catalysis. *Nanoscale*, 6(15):9085–9092, 2014.

[46] Núria J Divins, Inma Angurell, Carlos Escudero, Virginia Pérez-Dieste, and Jordi Llorca. Influence of the support on surface rearrangements of bimetallic nanoparticles in real catalysts. *Science*, 346(6209):620–623, 2014.

[47] Feng Tao, Michael E Grass, Yawen Zhang, Derek R Butcher, James R Renzas, Zhi Liu, Jen Y Chung, Bongjin S Mun, Miquel Salmeron, and Gabor A Somorjai. Reaction-driven restructuring of Rh-Pd and Pt-Pd core-shell nanoparticles. *Science*, 322(5903):932–934, 2008.

[48] Bing-Joe Hwang, Loka Subramanyam Sarma, Guo-Rung Wang, Ching-Hsiang Chen, Din-Goa Liu, Hwo-Shuenn Sheu, and Jyh-Fu Lee. Heat-induced alterations in the surface population of metal sites in bimetallic nanoparticles. *Chemistry-A European Journal*, 13(21):6255–6264, 2007.

[49] Zhufang Liu, Gregory S Jackson, and Bryan W Eichhorn. Tuning the CO-tolerance of Pt-Fe bimetallic nanoparticle electrocatalysts through architectural control. *Energy & Environmental Science*, 4(5):1900–1903, 2011.

[50] Norberto Chiodini, Franco Meinardi, Franca Morazzoni, Jin Padovani, Alberto Paleari, Roberto Scotti, and Giorgio Spinolo. Thermally induced segregation of SnO_2 nanoclusters in Sn-doped silica glasses from oversaturated Sn-doped silica xerogels. *Journal of Materials Chemistry*, 11(3):926–929, 2001.

[51] Mahdi Ahmadi, Farzad Behafarid, Chunhua Cui, Peter Strasser, and Beatriz Roldan Cuenya. Long-range segregation phenomena in shape-selected bimetallic nanoparticles: chemical state effects. *Acs Nano*, 7(10):9195–9204, 2013.

[52] R Pérez-Hernández, G Mondragón Galicia, D Mendoza Anaya, J Palacios, C Angeles-Chavez, and J Arenas-Alatorre. Synthesis and characterization of bimetallic Cu-Ni/ZrO_2 nanocatalysts: H_2 production by oxidative steam reforming of methanol. *International Journal of Hydrogen Energy*, 33(17):4569–4576, 2008.

[53] Jian Feng and Chao-Ping Zhang. Preparation of Cu-Ni alloy nanocrystallites in water-in-oil microemulsions. *Journal of colloid and interface science*, 293(2):414–420, 2006.

[54] P Li, Jingyue Liu, N Nag, and PA Crozier. In situ preparation of Ni-Cu/TiO_2 bimetallic catalysts. *Journal of Catalysis*, 262(1):73–82, 2009.

[55] Jahangeer Ahmed, Kandalam V Ramanujachary, Samuel E Lofland, Anthony Furiato, Govind Gupta, SM Shivaprasad, and Ashok K Ganguli. Bimetallic Cu-Ni nanoparticles of varying composition ($CuNi_3$, CuNi, Cu_3Ni). *Colloids and Surfaces A: Physicochemical and Engineering Aspects*, 331(3):206–212, 2008.

[56] John H Sinfelt. Catalysis by alloys and bimetallic clusters. *Accounts of Chemical Research*, 10(1):15–20, 1977.

[57] Shihua Wu, Changying Zhu, and Wenqiang Huang. Properties of polymer supported Ni-Cu bimetallic catalysts prepared by solvated metal atom impregnation. *Chinese Journal of Polymer Science*, 14(3):217–224, 1996.

[58] S Bernal, JJ Calvino, MA Cauqui, JM Gatica, C Larese, JA Pérez Omil, and JM Pintado. Some recent results on metal/support interaction effects in NM/CeO_2 (NM: noble metal) catalysts. *Catalysis Today*, 50(2):175–206, 1999.

[59] SJ Tauster, SC Fung, and Rl L Garten. Strong metal-support interactions. Group 8 noble metals supported on titanium dioxide. *Journal of the American Chemical Society*, 100(1):170–175, 1978.

[60] Lívia P Matte, Alex S Kilian, Leandro Luza, Maria CM Alves, Jonder Morais, Daniel L Baptista, Jairton Dupont, and Fabiano Bernardi. Influence of the CeO_2 support on the reduction properties of Cu/CeO_2 and Ni/CeO_2 nanoparticles. *The Journal of Physical Chemistry C*, 119(47):26459–26470, 2015.

[61] Selim Alayoglu, Kwangjin An, Gerome Melaet, Shiyou Chen, Fabiano Bernardi, Lin Wang Wang, Avery E Lindeman, Nathan Musselwhite, Jinghua Guo, Zhi Liu, et al. Pt-mediated reversible reduction and expansion of CeO_2 in Pt nanoparticle/mesoporous CeO_2 catalyst: In situ X-ray spectroscopy and diffraction studies under redox (H_2 and O_2) atmospheres. *The Journal of Physical Chemistry C*, 117(50):26608–26616, 2013.

[62] John C Matsubu, Shuyi Zhang, Leo DeRita, Nebojsa S Marinkovic, Jingguang G Chen, George W Graham, Xiaoqing Pan, and Phillip Christopher. Adsorbate-mediated strong metal-support interactions in oxide-supported Rh catalysts. *Nature Chemistry*, 9(2):120–127, 2017.

[63] Qiang Fu, Thomas Wagner, Sven Olliges, and Heinz-Dieter Carstanjen. Metal-oxide interfacial reactions: Encapsulation of Pd on TiO_2 (110). *The Journal of Physical Chemistry B*, 109(2):944–951, 2005.

[64] Stefan Labich, Edmund Taglauer, and Helmut Knözinger. Metal-support interactions on rhodium model catalysts. *Topics in Catalysis*, 14(1):153–161, 2000.

[65] Lee Eng Oi, Min-Yee Choo, Hwei Voon Lee, Hwai Chyuan Ong, Sharifah Bee Abd Hamid, and Joon Ching Juan. Recent advances of titanium dioxide (TiO_2) for green organic synthesis. *RSC Advances*, 6(110):108741–108754, 2016.

[66] Quan Zhuang, Yongning Qin, and Liu Chang. Promoting effect of cerium oxide in supported nickel catalyst for hydrocarbon steam-reforming. *Applied catalysis*, 70(1):1–8, 1991.

[67] A Maubert, GA Martin, H Praliaud, and P Turlier. CeO_2-supported nickel catalysts. Evidence of a strong metal-support ineraction. *Reaction Kinetics and Catalysis Letters*, 24(1-2):183–186, 1984.

[68] Wei Liu and Maria Flytzani-Stephanopoulos. Transition metal-promoted oxidation catalysis by fluorite oxides: A study of CO oxidation over Cu/CeO_2. *The Chemical Engineering Journal and the Biochemical Engineering Journal*, 64(2):283–294, 1996.

[69] Wei-Ping Dow, Yu-Piao Wang, and Ta-Jen Huang. TPR and XRD studies of yttria-doped ceria/γ-alumina-supported copper oxide catalyst. *Applied Catalysis A: General*, 190(1):25–34, 2000.

[70] Chen-Wei Liu, Yu-Chen Wei, and Kuan-Wen Wang. Surface condition manipulation and oxygen reduction enhancement of PtAu/C catalysts synergistically modified by CeO_2 addition and N_2 treatment. *The Journal of Physical Chemistry C*, 115(17):8702–8708, 2011.

[71] Song Qin, Changwei Hu, Huaqing Yang, and Zhishan Su. Theoretical study on the reaction mechanism of the gas-phase $H_2/CO_2/Ni$ (3d) system. *The Journal of Physical Chemistry A*, 109(29):6498–6502, 2005.

[72] MJL Ginés, AJ Marchi, and CR Apesteguia. Kinetic study of the reverse water-gas shift reaction over $CuO/ZnO/Al_2O_3$ catalysts. *Applied Catalysis A: General*, 154(1-2):155–171, 1997.

[73] Feng Tao, Michael E Grass, Yawen Zhang, Derek R Butcher, Funda Aksoy, Shaul Aloni, Virginia Altoe, Selim Alayoglu, James R Renzas, Chia-Kuang Tsung, et al. Evolution of structure and chemistry of bimetallic nanoparticle catalysts under reaction conditions. *Journal of the American Chemical Society*, 132(25):8697–8703, 2010.

[74] D Frank Ogletree, Hendrik Bluhm, Gennadi Lebedev, Charles S Fadley, Zahid Hussain, and Miquel Salmeron. A differentially pumped electrostatic lens system for photoemission studies in the millibar range. *Review of Scientific Instruments*, 73(11):3872–3877, 2002.

[75] Alexander Yu Klyushin, Tulio CR Rocha, Michael Hävecker, Axel Knop-Gericke, and Robert Schlögl. A near ambient pressure XPS study of Au oxidation. *Physical Chemistry Chemical Physics*, 16(17):7881–7886, 2014.

[76] Fabiano Bernardi, Maria CM Alves, and Jonder Morais. Monitoring of Pt nanoparticle formation by H_2 reduction of PtO_2: An in situ dispersive X-ray absorption spectroscopy study. *The Journal of Physical Chemistry C*, 114(49):21434–21438, 2010.

[77] D.B. Williams and C.B. Carter. *Transmission Electron Microscopy: A Textbook for Materials Science.* Number v. 2 in Cambridge library collection. Springer, 2009.

[78] B. Fultz and J.M. Howe. *Transmission Electron Microscopy and Diffractometry of Materials.* Graduate Texts in Physics. Springer Berlin Heidelberg, 2012.

[79] Poul L Hansen, Jakob B Wagner, Stig Helveg, Jens R Rostrup-Nielsen, Bjerne S Clausen, and Henrik Topsøe. Atom-resolved imaging of dynamic shape changes in supported copper nanocrystals. *Science*, 295(5562):2053–2055, 2002.

[80] H.E. Duckworth, R.C. Barber, and V.S. Venkatasubramanian. *Mass Spectroscopy.* Cambridge Monographs on Physics. Cambridge University Press, 1990.

[81] Website. http://www.chemguide.co.uk/analysis/masspec/howitworks.html, 2015.

[82] National Institute of Standards and Technology. *NIST Standard Reference Database 69, NIST Chemistry WebBook.* 2014.

[83] National Institute of Standards and Technology. *NIST Standard Reference Database 69, NIST Chemistry WebBook.* 2014.

[84] National Institute of Standards and Technology. *Atomic Weights and Isotopic Compositions, Version 4.1.* 2015.

[85] K. Codling, C. Kunz, W. Gudat, E.E. Koch, A. Kotani, D.W. Lynch, E.M. Rowe, B.F. Sonntag, and Y. Toyozawa. *Synchrotron Radiation: Techniques and Applications.* Topics in Current Physics. Springer Berlin Heidelberg, 2013.

[86] S. Mobilio, F. Boscherini, and C. Meneghini. *Synchrotron Radiation: Basics, Methods and Applications.* Springer Berlin Heidelberg, 2014.

[87] Julio C Cezar, Narcizo M Souza-Neto, Cinthia Piamonteze, Edilson Tamura, Flavio Garcia, Edson J Carvalho, Régis T Neueschwander, Aline Y Ramos, Helio CN Tolentino, Alberto Caneiro, et al. Energy-dispersive X-ray absorption spectroscopy at LNLS: investigation on strongly correlated metal oxides. *Journal of synchrotron radiation*, 17(1):93–102, 2010.

[88] C.R. Brundle and A.D. Baker. *Electron Spectroscopy: Theory, Techniques and Applications.* Number v. 2 in Electron Spectroscopy: Theory, Techniques and Applications. Academic Press, 1977.

[89] J.F. Watts and J. Wolstenholme. *An Introduction to Surface Analysis by XPS and AES.* Wiley, 2003.

[90] National Institute of Standards and Technology. *NIST X-ray Photoelectron Spectroscopy Database, Version 4.1.* 2012.

[91] C.D. Wagner and G.E. Muilenberg. *Handbook of X-ray photoelectron spectroscopy: a reference book of standard data for use in X-ray photoelectron spectroscopy.* Physical Electronics Division, Perkin-Elmer Corp., 1979.

[92] M Pl Seah and WA Dench. Quantitative electron spectroscopy of surfaces: a standard data base for electron inelastic mean free paths in solids. *Surface and interface analysis*, 1(1):2–11, 1979.

[93] David R Penn. Quantitative chemical analysis by ESCA. *Journal of Electron Spectroscopy and Related Phenomena*, 9(1):29–40, 1976.

[94] Website. http://www.globalsino.com/micro/TEM/images/TEM9923.gif.

[95] V Pérez-Dieste, L Aballe, S Ferrer, J Nicolàs, C Escudero, A Milán, and E Pellegrin. Near ambient pressure XPS at ALBA. 425(7):072023, 2013.

[96] D Frank Ogletree, Hendrik Bluhm, Eleonore D Hebenstreit, and Miquel Salmeron. Photoelectron spectroscopy under ambient pressure and temperature conditions. *Nuclear Instruments and Methods in Physics Research Section A: Accelerators, Spectrometers, Detectors and Associated Equipment*, 601(1):151–160, 2009.

[97] G. Bunker. *Introduction to XAFS: A Practical Guide to X-ray Absorption Fine Structure Spectroscopy.* Introduction to XAFS: A Practical Guide to X-ray Absorption Fine Structure Spectroscopy. Cambridge University Press, 2010.

[98] Dale E Sayers, Edward A Stern, and Farrel W Lytle. New technique for investigating noncrystalline structures: Fourier analysis of the extended X-ray absorption fine structure. *Physical Review Letters*, 27(18):1204, 1971.

[99] John J Rehr and Robert C Albers. Theoretical approaches to X-ray absorption fine structure. *Reviews of modern physics*, 72(3):621, 2000.

[100] Walter Kohn and Lu Jeu Sham. Self-consistent equations including exchange and correlation effects. *Physical review*, 140(4A):A1133, 1965.

[101] JJ Rehr, J Mustre de Leon, SI Zabinsky, and RC Albers. Theoretical X-ray absorption fine structure standards. *Journal of the American chemical society*, 113(14):5135–5140, 1991.

[102] Salil U Rege, Ralph T Yang, and Charles A Cain. Desorption by ultrasound: phenol on activated carbon and polymeric resin. *AIChE journal*, 44(7):1519–1528, 1998.

[103] Marc Breitbach, Dieter Bathen, and Henner Schmidt-Traub. Effect of ultrasound on adsorption and desorption processes. *Industrial & engineering chemistry research*, 42(22):5635–5646, 2003.

[104] Dave A Shirley. High-resolution X-ray photoemission spectrum of the valence bands of gold. *Physical Review B*, 5(12):4709, 1972.

[105] Dahlang Tahir, Nur Harmila Sari, et al. Stopping powers and inelastic mean free path of 200eV-50keV electrons in polymer PMMA, PE, and PVC. *Applied Radiation and Isotopes*, 95:59–62, 2015.

[106] James H Scofield. Theoretical photoionization cross sections from 1 to 1500 keV. Technical report, CALIFORNIA UNIV., LIVERMORE. LAWRENCE LIVERMORE LAB., 1973.

[107] Lellery Storm and Harvey I Israel. Photon cross sections from 1 keV to 100 MeV for elements z=1 to z=100. *Atomic Data and Nuclear Data Tables*, 7(6):565–681, 1970.

[108] AC Miller and GW Simmons. Copper by XPS. *Surface Science Spectra*, 2(1):55–60, 1993.

[109] Richard P Vasquez. $CuCl_2$ by XPS. *Surface Science Spectra*, 2(2):160–164, 1993.

[110] RP Vasquez. CuO by XPS. *Surface Science Spectra*, 5(4):262–266, 1998.

[111] G Mattogno, R Zanoni, D Giusto, G Russo, and L Sisti. XPS evidence for the formation of Ni(ii) complexes on treated activated carbon. *Inorganica chimica acta*, 104(1):9–13, 1985.

[112] AN Mansour and CA Melendres. Characterization of α-$Ni(OH)_2$ by XPS. *Surface Science Spectra*, 3(3):255–262, 1994.

[113] AN Mansour. Characterization of β-$Ni(OH)_2$ by XPS. *Surface Science Spectra*, 3(3):239–246, 1994.

[114] AV Ruban, Hans Lomholt Skriver, and Jens Kehlet Nørskov. Surface segregation energies in transition-metal alloys. *Physical Review B*, 59(24):15990, 1999.

[115] Junais Habeeb Mokkath and Udo Schwingenschlögl. Magnetic phase transition in $2NMNi_xCu_{1-x}$ ($0<x<1$) clusters. *The Journal of Physical Chemistry C*, 118(15):8169–8173, 2014.

[116] Leandro Luza, Camila P Rambor, Aitor Gual, Fabiano Bernardi, Josiel B Domingos, Thomas Grehl, Philipp Bruner, and Jairton Dupont. Catalytically active membranelike devices: Ionic liquid hybrid organosilicas decorated with palladium nanoparticles. *ACS Catalysis*, 6(10):6478–6486, 2016.

[117] Grégory Guisbiers, Subarna Khanal, Francisco Ruiz-Zepeda, Jorge Roque de la Puente, and Miguel José-Yacaman. Cu-Ni nano-alloy: mixed, core-shell or Janus nano-particle? *Nanoscale*, 6(24):14630–14635, 2014.

[118] Jiann-Horng Lin and Vadim V Guliants. Alumina-supported Cu@Ni and Ni@Cu core-shell nanoparticles: Synthesis, characterization, and catalytic activity in water-gas shift reaction. *Applied Catalysis A: General*, 445:187–194, 2012.

[119] Gabor A Somorjai and Yimin Li. *Introduction to surface chemistry and catalysis.* John Wiley & Sons, 2010.

[120] Marta Maria Natile, Alessandro Galenda, and Antonella Glisenti. CuO/CeO_2 nanocomposites: An XPS study. *Surface Science Spectra*, 16(1):13–26, 2009.

[121] AC Miller and GW Simmons. Nickel by XPS. *Surface Science Spectra*, 1(3):312–317, 1992.

[122] Simon K Beaumont, Selim Alayoglu, Vladimir V Pushkarev, Zhi Liu, Norbert Kruse, and Gabor A Somorjai. Exploring surface science and restructuring in reactive atmospheres of colloidally prepared bimetallic CuNi and CuCo nanoparticles on SiO_2 in situ using ambient pressure X-ray photoelectron spectroscopy. *Faraday discussions*, 162:31–44, 2013.

[123] Akio Kotani, T Jo, and JC Parlebas. Many-body effects in core-level spectroscopy of rare-earth compounds. *Advances in Physics*, 37(1):37–85, 1988.

[124] Klaus-Dieter Schierbaum. Ordered ultra-thin cerium oxide overlayers on Pt (111) single crystal surfaces studied by LEED and XPS. *Surface science*, 399(1):29–38, 1998.

[125] Peter Burroughs, Andrew Hamnett, Anthony F Orchard, and Geoffrey Thornton. Satellite structure in the X-ray photoelectron spectra of some binary and mixed oxides of lanthanum and cerium. *Journal of the Chemical Society, Dalton Transactions*, (17):1686–1698, 1976.

[126] Guilherme B Della Mea, Lívia P Matte, Alisson S Thill, Francielli O Lobato, Edilson V Benvenutti, Leliz T Arenas, Astrid Jürgensen, Roland Hergenröder, Fernanda S Poletto, and Fabiano Bernardi. Tuning the oxygen vacancy population of cerium oxide (CeO_{2-x}, $0<x<0.5$) nanoparticles. *Applied Surface Science*, 2017.

[127] A Pfau and KD Schierbaum. The electronic structure of stoichiometric and reduced CeO_2 surfaces: an XPS, UPS and HREELS study. *Surface Science*, 321(1-2):71–80, 1994.

[128] DR Mullins, SH Overbury, and DR Huntley. Electron spectroscopy of single crystal and polycrystalline cerium oxide surfaces. *Surface Science*, 409(2):307–319, 1998.

[129] Hideo Orita, Shuichi Naito, and Kenzi Tamaru. Nature of SMSI effect on carbon monoxide + molecular hydrogen reaction over supported rhodium catalysts. *The Journal of Physical Chemistry*, 89(14):3066–3069, 1985.

[130] M Guenin, PN Da Silva, and R Frety. Influence of chlorine towards metal-support and metal-sulphur support interactions. *Applied catalysis*, 27(2):313–323, 1986.

[131] Ambesh G Shastri, AK Datye, and Johannes Schwank. Influence of chlorine on the surface area and morphology of TiO_2. *Applied catalysis*, 14:119–131, 1985.

[132] M Abid and R Touroude. Pt/CeO_2 catalysts in selective hydrogenation of crotonaldehyde: high performance of chlorine-free catalysts. *Catalysis letters*, 69(3):139–144, 2000.

[133] SJ Tauster. Strong metal-support interactions. *Accounts of Chemical Research*, 20(11):389–394, 1987.

[134] Simon Bonanni, Kamel Aït-Mansour, Harald Brune, and Wolfgang Harbich. Overcoming the strong metal-support interaction state: CO oxidation on TiO_2 (110)-supported Pt nanoclusters. *Acs Catalysis*, 1(4):385–389, 2011.

[135] Marta Maria Natile and Antonella Glisenti. Nanostructured CeO_2 powders by XPS. *Surface Science Spectra*, 13(1):17–30, 2006.

[136] Davide Barreca, Giovanni A Battiston, Rosalba Gerbasi, and Eugenio Tondello. Study of cerium dioxide thin films by X-ray photoelectron spectroscopy. *Surface Science Spectra*, 7(4):297–302, 2000.

[137] FA Lima, ME Saleta, RJS Pagliuca, MA Eleotério, RD Reis, J Fonseca Júnior, B Meyer, EM Bittar, NM Souza-Neto, and E Granado. XDS: a flexible beamline for X-ray diffraction and spectroscopy at the brazilian synchrotron. *Journal of Synchrotron Radiation*, 23(6), 2016.

[138] Bruce Ravel and MATHENA Newville. Athena, Artemis, Hephaestus: data analysis for X-ray absorption spectroscopy using IFEFFIT. *Journal of synchrotron radiation*, 12(4):537–541, 2005.

[139] Website. http://bruceravel.github.io/demeter/dpg/mue/deglitch.html.

[140] R. Winefordner J. D. ed. D. C. Koningsberger, R. Prins. *X-ray absorption*, volume 92. New York: John Wiley and Sons, 1988.

[141] S Poulston, PM Parlett, P Stone, and M Bowker. Surface oxidation and reduction of CuO and Cu_2O studied using XPS and XAES. *Surface and Interface Analysis*, 24(12):811–820, 1996.

[142] Jae Y Kim, José A Rodriguez, Jonathan C Hanson, Anatoly I Frenkel, and Peter L Lee. Reduction of CuO and Cu_2O with H_2: H embedding and kinetic effects in the formation of suboxides. *Journal of the American Chemical Society*, 125(35):10684–10692, 2003.

[143] Yoshio Takahashi, Hiroshi Sakami, and Masaharu Nomura. Determination of the oxidation state of cerium in rocks by Ce L iii-edge X-ray absorption near-edge structure spectroscopy. *Analytica Chimica Acta*, 468(2):345–354, 2002.

[144] Website. http://monalisa.phys.washington.edu/feff/Docs/feff6/feff6.txt, 1993.

[145] Jason A Farmer and Charles T Campbell. Ceria maintains smaller metal catalyst particles by strong metal-support bonding. *Science*, 329(5994):933–936, 2010.

[146] Adrian Ungureanu, Brindusa Dragoi, Alexandru Chirieac, Carmen Ciotonea, Sebastien Royer, Daniel Duprez, Anne Sophie Mamede, and Emil Dumitriu. Composition-dependent morphostructural properties of Ni-Cu oxide nanoparticles confined within the channels of ordered mesoporous SBA-15 silica. *ACS applied materials & interfaces*, 5(8):3010–3025, 2013.

[147] Jiann-Horng Lin, Prakash Biswas, Vadim V Guliants, and Scott Misture. Hydrogen production by water-gas shift reaction over bimetallic Cu-Ni catalysts supported on La-doped mesoporous ceria. *Applied Catalysis A: General*, 387(1):87–94, 2010.

[148] Loredana De Rogatis, Tiziano Montini, Andrea Cognigni, Luca Olivi, and Paolo Fornasiero. Methane partial oxidation on NiCu-based catalysts. *Catalysis Today*, 145(1):176–185, 2009.

[149] JA Dalmon and GA Martin. Hydrogenolysis of C_2H_6, C_3H_8 and N-C_4H_{10} over silica-supported nickel-copper catalysts. *Journal of Catalysis*, 66(1):214–221, 1980.